Dissertation

submitted to the

Combined Faculties of the Natural Sciences and Mathematics

of the Ruperto-Carola-University of Heidelberg, Germany

for the degree of

Doctor of Natural Sciences

Put forward by

Dipl. Phys. Tobias Rentrop

born in: Weinheim, Germany

Oral examination: 29 June 2016

Observation of the Phononic Lamb Shift in a Synthetic Vacuum

Referees: Prof. Dr. Markus K. Oberthaler
Prof. Dr. Selim Jochim

Zusammenfassung

Diese Doktorarbeit beschreibt die experimentelle Umsetzung des Fröhlich-Hamiltonoperators in einer Mischung ultrakalter atomarer Gase. Dafür werden einzelne Atome in ein Bose-Einstein Kondensat (BEC) eingebracht, welche die Rolle von Verunreinigungen spielen. Diese Atome werden in einer Raumrichtung durch ein starkes, element-selektives optisches Potential gebunden. Dabei werden ihre externen Energieniveaus durch die Kopplung an die Anregungen (Phononen) des BECs verschoben. Dies entspricht den Lamb-Verschiebungen im Wasserstoffatom, welche durch Wechselwirkung mit dem Vakuum entstehen. In diesem Sinne kann das BEC als synthetisches Vakuum und die Energieänderung als phononisch-erzeugte Lamb-Verschiebung bezeichnet werden.
Durch kinetische Ramsey-Spektroskopie wird die Lücke zwischen den niedrigsten Fallen-Niveaus bestimmt. Zur Bestimmung der energetischen Veränderung durch die Wechselwirkung mit dem Hintergrund wird das Experiment mit und ohne BEC durchgeführt. Der Hintergrund beeinflusst die Energielücke durch zwei Mechanismen: zum einen wird das BEC durch das Fallenpotential für die Verunreinigungen ebenfalls leicht moduliert, zum anderen durch die Wechselwirkung über Phononen. Beide Effekte werden beobachtet und quantitativ beschrieben. Die Änderung des Abstands zwischen den Energieniveaus durch phononische Wechselwirkung wird für fermionische Verunreinigungen (^{6}Li) zu $(6 \pm 1) \cdot 10^{-4}$ bestimmt. Die Streuung von Phononen kann durch den Einsatz kondensierter bosonischer Verunreinigungen (^{7}Li) verstärkt werden, was zu einer gemessenen Änderung von $(4 \pm 0.1) \cdot 10^{-3}$ führt. Außerdem wird die Abhängigkeit der phononisch bewirkten Verschiebung von der Anzahl der ^{7}Li Atome und der relativen Besetzung der Energieniveaus dargestellt. Diese erste Beobachtung des Fröhlich-Hamiltonoperators in externen Freiheitsgraden in einer Mischung ultrakalter Gase erlaubt erstmals einen Zugang für zukünftige Tests von Theorien in einer hochgradig flexiblen Umgebung.

Abstract

This thesis reports on the implementation of the Fröhlich Hamiltonian in an ultracold atomic mixture. To this end, impurity atoms are immersed into a macroscopic Bose-Einstein condensate (BEC). The impurities are tightly trapped in one direction by a species-selective optical potential. In this scenario their coupling to the excitations (phonons) of the BEC causes energy shifts of their external states that are analogues to the electronic Lamb shift in the hydrogen atom, which originates from interaction with the vacuum. Therefore the BEC can be denoted *synthetic vacuum* and the energy shift termed *phonon-induced Lamb shift*. The energy gap between the lowest lying trap levels for the impurities is determined via motional Ramsey spectroscopy. For the detection of the energetic modifications due to interaction with the background, experiments are performed with and without BEC. The background modifies the gap by two mechanisms: the modulation of the BEC density by the optical trapping potential for the impurities, and the interaction with phonons. Both effects are observed and a quantitative description is derived. The relative change of the gap due to phononic interaction for fermionic ^{6}Li impurities is found to be $(6 \pm 1) \cdot 10^{-4}$. The phonon scattering can be enhanced by the use of a Bose-Einstein condensed impurity (^{7}Li), where we measured $(4 \pm 0.1) \cdot 10^{-3}$. Furthermore we present the dependence of the phonon induced shift on the absolute atom number and the relative population of states for ^{7}Li. This first observation of the Fröhlich Hamiltonian in motional degrees of freedom in an ultracold gas mixture paves the way to put theory to a test in a highly flexible environment.

Contents

1 Introduction

Although quantum mechanics makes predictions in terms of probabilities, an overwhelming number of them can safely be observed and confirmed in the form of expectation values. Among them are the precise measurements of the system's eigenenergies. If excited states are coupled to the environment, their population can decay. The rate of this change can be estimated by, for instance, Fermi's golden rule [1, 2]. It is this source of decoherence which is a bridge from quantum mechanics to classical mechanics for mesoscopic systems. In addition, the coupling to the environment manifests itself also in observable effects for the system under investigation, for example in shifts of energy levels.
The hydrogen atom can be solved quantum-mechanically [3]. Even taking relativistic effects and the spin degree of freedom of the electron into account, the calculation based on the Dirac equation [4] results in degeneracy of states with the same total angular momentum. Accordingly it was a big surprise when in 1947 Lamb and Retherford found the $2S_{1/2}$ and the $2P_{3/2}$ state of the hydrogen atom to be split by about 1 GHz [5]. A lot of experimental effort has been put into the investigation of this Lamb shift in hydrogen [6, 7].
The explanation of the Lamb shift by Bethe was the groundwork of quantum electrodynamics [8]. Conceptionally, vacuum fluctuations cause virtual absorption and emission processes of photons, changing the energy of the electronic states. In a quasiclassical picture the distance of the electron to the nucleus varies as it moves around the nucleus, hence the effect is strongest if the electron's probability of presence at the location of the proton is distinct from zero. Even the mass of the free electron is strongly affected by the vacuum fluctuations, a phenomenon known as Bethe electron mass renormalization [9]. Both effects are non-relativistic. In its further development, quantum electrodynamics proved to be a powerful concept, as demonstrated by the fact that the theoretically computed value for the electron's Landé factor coincides with measurements up to the 11^{th} decimal place [10].
This concept of an electron subject to fluctuations due to coupling to the electromagnetic vacuum is very powerful and can be generally applied to a wealth of similar scenarios, like a mobile electron in a semiconductor. In this case, non-relativistic electrons interact with the ionic lattice via the Coulomb force. Coupling to the collective lattice excitations (phonons) modifies the electron's dispersion relation. In an effective picture, this dressed electron can be described by a quasi-particle,

the polaron [11–14]. Due to phonon absorption and emission, its mass is effectively increased [15, 16]. The field-theoretical formulation of this problem goes back to Fröhlich and the corresponding Hamiltonian bears his name. Although it opens a straightforward access to the problem, it is not exactly solvable by analytic calculations. Therefore the amount of suitable applications is still open. Besides describing many important fundamental aspects of solid state materials [17, 18] it reaches to recent material research such as high temperature superconductors [19] and organic semiconductors [20, 21].
If the model is extended to an electron in a semiconductor bound to a defect, it is called a bound polaron. Due to the phononic coupling, its energy levels are shifted, which is the analogous mechanism as in the famous case of the electron in the hydrogen atom. By reason of this analogy, the effect is referred to as phonon-induced Lamb shift and was predicted already 50 years ago [22–24]. In the 1970s experiments on solid state systems were performed, without clear signal of the phononic Lamb shift [25, 26]. The main reason for this is that disorder leads to varying defect spectra over the sample and disguises the dressing effect.
While these effects are hard to resolve in solid state materials, fortunately the Fröhlich Hamiltonian can be realized with ultracold dilute gas mixtures of neutral atoms [27–30], where an impurity atom is immersed into a macroscopic Bose-Einstein-condensate (BEC). In this non-relativistic system, the low lying excitations of the BEC (phonons) play the role of the photons in the case of the hydrogen atom. For small momenta the phonons have a linear dispersion relation, analogous to the photons of the electromagnetic field. The general advantage of such a model system is the possibility to tune the coupling strength, the characteristic velocity of excitations in the medium (sound velocity) and the confining potentials [31–33]. The validity of the mapping onto the Fröhlich Hamiltonian relies on a finite impurity-BEC interaction strength [29].
Ultracold atom systems have been widely employed for the study of polaronic effects. Two different realizations are possible: in the context of an impurity in a Fermi sea the quasi-particle is termed Fermi polaron, in case of an atom immersed into a BEC it is named Bose polaron. Solely the Bose polaron is described by the Fröhlich Hamiltonian, whereas the Fermi polaron is closest to Pekar's primal concept. Here the impurity is dressed with the localized cloud of scattered fermions. Most experiments to date study the Fermi polaron, where e. g. the binding energy has been studied extensively by radiofrequency spectroscopy [34–37]. Decelerated oscillation speed in a shallow trap revealed its increased effective mass [38], see [39] for a review on Fermi polarons.
For impurities immersed in a one-dimensional BEC indications of polaronic effects have been observed [40, 41]. However, the Lamb shift and a unique signal of the Bose polaron have not been observed yet. Previous experiments with ultracold Bose-Fermi mixtures on interaction-induced energy shifts concentrated on BECs of a few atoms with completely frozen motional degrees of freedom [42–44]. In this

scenario the impurity distorts the whole bosonic wave function, relying on short wavelength phonons, which have a quadratic dispersion relation. This weakens the comparison to the electromagnetic field. Previous experiments on the Lamb shift with thermal atoms elevated its outcome by amplifying the electromagnetic field by cavities [45, 46]. Furthermore it has been studied in superconducting circuits [47]. In a quantum gas realization the BEC plays the role of the vacuum. As the BEC can be vastly controlled it is declared synthetic.
In this thesis the implementation of the Fröhlich Hamiltonian with tightly confined impurities is reported, in analogy to an electron bound to an ion in a semiconductor or an electron bound to a proton in the hydrogen atom. The impurities are strongly confined in one direction by an optical potential, whereas the phonon bath remains weakly trapped in all directions. Hence only a local change of the BEC wave function takes place and Lamb shifts due to potential shapes beyond the conventional Coulombic potential can be modeled.
We observe the phononic Lamb shift by spectroscopy of the gap between the two lowest energy levels of the bound impurity employing motional Ramsey spectroscopy [48, 49]. As we can remove the BEC from the system, we can directly compare the properties of the dressed and the bare impurity. This possibility does not exist in other systems, neither the vacuum nor the ionic lattice can be deactivated. It is essential for the validity of the Fröhlich Hamiltonian in the impurity-BEC scenario to remain in the weakly interacting regime. Accordingly the energy shifts are small for fermionic impurities. Our model system permits the use of the corresponding bosonic isotope as well. Thereby we can enhance the shifts by amplification due to macroscopic occupation of states, as high occupation numbers increase the probability of phonon interaction. The high signal values obtained enable us to perform a systematic study despite the weak coupling. The dependence of the shift on the populations of the investigated states is accessible as well.
Our results are compared with a perturbative Lamb shift calculation without free parameters. We find quantitative agreement of the measurements with the theoretical predictions based on the Fröhlich Hamiltonian.

This thesis is structured in the following way: In chapter 2, essential modifications of the experimental setup are detailed, which enabled the spectroscopy of the impurity energy levels with high precision. In chapter 3, atomic mixtures in traps and their density distributions are discussed. Further basic characteristics of a BEC, which are essential for understanding the impurity-BEC coupling, are highlighted. In chapter 4 the optical lattice is introduced and characterized, which is our tool to address and detect impurity properties. Chapter 5 discusses the theory of background induced shifts for impurities and the corresponding theoretical predictions for our experimental setup. Chapter 6 presents the experimental observation of the phononic Lamb shift. Concluding remarks and an outlook are given in chapter 7.

2 Experimental Setup

The first chapter presents a setup suitable for double species experiments with ultracold sodium and lithium gases. Our ultracold atom machine very much follows the standard textbook laser cooling approach, having the additional possibility of cooling a second species. The strength of this machine is the availability of several species-selective optical dipole traps, the corresponding knowledge of manipulation and detection of external states in these potentials and the ability to change the lithium isotope from a fermionic to a bosonic one. As the setup has been described extensively before [50–52], I will only highlight the changes performed within the last years and the aspects relevant for the experiments described in this thesis.
The first section gives a general summary of the employed strategy. In the following sections changes to the setup enabling the measurements this thesis is based on are highlighted. Most of the modifications aimed for an increased stability of the experimental apparatus and the capability of performing impurity physics. These improvements were a substantial part of this thesis work. The vacuum and laser setup were successfully modified to reduce the down time and increase the stability of the experiment. Further the upgrade to capture ^{7}Li as well requires changes on the lithium spectroscopy and MOT setup and an adaption of the spin preparation before loading the gas into the magnetic trap. The ^{7}Li hyperfine structure made several approaches for evaporative cooling in the magnetic trap possible that we tested. An alteration of the optical dipole trap loading sequence and beam shape enables higher atom numbers and stability. Here a magnetic field maximum along the trap beam further increases the atom numbers. Lastly, the adjustment of lithium atom numbers and the imaging system are outlined.

2.1 Overview

All ultracold atom experiments have to be performed in ultra high vacuum, as the atoms have to be decoupled from the environment. In our case a two species oven is used as an atomic beam source, a Zeeman slower setup decreases the velocity of the atoms so that they can be trapped in a double species magneto optical trap (MOT). Subsequent optical pumping is applied to enhance the population of the

trappable hyperfine states. A cloverleaf magnetic trap is used to trap the atoms and cooling of sodium is performed via forced evaporation by a radio frequency knife. The lithium atoms are cooled sympathetically. After evaporatively cooling the atoms to the temperature necessary to trap them in an optical dipole trap at given laser power, they are transferred from the magnetic trap to the optical dipole trap. Further evaporation in the optical dipole trap by reducing the trap depth will cause the sodium atoms to form a BEC. In the next step, experiments can be performed, most of them using a species-selective optical dipole trap for lithium. This potential is created using a standing light wave close to resonance for lithium, which is far off-resonant for sodium and thus does not strongly affect the sodium atoms. Detection is done via absorption imaging. The resonant imaging light pulse blows the cold samples away, so a new sample of atoms is trapped and cooled. These cycles take about half a minute with several seconds break between two subsequent runs for data analysis and reprogramming of the devices.

2.2 Vacuum System

In comparison to the original vacuum setup described in [50], only the oven section was changed during the course of this thesis. The general idea of this atom beam source is to have two individually heated reservoirs, one containing sodium, the other one lithium (see Fig. 2.1). We work at reservoir temperatures of 365 °C for sodium and 380 °C for lithium, respectively. It is at these temperatures that the vapor pressure of the alkali metals gets high enough to create a sufficiently intense atom beam. The reservoirs are connected via a small tube, accounting for the different vapor pressures of the two alkali metals. The lithium reservoir is used as a mixing chamber as well. The atoms leave the oven through a nozzle. In order to prevent clogging, nozzle and mixing tube should be hotter than the reservoirs. These ideas are in analogy to the setup in the Ketterle group described in [53].
Lithium and sodium are alkali metals, which are very reactive. Therefore directly after bringing new material into the vacuum system the surfaces of the alkali chunks are covered with oxides. As our experiments aim at impurity physics, more sodium than lithium is required. Therefore much more sodium (up to 40 g) than lithium is filled into the reservoir. Heating the reservoir will evaporate at least parts of these oxides and dirt on the surface of the oven vacuum chamber and the metal pieces. The heating should be done thoroughly as dirt deteriorates the high vacuum conditions. In case of lithium an oxide cage even prevents evaporation. This bake-out is done using a turbo-molecular pump as the outgassing is enormous and would reduce the ion-pumps' lifetime. For lithium additionally cracking of the oxide shell at temperatures of 550 °C and higher is necessary, opening the way for the pure metal

in the center of the chunk. As copper gaskets may only be heated up to 450 °C, nickel gaskets have to be used at the connection between lithium reservoir and oven. If the cracking and bake-out are done excessively, of course parts of the material will be wasted.
Under regular operation about once a year or more often the oven has to be replaced. In general the oven is not empty but has different issues, which will be detailed below. At an oven output of about 1 g per week, it is reasonable to catch most of the material that cannot reach the experiment area on purpose at a position where it can easily be removed. These atoms have a transversal speed too high to pass the tubes of the differential pumping stages between oven section and glass cell. Sodium and lithium have a high probability of sticking to surfaces at room temperature. Therefore a cold copper piece close to the oven nozzle ($\approx$ 6 cm distance) with an aperture in its center is a solution to this task. This copper plate is the outlet of the oven, being water cooled at the outside. This technique works nicely, but will catch a lot of sodium so that after some operation time the sodium pressure in the part between nozzle and copper plate can be so high that lithium cannot pass any more due to a short mean free path length. This is especially true as the nozzle is kept at 450 °C and the external cooling cannot reach room temperature in this section. Mounting a cleaned spare oven solves this problem, but requires a time consuming bake-out procedure.
Another reason for oven exchanges is bad pressure. In order to save material (sodium, lithium) during the night, the reservoirs are kept at about 100 °C colder temperatures than during active operation. Our standard values are 280 °C for sodium and 300 °C for lithium at night. This heating and cooling can cause stress to the metal parts and flanges. Moreover we observed strong degradation of the sodium cup flanges, where a chemical reaction causing unidentified green material at the outside occurred. The same has been observed by other groups working with sodium [54]. After some time of operation, the atom flux of the oven will be reduced or the pressure in the oven section will rise, making it necessary to exchange the oven.
An additional reason to the above mentioned for an oven exchange instead of a refill is the wear out of the lithium flange. The nickel gasket used to seal the lithium cup is harder than copper, making it necessary to use special stainless steel (316LN-ESU) for the flange. Nevertheless the knife edges of the flanges are blunt after single use if they are not closed carefully and using a torque wrench. Otherwise they need to be recut in the institute's workshop after each refill.

In order to better protect the flanges, we redesigned the oven. In the new design, the cups containing the metal chunks are welded onto the oven, the filling is done via blind flanges on top of the reservoirs. Both sodium and lithium are sealed with nickel gaskets in order to prevent chemical reactions. Getting the flanges further away from the reservoirs reduces thermal stress when changing the reservoir's temperature. The very compact design reduces mechanical stress on the vacuum apparatus and reduces

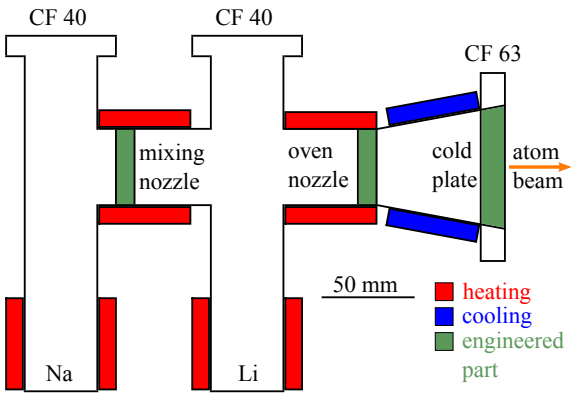

Figure 2.1: New design of the oven setup. The sodium and the lithium cup are heated (365 °C and 380 °C respectively) as well as the mixing and the oven nozzle (450 °C) (red area). The cone is water cooled from outside (blue area). The flanges giving access to the metal reservoirs are as distant as possible from the metal chunks while keeping the volume low. Technical drawings of the green parts are given in [55].

the thermal mass. It has been successfully implemented in the experimental setup. Its end of life was determined by an empty sodium reservoir which could easily be refilled. No corrosion of the flanges was observed.

After passing the copper plate, the atom beam can be blocked by an atomic beam shutter. It is a movable stainless steel metal sheet. This mechanical device is controlled from the outside of the vacuum chamber via a magnetic feed-through. The magnet inside the chamber is attached to a rod that can rotate due to two ball bearings (Lesker, DS450VPS). Attached to the rod is a stainless steel plate that, dependent on its position, either blocks the atoms, increasing the lifetime in the trap or lets them pass, allowing the MOT to load atoms from the oven. In its original version the shutter was mounted directly between oven and six way cross connecting to the rest of the apparatus. It turned out that in this position its lifetime due to sodium clogging of the bearings was short. We mounted the shutter on top of the six way cross, increasing the distance to the oven. Since then the shutter is running smoothly and the bearings never got stuck again.

2.3 Laser System

For the optical cooling of sodium yellow laser light (589 nm, D_2-line transition) is utilized which is generated by a dye laser. The concept of a dye laser is to excite dye molecules solved in a liquid. The dye solution is squeezed through a nozzle at a very high pressure (≈ 20 bar), forming a plane sheet. Excitation is realized with green laser light (532 nm) at high intensity (≈ 10 W) conveniently generated by a solid state laser system, a frequency doubled Nd:YAG laser. The dye molecules end up in a metastable state. Stimulated emission in a ring shaped laser cavity with frequency selective elements creates laser light with a narrow line width (<1 MHz).
For lithium, red laser light (671 nm, D-line transitions) is employed. It is created by a diode laser seeded tapered amplifier, a reliable commercial solid state laser system. It is frequency stabilized using another diode laser that is locked by a Doppler free spectroscopy setup. Besides laser cooling with resonant light we deploy off-resonant lasers for creating potentials (see chapter 3). For the species-selective optical dipole trap close to the lithium transition, red light is generated by a dye laser. The use of a dye laser is advantageous as the wavelength can be tuned widely, the small line width allows to work close to atomic transitions and in principle dye lasers can achieve high output powers and optical fiber coupling efficiencies. For the optical dipole trap confining sodium and lithium, an industrial high power Nd:YAG laser at 1064 nm is available.

The dye laser used for laser cooling of sodium suffered low power, short dye lifetime (less than a week) and mechanical instability. In order to increase the productivity of the experiment, we exchanged the mechanical dye solution pump by a version of Sirah Lasertechnik which is much more powerful than the former one. It has a larger dye solution reservoir and delivers pressures up to 20 bar and higher. At these high pressures a good nozzle is very important, as the surface has to be very even to prevent the formation of ripples on the dye jet. The Sirah nozzle is fabricated from sapphire in a stainless steel body, resulting in the required quality. Furthermore DABCO, a quencher and antioxidant, is added to the dye solution. It improves the dye lifetime. This way the dye solution, which degrades within days without the quencher, lasts about three months. Moreover we exchanged the 10 W pump laser at 532 nm by a new 14 W version of the same model (Laser Quantum Finesse). This additional power makes it possible to increase the pump laser power instead of realigning the laser cavity in case of drifts over the day, yielding more reliable operating hours. In order to keep the pump laser beams free from dust particles which cause flickering, the beam is shielded by tubes. The dye laser itself has its reference cavity inside the housing of the laser cavity. Therefore it turned out to be helpful to turn on the laser control at night, without pump laser and dye circulation, as the heating of the reference cavity is controlled by the main laser control switch.

The change in temperature inside the laser cavity over the day made the system superfluously instable.
Due to the successfully increased stability of the yellow dye laser we bought the same mechanical pump for the red dye laser as well. We could use the 10 W optical pump for the species-selective optical dipole trap dye laser, replacing a Coherent Verdi V10 that was constantly dropping in power and employed our knowledge on handling dye lasers to this system as well.

A further change of the laser setup was the replacement of all hard disk drive based beam shutters. For readout hard disk drives have a very fast moving actuator arm with large travel range where we attached a razor blade. As they have a high momentum they induce vibrations to the optical table and where therefore replaced by relays shutters. They have a smaller travel range. Therefore in the MOT and Zeeman slower beam path we used servo motor driven beam dumps.
Furthermore the electro-optic modulator (EOM) in the sodium slower beam has been replaced by a model with a larger aperture (Qubig EO-Na23). It obviates the telescopes in front and behind the EOM and delivers a much better beam shape, increasing the available cooling laser power by more than 50 mW. In addition we learned that the acousto-optic modulators (AOM) have a strong dependence on temperature. Due to the radio frequency power applied to their crystal they heat up. During the period of magnetic trapping, all AOMs were turned off, letting them cool down again. This leads to reproducible beam positions only after long periods of continuous operation of the experiment. Therefore we changed the control sequence of the power sensitive AOMs (Na MOT, Na slower, Na repumper) in a way that they were turned off only for a few ms. The absolute MOT light intensity proved to be especially critical, which is the reason why we started to control it via a computer driven analog card to enable reliable optimization.

In the next paragraph changes of the lithium laser system are described that aim to increase its stability and to also include the ability to cool ^{7}Li. The lithium setup consists of a diode laser, locked to a spectroscopy cell, and a tapered amplifier system that is frequency stabilized via a beat lock to the spectroscopy laser. In its original version, the spectroscopy laser was current modulated and locked onto the ^{6}Li crossover peak. The beat lock allows for an adaption of the detuning during the MOT sequence, e. g. for a compressed MOT at the end of the MOT loading. The hyperfine splitting of ^{6}Li is 228 MHz (see Fig. 2.2), resulting in a detuning of the spectroscopy laser to the transition of 114 MHz when locking onto the crossover peak. This is compensated e. g. for imaging by an AOM at 81 MHz and a beat lock frequency of 34 MHz. Due to the current modulation of the spectroscopy laser the line width of the diode laser was high and as we wanted to expand the system to ^{7}Li the scheme had to be changed. We implemented a lock pattern analog to the scheme implemented for sodium. In this scheme, the spectroscopy setup is based on saturated

Table 2.1: List of AOM and EOM frequencies of our setup. The sign is giving the used order of diffraction.

	Na ν[MHz]	Li ν[MHz]
MOT	+82	- 80
Repump	+113	+150
Slower	- 200	- 271
Spectroscopy	+70	- 120
Umpump	+76	+24
Umpump Repump	+80	+170
Imaging	+105	- 81
Big AOM	+1699	
Slower EOM	+1713	
^{7}Li Repump		+290

absorption spectroscopy. If probe and pump beam have the same frequency, atoms at rest are addressed. If the two beams are at different frequencies ($\omega_0 - \Delta\omega$ and $\omega_0 + \Delta\omega$) atoms that fly with $v/c = \Delta\omega/\omega_0$ are addressed by the counter propagating beams. In our setup one beam is at the bare laser frequency whereas the other beam is frequency shifted by an AOM in double pass configuration. Therefore if this setup is locked to a resonance, the laser is detuned by the frequency of the AOM. In order to change as little as possible, the spectroscopy AOM in the new setup is running at 120 MHz. In this configuration, the difference in frequency between diode laser and tapered amplifier remains almost the same whatever locking technique is used. This locking scheme can now be used for ^{7}Li as well. The only further change for the MOT that has to be done is to increase the repumper frequency. The hyperfine splitting of ^{7}Li is 804 MHz so the repumper frequency has to be increased by 576 MHz compared to ^{6}Li. This is done via an AOM in double pass configuration at roughly 290 MHz.

2.4 Spin Preparation

The previous section covers the modifications of the lithium laser setup necessary for a ^{7}Li MOT. For further cooling in a magnetic trap additional steps are required. Not all hyperfine states present in a MOT are magnetically trappable. Moreover in a mixture it is important to use stable spin states that do not allow spin exchange between atoms to hyperfine states, which are untrappable.
Fermionic ^{6}Li can be trapped efficiently only in the upper hyperfine state ($F = 3/2$),

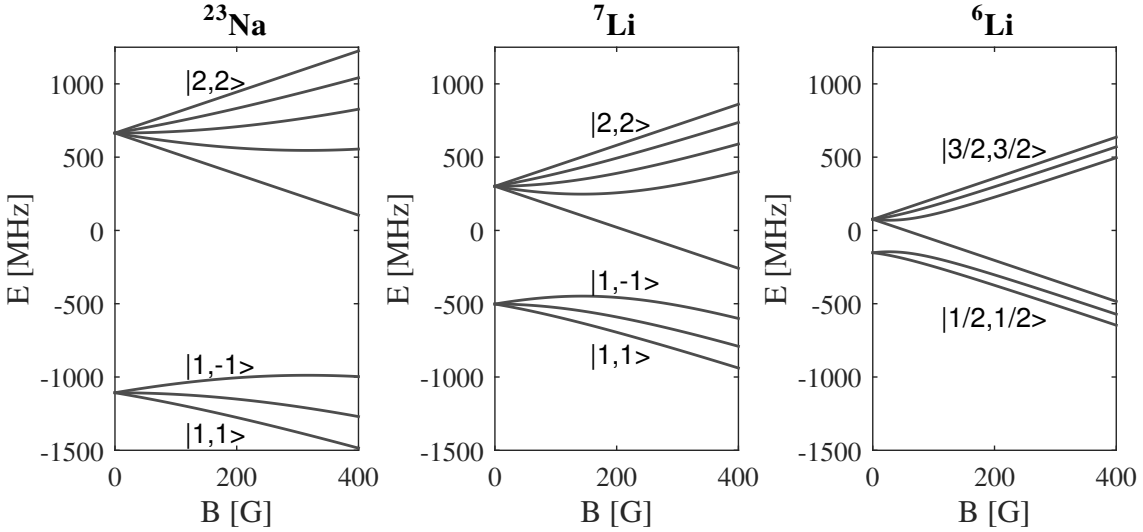

Figure 2.2: Plot of the Breit-Rabi formula for ^{23}Na, ^{6}Li and ^{7}Li [56]. The energy of different hyperfine states depends on the magnetic offset field. Only for small fields the linear Zeeman effect is a suitable description. For strong fields nuclear spin and the electron's spin decouple. Hydrogen-like atoms at intermediate fields and total angular momentum operator $J = 1/2$ can be described analytically by the Breit-Rabi formula.

as the $|F, m_F\rangle = |1/2, -1/2\rangle$ state bends at low magnetic fields, having its maximum at 27 G. The energetically highest hyperfine state $|3/2, 3/2\rangle$ is perfect for trapping ^{6}Li. In order to get a stable mixture, Na has to be prepared in the $|2, 2\rangle$ state, which requires optical pumping for both species at the end of the MOT sequence. The high efficiency of cooling the mixture in the upper hyperfine manifold has been reported [57] and it has been implemented in our setup [50].
For preparing both species in pure spin states by optical pumping, laser beams with two frequencies per species are required. Both beams have circular polarization, shifting the magnetic quantum number into the preferred direction. One beam per species is resonant to the cycling transition, in our lab they are called *umpump* beams. In case the atoms decay into the lower hyperfine manifold, they are repumped into the cycling transition by the second beam type, the *umpump repump* beams. This process lasts about 1 ms and takes place at a magnetic field of 33 G. Fast coils are required for this procedure, as they have to be off for the MOT phase and during optical pumping the atoms are free. So the final field should be present on the timescale of ms. With inclusion of the optical pumping procedure, we can achieve a MOT to magnetic trap transfer efficiency for sodium of about 50 %.
Mixtures of the bosonic isotopes ^{7}Li and ^{23}Na are different from Bose-Fermi mixtures with ^{6}Li, as the hyperfine structure of the two species (Na and ^{7}Li) is the same, immediately suggesting to trap them in the same state. Two states are of interest:

$|2,2\rangle$ and $|1,-1\rangle$. We implemented both to compare their performance.
For ^{7}Li the $|1,-1\rangle$ state can be prepared by turning of the repumping light at the end of the MOT stage. For Na this step is not necessary as we use a dark SPOT MOT [58], trapping most of the atoms in $F = 1$. In a subsequent step the MOT light is turned off and the magnetic trap is ramped up. This way roughly one third of the atoms, the ones in $|1,-1\rangle$ is magnetically trapped. It has been reported that by optical pumping, the number of sodium atoms in $|1,-1\rangle$ can be more than doubled [59]. As the sodium transitions are very close to each other, it is necessary to do the pumping at high magnetic fields (at least 60 G) so that the transition lines are well separated. For the $F = 1$ sodium spin polarization we used the same *umpump repump* frequency as for $F = 2$, but a higher magnetic field. Instead of using the *umpump* beam we set the MOT beams to reduced intensities. The fast magnetic coils can only reach field strengths of 40 G. Hence for higher magnetic fields slow coils have to be added. The empirically found best magnetic field value corresponds to 145 G, but the actual field for the pumping process might be lower, as it probably has not yet reached its steady state. In the end we reached the same sodium pumping efficiency for $F = 1$ as for the preparation in $|2,2\rangle$.
Due to reasons explained in the next paragraph, trapping the mixture in $|2,2\rangle$ is promising as well. In order to pump ^{7}Li into $F = 2$ we employed the beat lock of the lithium laser setup. It is a powerful tool to adjust frequencies dynamically. After the compressed MOT for lithium, the MOT beams are turned off while keeping the repump beams on, putting the ^{7}Li atoms into $F = 2$. Optical pumping is done by applying the same *umpump* beam as for ^{6}Li. In a last step the MOT repumper is turned off. All atoms are in $F = 2$, the ones having had enough cycles with the *umpump* beam in $|2,2\rangle$. Instead of a dedicated *umpump repump* beam for ^{7}Li, we employed the MOT repumper. The efficiency of this scheme is high and trapping both species in $|2,2\rangle$ has several advantages.
To sum up, we can efficiently prepare the bosonic species in the magnetic trap in the lower or the upper hyperfine manifold and compare the specific advantages of these states in the next steps of the experimental cycle.

2.5 Evaporation in the Magnetic Trap

After laser cooling and trapping in a MOT we transfer the atoms into a magnetic trap and cool them evaporatively. More precisely sodium is cooled by forced microwave evaporation and lithium is cooled sympathetically. In free space no magnetic field maxima are possible, making it necessary to trap atoms in low field seeking states. The challenge of constructing a magnetic trap is to find a solution on how to hinder atoms from crossing a $B = 0$ area, in which Majorana losses dominate.

Our magnetic trap is a Ioffe-Pritchard Cloverleaf trap [60], described in [50]. Its coils are embedded in two holders made of synthetic resin. Radial confinement is achieved by a 2D quadrupole field, generated by 4 gradient coils per holder at 400 A. Axial confinement is provided by a pair of coils having an inhomogeneous filed, as the distance between the coils is larger than their radius. This setup results in a curvature of the magnetic field along the coil axis. This pair is called *curvature* coils. Since an offset field at the position of the atoms will reduce the radial confinement, a homogeneous magnetic field is subtracted using a coil pair in Helmholtz configuration, called *antibias*. The *curvature* and the *antibias* coils are driven by one power supply at 220 A, called *curvature*. In order to compensate for mechanical drifts, an additional power supply, called *bias*, driving a current only through the *curvature* coils allows regulation of the offset field at the position of the atoms. As all of these coils have relatively high inductances, another homogeneous coil pair, called *finetune*, with just four windings allows fast magnetic ramps.
Two Zeeman substates in the ground state manifolds are well suited for magnetic trapping of a stable mixture, namely $|1,-1\rangle$ or $|2,2\rangle$ (see Fig. 2.2). Nevertheless several differences arise whether atoms are trapped in $|1,-1\rangle$ or $|2,2\rangle$. In the upper manifold trapping frequencies are twice as high. Furthermore the $|2,2\rangle$ states do not bend, resulting in an theoretically infinitely deep potential. However, several aspects complicate cooling in the upper manifold. An unfavorable feature of the upper hyperfine state for sodium is the higher three-body loss rate of one order of magnitude [61]. As three-body loss scales with the density squared, after reaching cold sample temperatures due to evaporation, the radial confinement of the magnetic trap is reduced in the experiment. For ^{7}Li the disadvantage of trapping in $F = 2$ is the negative scattering length ($a = -27\,a_0$ [62]), resulting in loss at low temperatures and high densities and an instability of the BEC phase. Hence cooling in $F = 1$ provides the advantage that large single species ^{7}Li condensates ($6 \cdot 10^5$ atoms) can be prepared in the magnetic trap by cooling sodium to depletion, which is robust, as the microwave-knife for sodium does not just approach the trap bottom, but crosses it. For further studies the ^{7}Li BECs can easily be transferred into the optical dipole trap.
Another difference of trapping in $|1,-1\rangle$ or $|2,2\rangle$ is the necessary frequency sweep for the evaporation of sodium. When cooling in the upper hyperfine manifold, the transition $|2,2\rangle$ to $|1,1\rangle$ is utilized. In order to cool the samples in $F = 1$ the transition $|1,-1\rangle$ to $|2,-2\rangle$ is best suited. We transferred the frequencies of the $F = 2$ sweep to the corresponding $F = 1$ transition and optimized them empirically. As the final experiments are performed in the lowest hyperfine state, directly after loading the atoms into the optical dipole trap a microwave transfer from $|3/2,3/2\rangle$ to $|1/2,1/2\rangle$ for ^{6}Li and $|2,2\rangle$ to $|1,1\rangle$ for ^{7}Li and ^{23}Na is performed. The final states of this transfer are not magnetically trappable, making it necessary to do the transfer into a purely optical confinement. If the magnetic trapping is done in the lower hyperfine manifold, a rapid adiabatic passage at a low magnetic field and 16.9 MHz

is performed. Its former version is described in [51] and has been slightly modified, as frequency ramps proved to be more robust than magnetic field ramps.
We learned that the radio frequency antennas built in the magnetic coil holders and described in [50] are not perfect to achieve good coupling to the atoms. We used copper wires to build antennas with a few windings and a diameter of about 32 mm. They were put as close to the atoms as possible. Therefore they were mounted between the magnetic coil holders parallel to the glass cell, letting the imaging light pass through their aperture. They strongly increased the Rabi frequency to above $2\pi \cdot 10\,\mathrm{kHz}$.
Nevertheless in our setup cooling in $F = 1$ and $F = 2$ resulted in the same atom numbers for sodium at the end of the magnetic trap and we got better atom numbers for ^{7}Li in $F = 2$, probably due to the increased trapping frequencies and trap depth. The overlap of the clouds and therefore sympathetic cooling of lithium works better in case of high trap frequencies. The gravitational sag scales with ω^{-2} , see Eq. (3.41). For this reason, the experiment is mounted on a vertical breadboard as the radial trap frequencies of the magnetic trap trap are higher than the axial ones, hence it is beneficial to build the setup in a way that gravitation is along the radial direction. Eventually we employed magnetic trapping of all species in the upper hyperfine manifold, which poses many challenges but results in higher atom numbers.

2.6 High Magnetic Field Hybrid Trap

Our experiments take place in a crossed beam optical dipole trap. Due to three-body loss and relative displacements of the magnetic trap minimum at different trap depths due to the cloverleaf configuration, the transfer from magnetic trap to the optical dipole trap can be improved by a smart loading procedure.
Three-body loss strongly depends on the density of the gas. In our experiment there are two situations in which the three-body loss rate for sodium is especially high: in the upper hyperfine manifold and in the vicinity of Feshbach resonances. In these situations the atomic density should be as low as possible. Furthermore we observed that the fluctuating magnetic field at the position of the atoms in the magnetic trap resulted in a high scatter of the sodium atom number and temperature, especially strong at very low temperatures. We decided to build a deep optical trap to transfer the atoms before the microwave knife gets close to the trap bottom.
In the magnetic trap sodium is in $F = 2$, causing high three-body loss. In order to reduce the density, low trap frequencies are required. Combined with a deep trap depth, this necessitates the use of a large beam waist for optical trapping. As the trap depth is proportional to the peak intensity (see Eq. (3.1)), these traps require high laser powers. In our setup, an one-beam trap with a largely elongated potential

is employed for this reason. This configuration circumvents this problem, as it can have a rather small waist, resulting in a deep potential, but the density will not be high, as in one direction atoms are almost free ($\omega \approx 2\pi(700, 700, 1)$Hz for sodium, twice as high for lithium).
In order to avoid heating when reloading the atoms from the magnetic into the optical potential, all trap changes are supposed to be adiabatic, resulting in long timescales. In order to prevent high densities in the experiment, in a first step of the loading procedure the magnetic confinement is reduced in 700 ms. In a subsequent step, the horizontal optical dipole trap beam is ramped up to full power (9 W) in 150 ms. In a further step the radial magnetic confinement can be turned off completely in 400 ms and the axial magnetic confinement is set only by the *curvature* coils and the *bias* power supply. Next, the magnetic confinement is turned off completely in 250 ms and the atoms expand along the optical dipole trap beam. The purely optical trapping enables us to perform the microwave transfer to the lower manifold. The transfers are performed by rapid adiabatic passages where the initial and the final state are coupled via microwave radiation. Either the magnetic field or the radio frequency can be sweeped. Lithium is transferred first by a frequency sweep in 35 ms at a constant magnetic field. Afterwards sodium is transferred using a constant frequency but a magnetic field ramp of 35 ms. Having sodium prepared in $F = 1$, the three-body loss coefficient is one order of magnitude smaller and a second optical dipole trap beam can be applied to increase the density. The atomic cloud has a size of several mm, making it difficult and slow to cool them in this dimple. For this cooling process the intensity of the horizontal beam is linearly reduced in time.
The effectivity of cooling into this dimple can be increased if an additional magnetic confinement in axial direction is applied. The $|1, 1\rangle$ and $|1/2, 1/2\rangle$ hyperfine states, which are the possible final states of the rapid adiabatic passage, are high magnetic field seeking. The *curvature* coils produce a magnetic field minimum, which can be a local field maximum if a homogeneous field is subtracted. In order to do so we used the *curvature* coils and the *bias* power supply plus the homogeneous field of the *finetune* coils. This can only create a field maximum in axial direction at the position of the dimple if one of the fields is inverted to its standard orientation. In order to reverse the current direction of the *bias* power supply, the institute's electronic department built an H bridge consisting of two contactors suited for currents up to 50 A. The mechanical switching takes some time (about 50 ms). Therefore after the microwave transfer a hold time of 250 ms is included. A simultaneous ramp of the *finetune* and *curvature* coils in 100 ms to 40 G and -32 G results in an axial trapping frequency of a few Hz. In a next step the second optical dipole trap beam is ramped up in 100 ms to 2 W and the intensity of both beams is slowly reduced in 5 s to 1 W for the horizontal and 0.4 W for the vertical beam. In the last 100 ms of the optical cooling ramp the magnetic fields are turned off, which is slow and not perfectly controlled. This proved to be disadvantageous for accurate and stable magnetic field in the optical dipole trap, which made waiting times and additional

transfers for magnetically sensitive measurements necessary. The trap frequencies of the final optical dipole trap are $\omega = 2\pi \cdot (155, 102, 220)\,\mathrm{Hz}$ and the corresponding measurements are presented in subsection 3.2.2.
Sodium condensates of $4 \cdot 10^6$ atoms have been achieved using this technique. Furthermore we could store the sodium atoms in this configuration while ramping up a strong homogeneous magnetic field in order to approach the well-known sodium Feshbach resonance at 905 G [63] from high values in order to tune a_{BB} to zero. Atom numbers of about $2 \cdot 10^6$ at these high magnetic fields could be realized this way, whereas crossing the resonance with BECs by magnetic field jumps resulted in strongly enhanced loss.

2.7 Adjusting the Atom Number

All experiments in this theses aim at impurity physics. Therefore we used the maximum possible sodium atom number at varying lithium atom numbers. The sodium MOT is loaded starting from the end of the sequence. The typical loading time constant for a sodium MOT is less than a second, resulting in a saturated MOT after the time the computer control needs to calculate the images, send the control voltages and to program the microwave generator, a time span that is not very well controlled. The lithium MOT has a loading time constant of many seconds. In order to control the lithium atom number, the lithium MOT light is turned off at the beginning of the sequence and reloaded for a defined time, whereas the sodium MOT is loaded without interruption. This well defined lithium MOT loading time correlates with the lithium atom number in the optical dipole trap and allows for its control. Due to the small lithium numbers required for our experiments, the employed loading time is on the order of a second.

2.8 Imaging

We use absorption imaging to detect the atomic clouds. In absorption imaging the atomic cloud is exposed to a pulse of resonant laser light. The atoms scatter photons of the probe light, resulting in reduced intensity at the position of the atoms. For imaging a cycling transition is used. As atoms might end up in the lower manifold, repump light is applied perpendicularly to the imaging direction. The imaging pulse heats the sample up and blows it away. After the camera is read out, the procedure is repeated for a reference image. As the atoms have been removed from the imaging

plane by the first pulse, this time no atoms are in the imaging plane and no light is scattered. If no saturation occurs the intensity of the imaging beam is reduced exponentially (Beer–Lambert law). Therefore the number of atoms can be calculated using the natural logarithm of the two pictures. Using this technique, the spatial information along the imaging beam is lost, as it is integrated out. A commercial objective (Plan-Apochromat S 1,0x, Zeiss) with an effective focal length of 100 mm is used to image the shadow of the cloud onto the chip of an interline CCD camera (RETIGA EXi, Qimaging). In order to have the possibility of imaging sodium and lithium at the same time, the imaging beam is separated by a dichroic mirror after passing the atomic clouds and imaged onto two identically constructed cameras. The magnification of the imaging setup is 2.3, the pixel size of the imaging chip is 6.45 µm. Most information we are interested in is deduced from time-of-flight (TOF) pictures. In this procedure, atoms are released from the trap, letting them fall for the time T_{TOF}. After long times T_{TOF}, the in-situ distribution of the atoms can be neglected and their shape is governed by their momentum. In our system the imaging beam propagates along gravity, making long T_{TOF} possible without compensation of gravitation.
In addition to these high-resolution measurements, for imaging the vertical direction a second imaging setup is implemented. A horizontal laser beam is sent through the bore of the magnetic field coils and imaged by a lens onto a small CCD camera (Guppy, Allied Vision Technologies). It can be used for detection of the atoms at early stages of the cooling process as well as for fluorescence measurements of the MOT. This way the lithium MOT loading rate can be optimized. Exemplary absorption images of our atomic clouds are shown in Fig. 3.3.

3 Optical Traps

When atoms are exposed to an electric field of high intensity, e. g. a laser beam, a dipole moment will be induced, as electrons and protons experience forces in opposed directions. If these fields are inhomogeneous the dipole moment will be pulled in or pushed out of the high intensity regions, depending on its orientation. The dipole potential depends on the optical properties of the two level atom [64]:

$$V_{\mathrm{dip}}(\vec{r}) = \frac{3\pi c^2}{2\omega_0^3}\left(\frac{\Gamma}{\omega-\omega_0}+\frac{\Gamma}{\omega+\omega_0}\right) I(\vec{r}), \tag{3.1}$$

where c is the speed of light, ω_0 is the resonance frequency of the atom's optical transition, Γ is the decay rate of the excited state, ω is the laser frequency and $I(\vec{r})$ the intensity distribution of the laser beam. The sign of the potential depends on the sign of the detuning $(\omega-\omega_0)$. For real atoms approximations are made as not all transitions are taken into account. In our experiments optical potentials are used for trapping atoms and for creating periodic potentials, referred to as lattice.

3.1 Theory: Atoms in Traps

If the intensity in Eq. (3.1) is given by two crossed Gaussian beams, the resulting potential can be well approximated by a 3D harmonic oscillator potential if the distance to the beam center is small:

$$V(x,y,z) = \frac{1}{2}m\left(\omega_x^2x^2+\omega_y^2y^2+\omega_z^2z^2\right), \tag{3.2}$$

with the trapping frequencies ω_i and the mass m. A hot (far from degeneracy) thermal gas in the trap will be well described by the Maxwell–Boltzmann statistics:

$$\langle N_i\rangle = \frac{1}{\mathrm{e}^{(E_i-\mu)/k_{\mathrm{B}}T}}, \tag{3.3}$$

where E_i is the energy of the i-th state, k_{B} is the Boltzmann constant, T the temperature of the sample and μ the chemical potential. For hot gases we can

neglect μ. The virial theorem states that on average over time in a harmonic potential half of the total energy is potential, the other half kinetic energy. As we are interested in the density of the cloud, we will focus on the potential energy. We can now see that the energy distribution $\propto \exp(-E/k_\mathrm{B}T)$ leads to a spatial shape $\propto \exp(-1/2m\omega^2x^2/k_\mathrm{B}T)$. Taking the normalization into account ($\int n \cdot \mathrm{dV} = N$), where N is total particle number of the gas, we know that the density of the gas is given by:

$$n_\mathrm{th}(x,y,z) = \frac{N_\mathrm{th}}{\pi^{3/2} r_{\mathrm{th},x} r_{\mathrm{th},y} r_{\mathrm{th},z}} \, \mathrm{e}^{-\frac{x^2}{r_{\mathrm{th},x}^2} - \frac{y^2}{r_{\mathrm{th},y}^2} - \frac{z^2}{r_{\mathrm{th},z}^2}}. \tag{3.4}$$

Here the width of the Gaussian distribution is not described by $\sigma = r/\sqrt{2}$, but by the most probable distance of an atom to the potential minimum:

$$r_{\mathrm{th},i} = \sqrt{\frac{2k_\mathrm{B}T}{m\omega_i^2}}. \tag{3.5}$$

This can be related to the most probable speed of an atom: $v_\mathrm{p} = \sqrt{2k_\mathrm{B}T/m}$. This classical result has to be modified when temperatures are very low and quantum effects cannot be neglected any more. The following description can be found in many textbooks, see e. g. [65, 66] and is based on the chapter 'Quantitative analysis of density distributions' in [67]. We will now take the particle statistics into account:

$$\langle N_i \rangle = \frac{1}{\mathrm{e}^{(E_i-\mu)/k_\mathrm{B}T} \mp 1}. \tag{3.6}$$

Here the minus sign is for bosons and the plus sign represents fermions. We can use a description via the grand canonical ensemble if we choose μ yielding the correct total particle number:

$$\sum_i \langle N_i \rangle = \langle N \rangle = N. \tag{3.7}$$

We can simplify the problem, assuming that the thermal energy $k_\mathrm{B}T$ is large compared to the harmonic oscillator spacing $\hbar\omega$. In other words, the *de Broglie* wavelengths of particles has to be small compared to the length scale of changes of the potential V. In this case a local description of the gas as a bulk gas is possible. The gas can then be described by a semi-classical distribution function $f_{\boldsymbol{p}}(x,y,z)$. Integration over $\mathrm{d}^3\boldsymbol{p}\mathrm{d}^3\boldsymbol{x}$ gives the number of atoms in the corresponding phase space cell times

$(2\pi\hbar)^3$. Hence the density distribution of a thermal gas is given by:

$$\begin{aligned} n_{\mathrm{th}}(x,y,z) &= \int \frac{1}{(2\pi\hbar)^3} f_{\boldsymbol{p}}(x,y,z)\mathrm{d}^3\boldsymbol{p} \\ &= \int \frac{1}{(2\pi\hbar)^3} \frac{1}{\mathrm{e}^{\left(\boldsymbol{p}^2/2m+V(x,y,z)-\mu\right)/k_{\mathrm{B}}T} \mp 1} \mathrm{d}^3\boldsymbol{p} \\ &= \pm\frac{1}{\lambda_{\mathrm{dB}}^3}\mathrm{Li}_{3/2}\left(\pm\mathrm{e}^{(\mu-V(x,y,z))/k_{\mathrm{B}}T}\right) \\ &= \pm\left(\frac{mk_{\mathrm{B}}T}{2\pi\hbar^2}\right)^{3/2} \cdot \mathrm{Li}_{3/2}\left(\pm\mathrm{e}^{\frac{\mu}{k_{\mathrm{B}}T}}\mathrm{e}^{-\frac{V(x,y,z)}{k_{\mathrm{B}}T}}\right), \end{aligned} \tag{3.8}$$

where λ_{dB} is the *de Broglie* wavelength and $\mathrm{Li}_{3/2}$ is the polylogarithm of order $3/2$,

$$\mathrm{Li}_s(z) \overset{s\neq 0}{=} \frac{1}{\Gamma(s)}\int_0^\infty \mathrm{d}q \frac{q^{s-1}}{\mathrm{e}^q/z-1}. \tag{3.9}$$

It is defined for values of z smaller than 1 ans is depicted in Fig. 3.1. If we assume a harmonic confinement, the spatial integral over the thermal density distribution can be evaluated, giving the number of thermal atoms in the trap:

$$N_{\mathrm{th}} = \int n_{\mathrm{th}}(x,y,z)\mathrm{d}V = \pm\left(\frac{k_{\mathrm{B}}T}{\hbar\bar{\omega}}\right)^3 \mathrm{Li}_3(\pm\mathrm{e}^{\mu/k_{\mathrm{B}}T}), \tag{3.10}$$

where $\bar{\omega} = (\omega_x\omega_y\omega_z)^{1/3}$. We will now focus on bosons. When the temperature of a thermal bosonic gas is reduced, the occupation value $\langle N_0\rangle$ of the lowest state will grow. Therefore μ has to approach 0 from below (see Eq. (3.6) for $E_0 = 0$). Thus, the highest possible density of a thermal bosonic cloud at a given trap potential V and temperature T is obtained at $\mu = 0$ and it has a finite value. If there are more atoms in a trap than a thermal cloud can contain (at a certain temperature), this part of the atoms has to be in the BEC phase. Therefore the critical temperature T_{C}, below which a fraction η_{CF} of the atoms is in the BEC phase, has to depend on the trapping potential and the atom number. We calculated the number of thermal atoms in a harmonic trap in Eq. (3.10). If we set $\mu = 0$ and use $\mathrm{Li}_3(1) = 1.2$, we get $N_{\mathrm{th,\,max}} = (k_{\mathrm{B}}T/\hbar\bar{\omega})^3 \cdot 1.2$. By introducing the critical temperature

$$T_{\mathrm{C}} = 0.94 \cdot \hbar\bar{\omega}N^{1/3}/k_{\mathrm{B}}, \tag{3.11}$$

the highest possible number of thermal bosons in a trap can be expressed as $N_{\mathrm{th,\,max}} = N \cdot T^3/T_{\mathrm{C}}^3$. We can now express the relative fraction of atoms in the condensate $\eta_{\mathrm{CF}} = (N - N_{\mathrm{th}})/N$ depending on the temperature of the sample by:

$$\eta_{\mathrm{CF}} = 1 - \left(\frac{T}{T_{\mathrm{C}}}\right)^3 \tag{3.12}$$

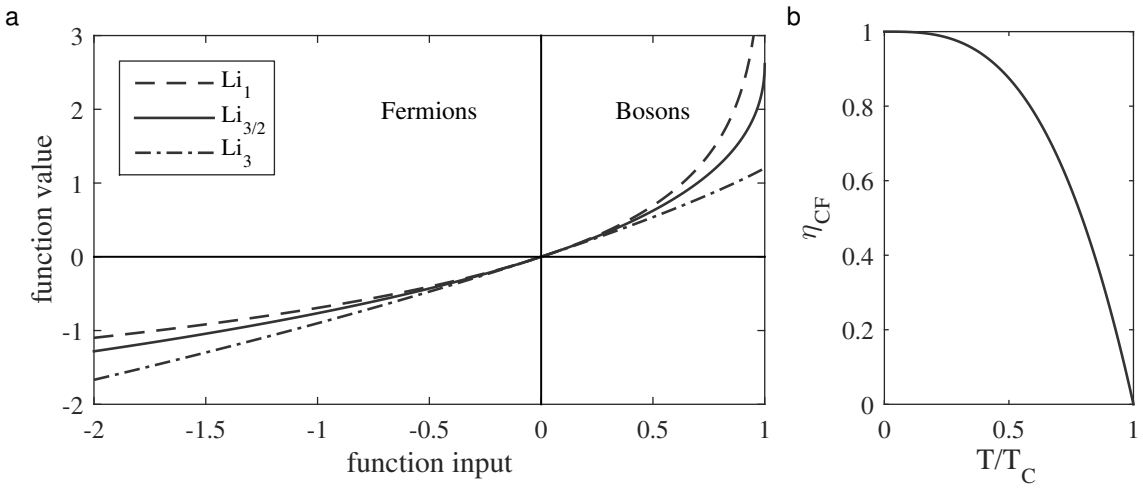

Figure 3.1: a): The polylogarithm of order 1, 3/2 and 3. The first case is useful to calculate 2D densities, the second function is proportional to atomic 3D densities, see Eq. (3.8). Bosons are described by positive input values, fermions by negative values. The polylogarithm of order 3 can be used to calculate the total number of thermal atoms in a harmonic trap, see Eq. (3.10). b): The fraction of condensed atoms η_{CF} over the temperature. A strong dependence on temperature and thus high sensitivity for thermometry is given close to T_C.

Its functional dependence is depicted in Fig. 3.1 b. Note that η_{CF} quickly rises below T_{C} and saturates, resulting in a reduced sensitivity when used for thermometry below $\approx 0.7 T_{\mathrm{C}}$ [68].

For decreasing temperature or increasing density of the gas the interparticle distance will get about equal to the *de Broglie* wavelength of the atoms and bosons will start to macroscopically populate the ground state, forming a BEC. In case of a non-interacting gas, the condensate wave function will be the ground state of the harmonic oscillator:

$$n_{\mathrm{BEC}}(x,y,z) = \frac{N}{a_x a_y a_z \pi^{3/2}} \mathrm{e}^{-\frac{x^2}{a_x^2}-\frac{y^2}{a_y^2}-\frac{z^2}{a_z^2}}; \;\; a_i = \sqrt{\frac{\hbar}{m\omega_i}} \tag{3.13}$$

This expression is used in subsection 5.1.1 to describe single lithium atoms and ^{7}Li BECs, as its interspecies interaction is very weak ($a_{\mathrm{Li,\,Li}} = 7\,a_0$ [69]). If the BEC is interacting, its interaction energy gets easily dominant compared to its kinetic energy. Hence the kinetic term is often neglected. This is called Thomas-Fermi approximation.

Let us now discuss fermionic atoms. Due to the Pauli exclusion principle, at maximum one atom will populate each quantum state. Therefore the energetically lowest state of N fermions in a trap ($T = 0$) is the occupation of the N lowest trap levels. The energy of the highest occupied state is called *Fermi energy* E_F. One can determine a Fermi temperature as $T_\mathrm{F} = E_\mathrm{F}/k_\mathrm{B}$. Cooling a fermionic sample will result in a change of the particle statistics from Maxwell-Boltzmann shape (exponential) to a step function. As this is a smooth process, it is very challenging to use fermions for thermometry in the experiment. On the other hand, even if the precise temperature is unknown, a good estimate for the density distribution can be found. By counting the number of energy levels we can find the Fermi energy for N atoms in a harmonic trap: $E_\mathrm{F} = \hbar\bar{\omega}(6N)^{1/3}$. In a 2D situation like our species-selective optical dipole trap, this changes to: $E_\mathrm{F} = \hbar\bar{\omega}(2N)^{1/2}$ with $\bar{\omega} = \sqrt{\omega_x \cdot \omega_y}$. The chemical potential μ, which has the value E_F at $T = 0$, can be calculated using the Sommerfeld expansion at temperatures $T > 0$ but $T \ll 1$ [70]:

$$\mu(T) = E_\mathrm{F}\left(1 - \frac{\pi^2}{3}\left(\frac{T}{T_\mathrm{F}}\right)^2\right). \tag{3.14}$$

As the occupation of states is known at $T = 0$, the density can be given as well:

$$n_\mathrm{F}(x, y, z) = \frac{1}{6\pi^2}\left(\frac{2m}{\hbar^2}\right)^{3/2}(\mu - V)^{3/2}. \tag{3.15}$$

In a harmonic trap this simplifies to:

$$n_\mathrm{F}(x, y, z) = \frac{8}{\pi^2}\frac{N}{r_{\mathrm{F},x} r_{\mathrm{F},y} r_{\mathrm{F},z}}\left(1 - \frac{x^2}{r_{\mathrm{F},x}^2} - \frac{y^2}{r_{\mathrm{F},y}^2} - \frac{z^2}{r_{\mathrm{F},z}^2}\right)^{3/2} \tag{3.16}$$

$$r_{\mathrm{F},i} = \sqrt{\frac{2E_\mathrm{F}}{m\omega_i^2}} \tag{3.17}$$

where only positive densities are of physical relevance. Please remember that for the validity of the above expressions we assumed that the typical energy is larger than the trap level spacing. At asymmetric traps this assumption can be violated.
Our experiments take place using a species-selective optical dipole potential. It imposes a strong confinement for lithium in one direction, which we will denote as the x-axis. Thermal atoms in 2D can be described semiclassically by a slight modification of Eq. (3.8) [71]:

$$\begin{aligned} n_\mathrm{th}(x, y) &= \pm\frac{1}{\lambda_\mathrm{dB}^2}\mathrm{Li}_1\left(\pm\mathrm{e}^{(\mu - V(x,y))/k_\mathrm{B}T}\right) \\ &= \pm\left(\frac{mk_\mathrm{B}T}{2\pi\hbar^2}\right)\cdot\mathrm{Li}_1\left(\pm\mathrm{e}^{\frac{\mu}{k_\mathrm{B}T}}\mathrm{e}^{-\frac{V(x,y)}{k_\mathrm{B}T}}\right) \end{aligned} \tag{3.18}$$

The polylogarithm of order 1 can be derived from the natural logarithm:

$$\mathrm{Li}_1(z) = -\ln(1-z) \tag{3.19}$$

At this point we are able to describe fermions and thermal bosons in arbitrary potentials if the temperature is known. The only unknown variable we have to approximate and optimize numerically is the chemical potential. This is possible as we have the constraint that the total atom number is fixed. In the net section, we will extend this discussion to interacting bosons.

3.1.1 Weakly Interacting Bosons

The next sections highlight the effects of interaction for clouds of ultracold atoms. In order to understand the interaction properties of cold gases, we should think about typical length scales. In our setup, a typical sodium BEC density is about $5 \times 10^{19}\,\mathrm{m}^{-3}$. This results in an interparticle distance of 270 nm. The corresponding characteristic length scale for the interaction, the scattering length a of the sodium-sodium interaction is $55\,a_0$, corresponding to 3 nm. Therefore such ultracold quantum gases are called dilute and due to low temperatures they are characterized by low-energetic (s-wave) two-body scattering [65]. By reason of the symmetry of the wave functions, for identical bosons the s-wave scattering cross section is $\sigma = 8\pi a^2$, whereas for fermions it vanishes. In case of distinguishable particles, it is $\sigma = 4\pi a^2$. In an effective picture, the van der Waals potential can be described by a contact interaction potential:

$$V = \delta(\vec{r} - \vec{r}\,') \cdot g, \tag{3.20}$$

where $\vec{r}$, $\vec{r}\,'$ is the position of the atoms and $g = 4\pi\hbar^2 a/m$ for identical bosons and $2\pi\hbar^2 a/m_\mathrm{r}$ for distinguishable atoms. The parameter m_r describes the reduced mass of the two-body problem.

3.1.2 Gross-Pitaevskii Equation

The time-independent Gross-Pitaevskii equation [72, 73] has the form of a Schrödinger equation with an additional term $g|\Psi(\vec{r})|^2$, describing the potential of the bosons on themselves.

$$\mu\Psi(\vec{r}) = -\frac{\hbar^2}{2m}\nabla^2\Psi(\vec{r}) + V(\vec{r})\Psi(\vec{r}) + g|\Psi(\vec{r})|^2\Psi(\vec{r}). \tag{3.21}$$

Therefore this equation is non-linear. The Eigenvalues of this equation are called μ, which is not the energy per particle but the total energy of Ψ. In case of no interaction it reduces to the known Schrödinger equation.

In a harmonic trap, kinetic energy increases the size of the cloud whereas potential energy reduces its size, resulting in the characteristic length scale of the harmonic oscillator length $a = \sqrt{\hbar/(m\omega)}$. If (repulsive) interaction is taken into account, it will increase the size of the cloud as well. For realistic experimental conditions it will be dominant compared to the kinetic energy. Therefore the kinetic energy can be neglected at high atom numbers and strong interactions, which is called the Thomas-Fermi approximation [65]. Without the kinetic term the time independent Gross-Pitaevskii equation simplifies to:

$$\mu\Psi(\vec{r}) = V(\vec{r})\Psi(\vec{r}) + g|\Psi(\vec{r})|^2\Psi(\vec{r}). \tag{3.22}$$

The solution of this equation for the density is:

$$n(\vec{r}) = |\Psi(\vec{r})|^2 = \frac{\mu - V(\vec{r})}{g}. \tag{3.23}$$

The physical meaning of this expression is that the external potential is filled with density up to the value of the chemical potential, which is the same situation we found for fermions at $T = 0$. In case of a harmonic trap, this results in a parabola

$$n_{\mathrm{TF}}(x,y,z) = \frac{15}{8\pi r_{\mathrm{TF},x} r_{\mathrm{TF},y} r_{\mathrm{TF},z}} \left(1 - \frac{x^2}{r_{\mathrm{TF},x}^2} - \frac{y^2}{r_{\mathrm{TF},y}^2} - \frac{z^2}{r_{\mathrm{TF},z}^2}\right), \tag{3.24}$$

with Thomas-Fermi radii

$$r_{\mathrm{TF},i} = \sqrt{\frac{2\mu}{m\omega_i^2}}, \tag{3.25}$$

and chemical potential

$$\mu = (15\hbar^2\sqrt{m}N\eta_{\mathrm{CF}}\bar{\omega}^3 a_{\mathrm{BB}})^{2/5}/2. \tag{3.26}$$

In case of an arbitrary potential the density distribution can easily be found by the use of Eq. (3.23). At the edge of the BEC the Thomas-Fermi approximation breaks down as the curvature of the density is strong. In this thesis the effect will be neglected.
In order to apply the Thomas-Fermi description Eq. (3.23) in case of the 2D lattice

situation, we integrate the x-direction out:

$$\begin{aligned} n_{2\mathrm{D}} = \int n_{3\mathrm{D}} dx &= \int \frac{\mu - V(x,y,z)}{g} dx \\ &\approx \int_{-\sqrt{\frac{2(\mu - V(y,z))}{m\omega_x^2}}}^{\sqrt{\frac{2(\mu - V(y,z))}{m\omega_x^2}}} \frac{\mu - (1/2 m\omega_x^2 x^2 + V(y,z))}{g} dx \\ &= \frac{4}{3g}(\mu - V)^{3/2} \sqrt{\frac{2}{m\omega_x^2}} \end{aligned} \tag{3.27}$$

Here we assume the external potential ω_x to be dominant and neglect the effect of the sodium potential in lattice direction.
The observation of border effects raises the question of the length scale on which a BEC in a box can reach its constant value. This length scale ξ is called healing length, as it is the scale on which the BEC can react, can heal in case of a perturbation. Its value is found to be:

$$\xi = \frac{1}{\sqrt{8\pi n a}}, \tag{3.28}$$

where n is the BEC density.

3.1.3 Elementary Excitations

Up to now we treated the BEC like a static matter wave field $\Psi(\vec{r}) = \sqrt{n(\vec{r})}$. However, in this thesis, we are interested in the interaction of impurity atoms with a BEC. Such a field changes the energy of the impurity atom, but there are further effects the condensate causes by this interaction. In order to understand them, we will now study fluctuations of the BEC. We assume that we can still describe the BEC by $\Psi_0 = \sqrt{n(\vec{r})} \exp(-i\mu t/\hbar)$ with a small correction $\hat{\Psi} = \Psi_0 + \delta\hat{\Psi}$. This topic is discussed in the framework of [65, 74]. We expect solutions to be periodic in time and choose the following form:

$$\delta\hat{\Psi}(\vec{r},t) = \sum_{\boldsymbol{q}} \left[u_{\boldsymbol{q}}(\vec{r}) \hat{b}_{\boldsymbol{q}} e^{-i\omega_{\boldsymbol{q}} t} + v^*_{\boldsymbol{q}}(\vec{r}) \hat{b}^\dagger_{\boldsymbol{q}} e^{-i\omega_{\boldsymbol{q}} t} \right] e^{-i\mu t/\hbar}. \tag{3.29}$$

Here $\hat{b}_{\boldsymbol{q}}$ and $\hat{b}^\dagger_{\boldsymbol{q}}$ denote the quasiparticle creation and annihilation operators with momentum $\boldsymbol{q}$ and energy $\hbar\omega_{\boldsymbol{q}}$. We use this ansatz in the time-dependent Gross-Pitaevskii equation

$$-\frac{\hbar^2}{2m}\nabla^2\Psi(\vec{r},t) + V(\vec{r})\Psi(\vec{r},t) + g|\Psi(\vec{r},t)|^2\Psi(\vec{r},t) = i\hbar\frac{\partial\Psi(\vec{r},t)}{\partial t}, \tag{3.30}$$

and linearize the result. We neglect terms in higher orders than linear. If we assume a uniform gas ($V(\vec{r}) = 0, n(\vec{r}) = n$), we can choose plane waves as a solution for $u_{\boldsymbol{q}}$ and $v_{\boldsymbol{q}}$:

$$u_{\boldsymbol{q}}(\vec{r}) = u_{\boldsymbol{q}} \frac{e^{i\boldsymbol{q}\vec{r}}}{\sqrt{V}} \qquad \text{and} \qquad v_{\boldsymbol{q}}(\vec{r}) = v_{\boldsymbol{q}} \frac{e^{i\boldsymbol{q}\vec{r}}}{\sqrt{V}}, \tag{3.31}$$

where V is the volume of the system. We get the Bogoliubov equations

$$\left(\frac{\hbar^2 q^2}{2m} + ng - \hbar\omega \right) u_q - ngv_q = 0, \tag{3.32}$$

$$\left(\frac{\hbar^2 q^2}{2m} + ng + \hbar\omega \right) v_q - ngu_q = 0. \tag{3.33}$$

Introducing the free particle energy $\epsilon_q = \frac{\hbar^2 q^2}{2m}$ and summarizing the two conditions we get

$$\hbar\omega = \sqrt{\epsilon_q^2 + 2ng\epsilon_q}. \tag{3.34}$$

For small momenta q the linear part is dominant, $\hbar\omega \approx \sqrt{ng/m}\hbar q$. Its slope $c = \sqrt{ng/m}$ is the sound velocity. This phonon like spectrum has no curvature, showing a massless character. In this regime a BEC is superfluid. At about $q = 1/\xi$ the dispersion relation starts to bend. For high momenta q the energy is the well know free particle energy plus a mean field energy shift ng. The curvature is the mass of the free particle. So for small momenta the behavior is collective whereas for large momenta single particle effects dominate.

3.1.4 Two Atomic Species Mixtures

In case of a mixture of two BECs, the stationary Gross-Pitaevskii equations of the two clouds get coupled by their density-density interaction. As in this thesis one component is treated as impurity and the other one as bosonic background bath, their densities are denoted by $n_{\mathrm{I}} = |\Phi|^2$ and $n_{\mathrm{B}} = |\Psi|^2$, respectively. Their interaction is characterized by g_{IB}. In general the external potential for the two components is not the same due to different atomic properties (see Eq. (3.1)), therefore they are called V_{I} and V_{B}. For this two-component case, the system can be described by two coupled Gross-Pitaevskii equations

$$\begin{aligned}
\mu\Psi(\vec{r}) &= -\frac{\hbar^2}{2m_{\mathrm{B}}}\nabla^2\Psi(\vec{r}) + V_{\mathrm{B}}(\vec{r})\Psi(\vec{r}) + g_{\mathrm{BB}}|\Psi(\vec{r})|^2\Psi(\vec{r}) + g_{\mathrm{IB}}|\Phi(\vec{r})|^2\Psi(\vec{r}) \\
\mu\Phi(\vec{r}) &= -\frac{\hbar^2}{2m_{\mathrm{I}}}\nabla^2\Phi(\vec{r}) + V_{\mathrm{I}}(\vec{r})\Phi(\vec{r}) + g_{\mathrm{II}}|\Phi(\vec{r})|^2\Phi(\vec{r}) + g_{\mathrm{IB}}|\Psi(\vec{r})|^2\Phi(\vec{r}).
\end{aligned} \tag{3.35}$$

With certain assumptions, the system of coupled equations can be simplified. This is discussed in detail in subsection 5.1.1. Depending on the sign and magnitude of $g_{\mathrm{BB}}, g_{\mathrm{IB}}$ and g_{II} a mixture can even get instable due to strong attractive interaction [65].

3.2 Optical Dipole Trap

As described in Eq. (3.1), red-detuned light i. e. $\omega < \omega_0$ can be used for trapping of atoms. For trapping with blue detuning it would be necessary to build a container of light intensity. As the potential depth is proportional to the intensity, in practical applications laser beams with high power and small beam waists are used. For the cold temperatures achievable with laser-cooled and magnetically trapped atoms, even such optical traps can confine atoms despite their finite potential depths. In our experiment the atoms are cooled in the magnetic trap before they are loaded into the optical trap. As intensity gradients exert a force on the atoms, either several beams are used for trapping or one focused beam with small waist and therefore short Rayleigh length is suited for trapping. One of the advantages of trapping in one beam is its simplicity, the reliable and precise intersection of laser beams of small size is challenging. In general the disadvantage of a one beam trap is the weak potential along the beam direction.

3.2.1 Setup

In our lab the optical trapping is realized by two crossed laser beams at $\lambda = 1064\,\mathrm{nm}$. One beam is horizontal and has a waist of about $w = 60\,\mu\mathrm{m}$. The second beam is perpendicular to the first one and has an orientation of 49° to gravity. Its waist is about $w = 80\,\mu\mathrm{m}$. The power of the horizontal beam is about 9 W, the power of the vertical one about 2 W. The last mirror of the optical dipole trap laser beams have piezo actuators, allowing for the computer-controlled positioning of the optical dipole trap. As the Nd:YAG laser is sent to the atoms without fibers, drifts of laser beam pointing or mechanical drift of optics close to the laser will change the optical dipole trap position. We observed that during a work day the overlap of the beams has to be realigned several times. We scan the vertical position of the vertical beam by the piezo mirror, optimizing the atom number.

3.2.2 Trapping Frequencies

The potential of a Gaussian laser beam can be approximated by a harmonic potential, which is a very good approximation for small displacements of the atoms from the center of the beam. By a sudden shift of the confining potential, oscillations in this optical potential can be induced. In order to probe the harmonic part, small oscillation amplitudes are desirable. Therefore they are difficult to observe in-situ, but the momentum of these oscillations can be detected by taking time-of-flight pictures. As it is much easier for us to detect sodium samples after long time of flight (BEC phase and high atom numbers), the lithium values can be calculated from the sodium numbers by Eq. (3.1), taking only for the D-line transitions into account. We are interested in the initial trap, defined by two intersecting laser beams. Therefore one of the beams is slowly deflected and suddenly set back to its original position. This way we can induce oscillations in the combined optical dipole trap. The confinement is described by a 3D harmonic oscillator with three orthogonal axes. The first axis, called x-direction, is orientated along the horizontal optical dipole trap beam and the trapping potential is given by the vertical optical dipole trap beam. The second axis, called y-axis, is pointing along the vertical beam and determined by the potential of the horizontal beam. The third direction (z-axis) is perpendicular to the x- and y-axes. As the vertical beam has an angle of 49° to gravity, y and z have a component along gravity. A typical oscillation measurement is shown in Fig. 3.2. Only the measurement of the x-direction is performed using

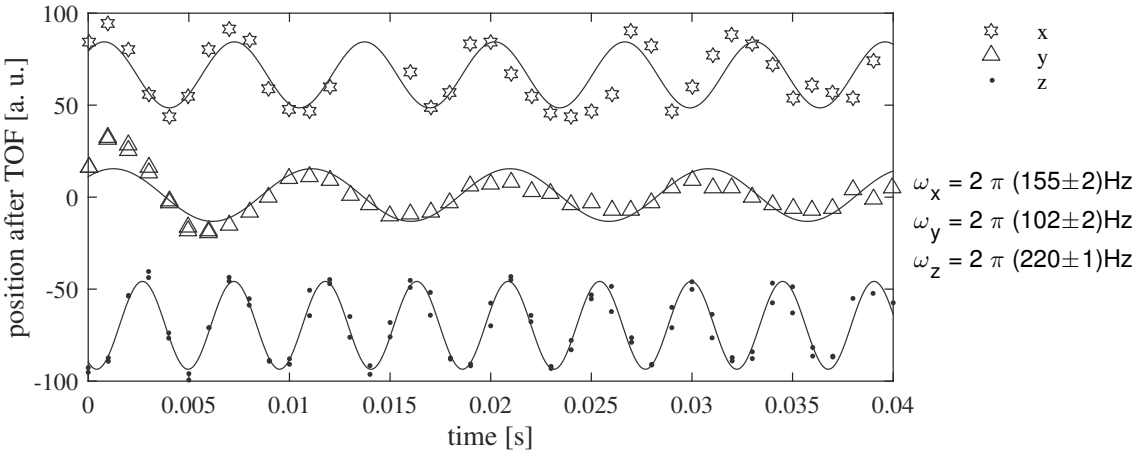

Figure 3.2: A sudden shift of the optical dipole trap position causes the sodium cloud to oscillate. This oscillation is detected by absorption images after time-of-flight. In y-direction inharmonic parts of the potential are probed and damping can be observed. The uncertainties correspond to the 68 % confidence levels of the fit.

the usual imaging. For the y- and z-axis the vertical imaging is used. The y- and z-oscillation can be excited separately or in a combined fashion. For a pure $y(z)$ oscillation the horizontal (vertical) beam has to be deflected along the vertical beam (in vertical direction). For a combined y-z oscillation the horizontal beam can be deflected in horizontal direction. As the orientation of the vertical beam is almost 45°, either the images can be rotated by 49° or the coordinate transformation can be done by adding the center of mass coordinate in the two image directions and by subtracting it. All methods lead to the same results.
The potential of a Gaussian beam is expected to be invariant under rotation. In that case, the trap frequency in z-direction should be $\sqrt{(155\,\mathrm{Hz})^2 + (102\,\mathrm{Hz})^2} = 186\,\mathrm{Hz}$, which is not even close to the measured 220 Hz. The reason is the orientation-dependent divergence of the trapping laser beam. The focus of the beam behind the spherical lens is displaced by several mm in horizontal compared to vertical direction. Further the waist in horizontal and vertical direction is not the same. When the trapping frequencies for sodium are known, the ones for lithium can be calculated using Eq. (3.1). For ^{6}Li the ratio is 2.25, for ^{7}Li it is 2.08. The relevant atomic properties can be found in [75–77].

3.2.3 Temperature Measurements

The free expansion of fermionic clouds below the Fermi temperature only weakly depends on temperature. Therefore we will focus on the bosonic species in this subsection. At temperatures below T_C a bosonic sample will be bimodal, having a thermal part and a part in BEC phase (see section 3.1). In time-of-flight pictures, which are taken after a free expansion time of T_TOF, a BEC has the shape of a 3D-parabola, whereas the thermal sample has a Gaussian shape. All statements on BECs in this paragraph are based on the Thomas-Fermi approximation. The free expansion of a thermal cloud is given by its momenta due to their thermal energy, making the size of the cloud dependent on the temperature. Furthermore the fraction of atoms in the BEC η_CF depends on the temperature (see section 3.1). Therefore one can measure temperature by taking time-of-flight pictures of bimodal distributions. The pictures are summed up in one direction, resulting in profiles. The wings of these profiles are fitted by a Gaussian line. The width of the Gaussian distribution is characterized by σ. In order to prevent confusion, I would like to mention that $FWHM = \sigma \cdot 2\sqrt{2\ln(2)} \approx 2.4\sigma$. If the magnification of the imaging system is known, this can be used to calculate the absolute temperature:

$$T = \frac{m\sigma^2}{k_\mathrm{B} T_\mathrm{TOF}^2} \tag{3.36}$$

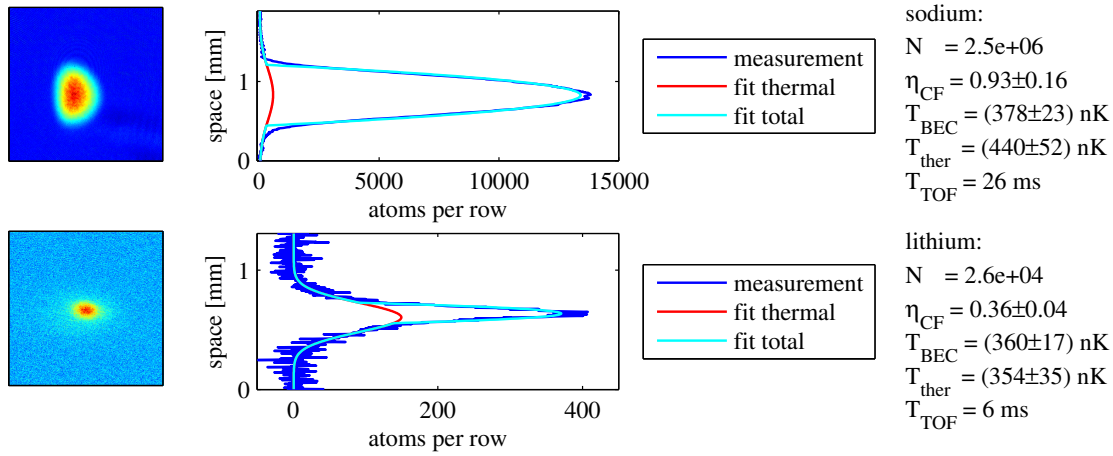

Figure 3.3: Exemplary absorption images for temperature determination. The upper row shows a sodium time-of-flight picture, the lower one a picture of ^{7}Li, taken in the same experimental run. The vertical optical dipole trap beam causes some distortion of the sodium BEC, thus the images are evaluated along the horizontal optical dipole trap beam. In order to do so they are integrated, yielding the profiles in blue. The outer parts are fitted by a Gaussian (red) and correspond to the thermal atoms. The difference of the measured profile to the thermal distribution is the BEC and can be fitted by a parabola. The sum of thermal fit and BEC fit are shown in cyan. For sodium it is very challenging to fit the thermal wing as it is vanishingly low, causing strong dependence on the part of the profile that is used for the fit. All numbers of interest are given on the right.

The difference of the fit and the absorption profile is calculated and should yield a parabola. It is fitted as well and the integral is calculated. The two fit functions can be used to calculate the relative fraction of atoms in the BEC η_{CF}. This can be used to calculate the absolute temperature (see Eq. (3.12)):

$$T = \frac{0.94\hbar\bar{\omega}N^{1/3}}{k_{\mathrm{B}}}\left(1-\eta_{\mathrm{CF}}\right)^{1/3}. \tag{3.37}$$

Here it is necessary to know the corresponding trap frequencies. In our case this is especially challenging, as the sodium cloud strongly modifies the lithium potential. Numerical tests of the situation revealed that the above formula is nevertheless a very good approximation. This can be improved if sodium is removed from the trap after the final cooling step. The momentum distribution of the BEC atoms is given by the chemical potential μ. Therefore the size of the BEC can be used to deduce its value. In general, the sensitivity is highest slightly below the critical temperature. In

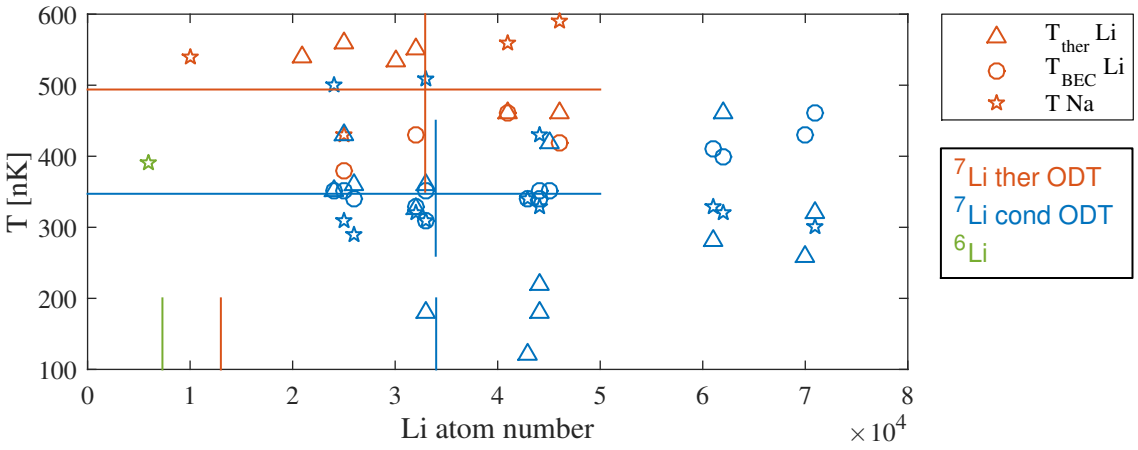

Figure 3.4: Summary of temperature measurements. Three situations are especially interesting for us: fermionic impurities (green), bosonic clouds with and without curved magnetic field to enhance cooling (blue and red). The temperatures deduced from the ^{7}Li image by η_{CF}, thermal size and from the sodium profile are plotted. Vertical bars on the x-axis indicate typical experimental atom numbers. The crossed lines show mean values where the length of the lines display the parameter range taken into consideration.

our case a temperature measurement using time-of-flight is challenging as the critical temperature for sodium is about 730 nK, the actual temperature is roughly 350 nK, resulting in $\eta_{\mathrm{CF}} = 0.9$. In this case after long T_{TOF} it is difficult to differentiate between a fringe due to imperfect imaging and some thermal background. Long T_{TOF} are required to resolve the sodium atom number in the BEC, as in-situ or after short time of flight the clouds have a high optical density. For this reason ^{7}Li is a perfect thermometer. The critical temperature T_{C} depends on the atom number (see Eq. (3.11)). As we can choose the lithium atom number we want to work with, the critical temperature can be set to an optimal value. The error in T is dominated by the contribution of the uncertainty of the Gaussian fit. For the temperature deduced from the thermal cloud only the width of the distribution σ is relevant. For the calculation of η_{CF}, σ and the amplitude of the fit have to be taken into account. The uncertainty of $\bar{\omega}$ is small compared to it.

In Fig. 3.4 all thermometry measurements are displayed. No individual error bars are shown, as the huge stray of temperature values gives an impression about the confidence level of this approach. In case of ^{6}Li only sodium is used to deduce the temperature, which is not very precise. Therefore it is plausible to assume it has the same temperature as in the cold bosonic case. For ^{7}Li and the curved magnetic field applied during cooling in the optical dipole trap (blue) the three approaches converge

to 350 nK. Extreme temperature values and lithium atom numbers are not taken into account. The trusted area is visualized by the extent of the lines. The position of the lines indicate the mean values. For the case without magnetically enhanced trapping the values calculated by the condensate fraction differ from the ones for sodium and the ones derived from the size of the thermal cloud (red). The mean value is 500 nK. For high lithium atom numbers the temperature values from the condensate fraction increase, an effect not observed on sodium or on the temperature derived from thermal expansion.

3.3 Density Distribution of a Two-Species Mixture

The experiments this thesis aims at are based on density-density interaction. In our setup it is crucial to understand the density distribution of the two species, which we cannot observe directly due to the high densities and the small spatial length scales. When the distributions are known, all relevant parameters can be extracted.

3.3.1 Key Parameters

The impurity-BEC coupling we are interested in is density dependent. In our case the BEC density is strongly non-uniform. Therefore we describe the BEC density by the concept of the effective density [48, 52]. It is the mean value of the sodium density the lithium atoms probe:

$$\bar{n}_{\mathrm{Na}} = \frac{1}{N_{\mathrm{Li}}} \int n_{\mathrm{Na}} n_{\mathrm{Li}} \mathrm{d}V \tag{3.38}$$

It can be applied to the sodium density using n_{Na} and the BEC density integrating over $n_{\mathrm{Na,\,BEC}}$. In case of ^{7}Li we will be interested in the effective sodium BEC density which the lithium BEC probes, so one could replace n_{Li} by $n_{\mathrm{Li,\,BEC}}$. In order to prevent confusion, all given effective densities in this document refer to the above given definition.
Another helpful estimate of the geometrical distribution is the immersed fraction. Its value gives the fraction of lithium atoms that are inside the sodium BEC:

$$\eta_{\mathrm{im}} = \frac{1}{N_{\mathrm{Li}}} \int n_{\mathrm{Li}}(\mu_{\mathrm{Na}} > V_{\mathrm{Na}}) \mathrm{d}V \tag{3.39}$$

In Thomas-Fermi approximation all voxel with $\mu_{\mathrm{Na}} > V_{\mathrm{Na}}$ have a finite sodium BEC density. Therefore this condition can be used to calculate the immersed fraction. In

case of ^{7}Li we will see that we need to know the 2D density of condensed impurity atoms. Again we need to average over the sample. This can be expressed in the following way:

$$\bar{n}^{\mathrm{2D}}_{\mathrm{Li,\,BEC}} = \frac{1}{N_{\mathrm{Li}}} \int (n_{\mathrm{Li,\,BEC}})^2 \,\mathrm{d}A \tag{3.40}$$

3.3.2 Differential Gravitational Sag

Up to now we have not discussed effects of gravity. Its linear contribution to the harmonic potential will cause a spatial shift of the minimum by $\Delta_{\mathrm{GS}} = g_0/\omega^2$ where g_0 is the gravitational acceleration constant and ω the trap frequency in direction of gravity. In general a shift can be neglected if the harmonic approximation is still valid at the displacement Δ_{GS} from the trap center, but due to different masses and trap frequencies, in our setup a differential shift occurs. It can be easily calculated projecting gravity onto the effective trapping potential along gravity. As introduced in subsection 3.2.2 the x-axis points along the horizontal beam, y-axis along the vertical beam and z-axis is perpendicular and therefore y and z-axes are orientated opposite to gravity. The angle α between gravity and the vertical beam is 49°. Effectively, this shift is given by

$$\Delta_{\mathrm{DGS}}(x,y,z) = \left(0, g\cos(\alpha)(1/\omega^2_{\mathrm{Na},y} - 1/\omega^2_{\mathrm{Li},y}), g\sin(\alpha)(1/\omega^2_{\mathrm{Na},z}, -1/\omega^2_{\mathrm{Li},z})\right). \tag{3.41}$$

The displacement of the lithium cloud compared to the sodium cloud is about $\Delta_{\mathrm{DGS}}(x,y,z) \approx (0, 13, 3)\,\mu\mathrm{m}$, which is a shift uphill.

3.3.3 Density Distribution in the Optical Dipole Trap

Now we can address the question of how the density distribution of the two-component mixture looks like in the optical dipole trap. In summary the relevant parameters are: the atom numbers N_{Na} and N_{Li} which are determined by absorption imaging, the trapping potential of the optical dipole trap and the temperature T (see subsection 3.2.3). We can calculate the full external potential for sodium $V^{\mathrm{ext}}_{\mathrm{Na}}(\vec{r})$ and lithium $V^{\mathrm{ext}}_{\mathrm{Li}}(\vec{r})$. It is not the same for the two species due to different atomic properties. We will take the effect of sodium on lithium into account, neglecting the effect of lithium on the sodium distribution. This is sensible as the interaction is density mediated and the sodium density is much higher than the lithium one.
So our calculation starts with the sodium distribution. Our experiments take place below T_{C} for sodium, so a part of the atoms is condensed, a part is thermal. For

a harmonic trap all relevant analytic expressions are given in section 3.1. Here the numerical method is explained which has the same physical basis but can be used for arbitrary potentials. This is useful, as the potential $V_{\mathrm{Na}}^{\mathrm{ext}}(\vec{r})$ is not harmonic in the presence of the periodic species selective potential (lattice). We will discuss its impact on the density distribution in the following section and its application in chapter 4. For the numerics we use a grid of $1000 \cdot 100 \cdot 100$ voxel. The increased sampling is used in direction of the lattice, which slices the lithium cloud along the horizontal dipole trap beam.
We get the thermal sodium density distribution using the polylogarithm, see Eq. (3.8) and setting $\mu = 0$. For vanishing μ the highest thermal bosonic densities are obtained (see Fig. 3.1). In a next step, this density distribution is integrated over space and the number of thermal atoms is determined. The missing atoms $N - N_{\mathrm{th}}$ are in the BEC phase. They are distributed over the numerical grid using Thomas-Fermi approximation (see Eq. (3.23)). In this case we need to know μ, which we determine numerically by testing if the applied chemical potential results in the correct atom number in the BEC. The sodium-sodium scattering length is set to $54.54\,a_0$ [78]. As a result of this procedure, we obtain the sodium density of all grid points, describing our system.

For lithium, we will add the interspecies interaction potential to the external potential $V_{\mathrm{Li}}^{\mathrm{ext}}(\vec{r})$. In case of fermionic ^{6}Li it is attractive ($a_{\mathrm{Na\,Li}} = -75\,a_0$), in case of bosonic ^{7}Li it is weakly repulsive ($a_{\mathrm{Na\,Li}} = 21\,a_0$) [79]. All experiments are performed in the energetically lowest hyperfine state. The potential for lithium is $V_{\mathrm{Li}}^{\mathrm{eff}} = V_{\mathrm{Li}}^{\mathrm{ext}} + g_{\mathrm{IB}} n_{\mathrm{Na}}$. For thermal ^{7}Li and for ^{6}Li we get the density distribution using the polylogarithm. For fermions the starting value for μ is based on the Sommerfeld expansion. For bosons the thermal distribution for $\mu = 0$ is calculated and the resulting atom number is obtained. If this test distribution has too many atoms, there is no BEC and the correct value for μ is searched iteratively. If an additional BEC is necessary, it is calculated using Thomas-Fermi approximation and searching the corresponding μ numerically. The lithium intra-species scattering length is set to $7\,a_0$ [69]. This way the lithium density can be calculated.

Fig. 3.5 shows the obtained density distribution for ^{6}Li. In the upper row images with the same perspective as in the lab are shown. Here gravity is integrated out. The left side displays the sodium cloud, the right side the lithium distribution. Both pictures show the same volume. On the right side the profiles in lattice direction are shown. A small thermal part of sodium can be seen. The sodium BEC is well described by a parabola. ^{6}Li is pulled into the sodium cloud, but the effective potential is not deep enough to store all fermions, although the bosonic peak column density is about 250 times higher than the fermionic one. The lower row shows images corresponding an acquisition through the bore of the magnetic coils ($\vec{g}$ is pointing downwards). Lithium is shifted upwards and exploring the vertical optical dipole trap beam in uphill direction. The fraction of lithium atoms within the BEC η_{im} is about

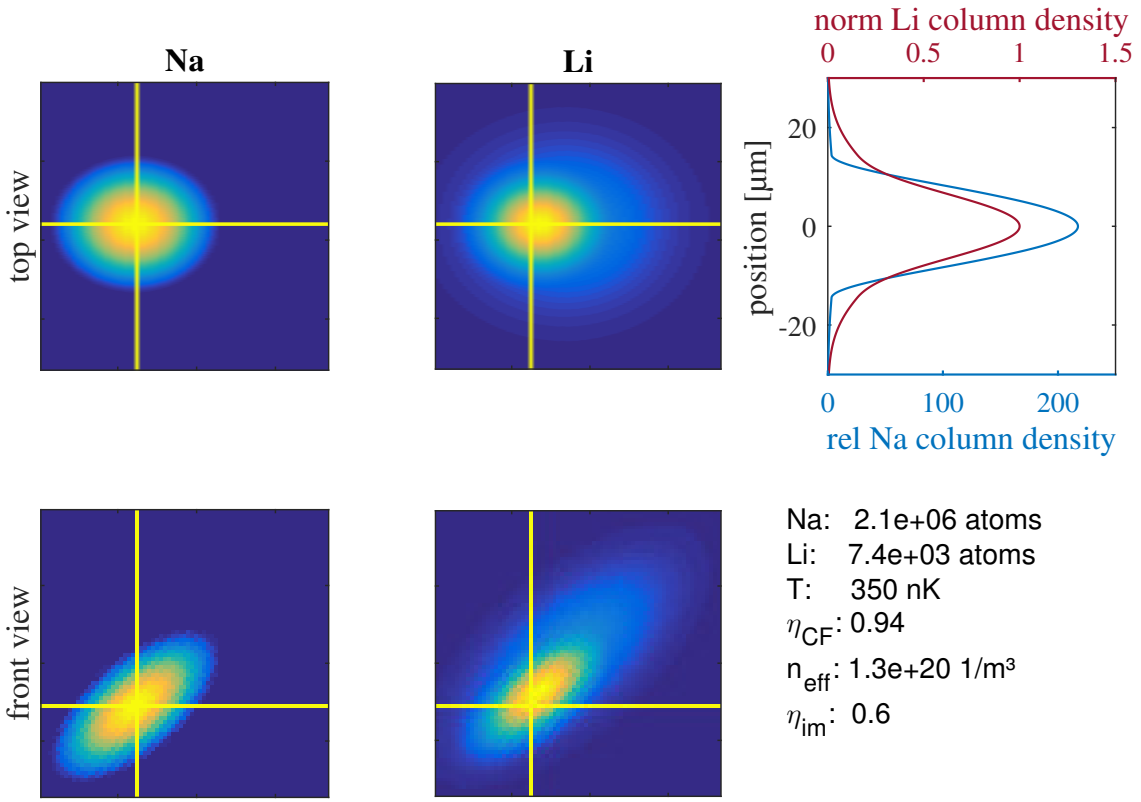

Figure 3.5: The calculated sodium and ^{6}Li density in the optical dipole trap for typical experimental parameters. The upper row integrates along gravity, the lower one in horizontal direction. The crossed lines indicate the center of the sodium BEC. The lithium profile (red) in the right-hand panel is normalized to 1 and the sodium (blue) profile is given in relative units to the lithium profile. The field of view has a size of 60 µm × 60 µm × 60 µm.

0.6. This has to be regarded as a great progress compared to former experiments ($N_{\mathrm{Na}} = 5 \cdot 10^5$,$N_{\mathrm{Li}} = 2 \cdot 10^5$,$T = 600\,\mathrm{nK}$,$\eta_{\mathrm{CF}} = 0.6$, [48]). The fundamental difference of fermions to bosons is noticeable. A few thousand fermions form a larger cloud than a million bosons in a BEC.

Fig. 3.6 shows the density calculations plotted the same way for ^{7}Li. Two typical scenarios are plotted, which differ in atom numbers and temperature. For one scenario, the the High Field Hybrid Trap technique is used (see section 2.6) is used, whereas in the other case the cooling into the dimple is not enhanced by a magnetic field. We used this technique as a knob to generate either a condensed or a purely thermal ^{7}Li cloud in the optical dipole trap. The upper part of the figure shows the thermal case. As the ^{7}Li cloud is not attracted by sodium, it is rather large and pushed out of the BEC. Therefore the immersed fraction η_{im} is only about 20 % and

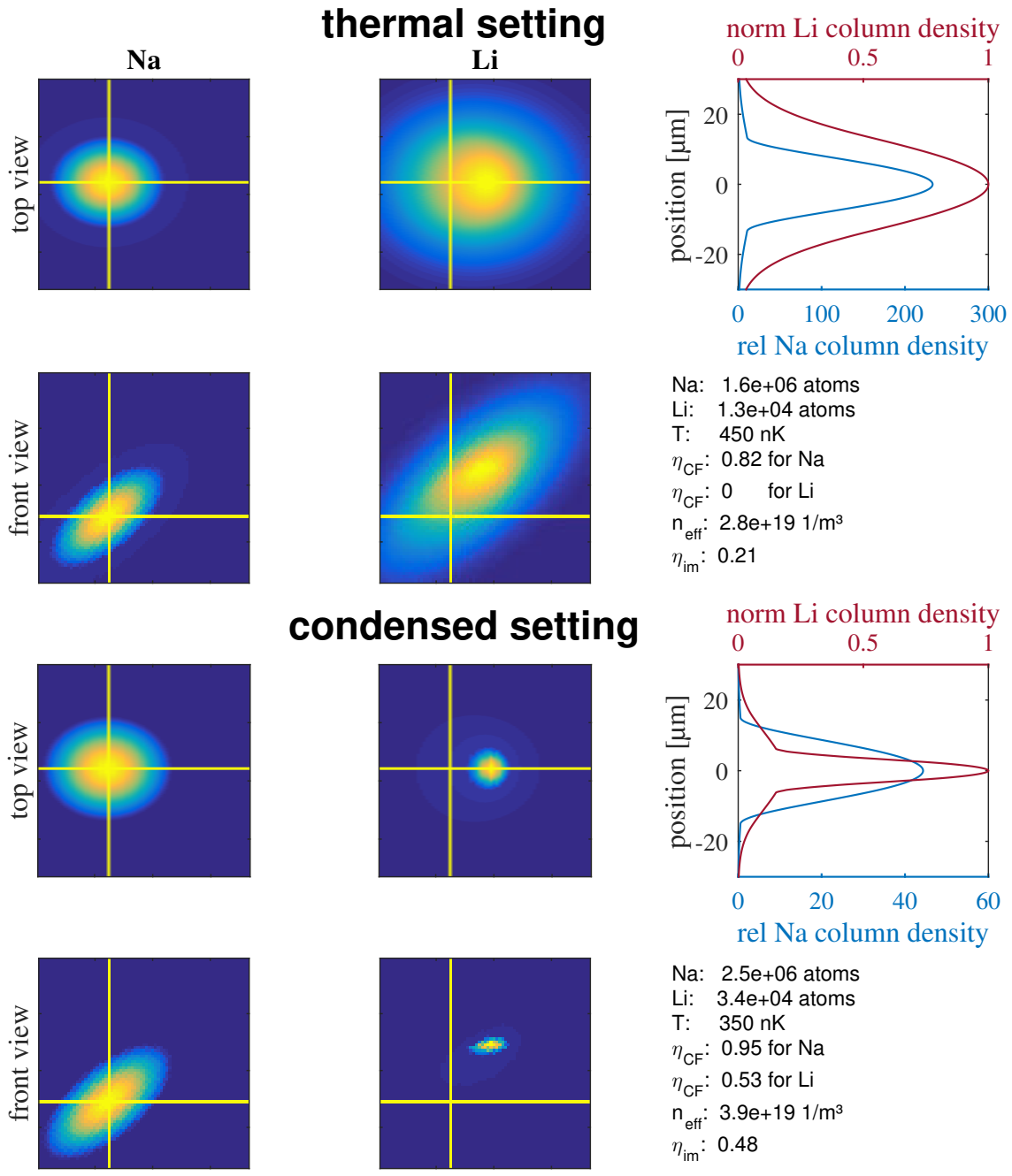

Figure 3.6: The calculated sodium and ^{7}Li density in the optical dipole trap for two sets of typical experimental parameters. Plotting is analogous to the fermionic case. For the upper scenario ^{7}Li is purely thermal. In the lower one the atom numbers are increased, temperature is decreased, causing the formation of a lithium BEC.

the effective density is about a factor of 5 lower than in the fermionic case shown before.
In case of lithium condensation, the density distribution is very different. The lithium atom number is higher, resulting in condensation of about half the lithium atoms. As a BEC is very compact, especially in Thomas-Fermi approximation at low interaction strength, the lithium column density increases dramatically and is just 40 times lower than the sodium one. The use of the High Field Hybrid Trap technique increases the number of sodium atoms by a factor of 1.6, which causes only slight changes in the sodium BEC size. The effective density is rather constant, as the lithium BEC forms at the border of the sodium BEC. In the profile in lattice direction this displacement cannot be observed. Only the transversal image shows the shift of lithium to the border of the sodium BEC, resulting in a reduction of $\bar{n}$ compared to the fermionic case. As the lithium BEC is floating on the sodium BEC, the immersed fraction rises to 0.5. The lithium profile nicely shows the bimodal distribution.

3.3.4 Density Distribution with Additional Species-Selective Potential

So far, we have only calculated the density distribution in the presence of an almost species independent optical trapping potential. However, for our experiments we use a standing light wave potential which is much stronger for lithium than for sodium. It will be described in more detail in chapter 4 and creates a sine potential along the x-direction of our experimental system

$$V_{\mathrm{SSODT}} = V_0 \cdot \sin\left(\frac{2\pi}{3.3\,\mu\mathrm{m}}x\right)^2. \tag{3.42}$$

We know very precisely the energy gap of ground to first excited state for lithium in the lattice (see subsection 4.4.2), and the wavelength of the generating laser (670 nm to 672 nm). The first information allows for a determination of V_0 for lithium and using Eq. (3.1) its corresponding value for sodium can be calculated. Due to the about 100 times stronger confinement for lithium along the standing wave potential, the lattice will cause the formation of an array of independent pancakes and higher peak densities compared to the optical dipole trap density distribution. For fermions this will result in slightly larger radii and for bosons this can cause Bose-Einstein condensation. Therefore the lattice can dramatically change the density distribution and should be taken into account. Please note that for lithium the lattice can be attractive and repulsive ($\lambda_0 = 671\,\mathrm{nm}$), whereas it is always attractive for sodium ($\lambda_0 = 589\,\mathrm{nm}$). Lithium pancakes can be located in sodium density minima or maxima (see section 5.4). Hence the key parameters $\bar{n}$ and η_{im} depend on the wavelength of the lattice.

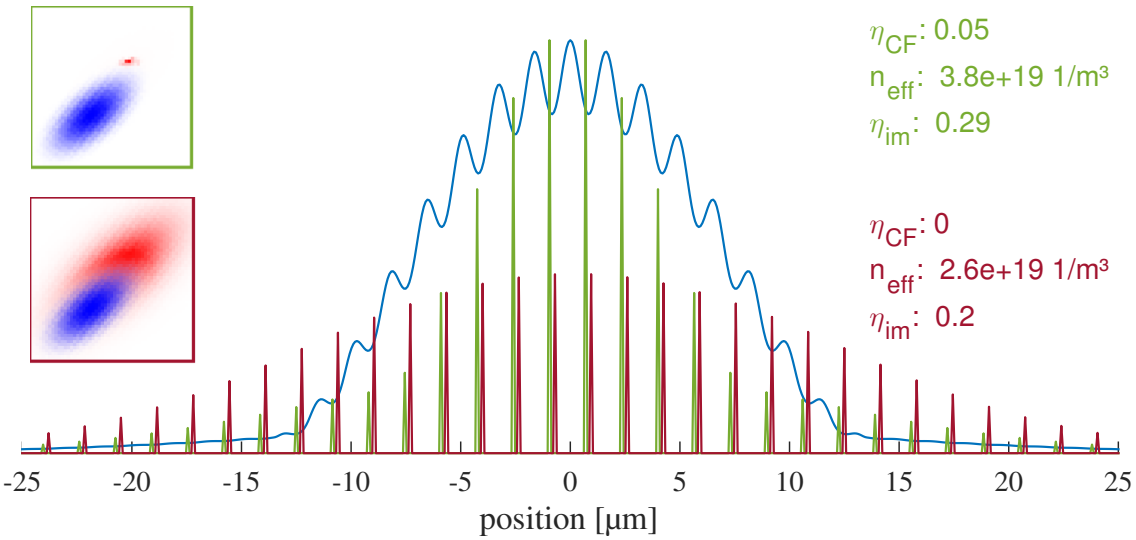

Figure 3.7: Comparison of the two methods to obtain the density distributions of the Na ^{7}Li mixture in the combined potential of dipole trap and standing light wave in the thermal scenario of Fig. 3.6. The lithium profiles are plotted with the normalized sodium profile (blue) for comparison and are displaced to each other for better visualization. The red line corresponds to the technique which distributes the optical dipole trap density over the lattice sites and the green line is the result for an overall chemical potential. The images on the left show the transversal view of the distributions resulting from the two techniques. Here sodium is shown in blue and lithium in red. On the right side the calculated key parameters are denoted.

Up to now we could describe the atomic systems by one chemical potential, implying a connection of different parts of the density distribution. An array of independent lithium clouds does not necessarily have one overall chemical potential. It is possible to calculate the lithium density distribution using a global chemical potential, which corresponds to the ground state of the system. Another possibility is to freeze the optical dipole trap density, allocate lithium atoms to lattice sites and calculate the lithium density for each pancake separately, applying the 2D expressions. This is the other extreme case, assuming that during the adiabatic lattice ramp up, the lithium motion is frozen out. The correct description must be between these two scenarios, while indirect measurements support the second approach. Analyzing our experimental findings (see chapter 6) we observe a strong variation in the signal, whether the bosonic cloud is condensed in the optical dipole trap (before loading the lattice) or not. This can be easily interpreted: a thermal cloud is much larger than a condensed one, so if a BEC is loaded into the lattice, less lattice sites are populated. If we calculate the lithium density distribution using one global chemical potential,

such dynamical effects are not taken into account. Therefore the best way seems to be an initial calculation of the lithium density distribution in the optical dipole trap, the subsequent calculation of the lithium density for every lattice site, taking the full 2D potential into account. In Fig. 6.10 the topic is addressed again.
In Fig. 3.7 the results for both methods are shown. The parameters correspond to the results shown in the upper part of Fig. 3.6, the thermal case. Here the lattice wavelength is set to $\lambda = 670.5\,\mathrm{nm}$, corresponding to a lithium trap frequency of $\omega = 2\pi \cdot 27.25\,\mathrm{kHz}$ in lattice direction. The weak sine potential for sodium causes a periodic modulation also for this species. At this wavelength the potential is attractive for sodium and repulsive for lithium. Hence the lithium pancakes are located in sodium density minima. In the total ground state scenario condensation starts due to the increased confinement for lithium. The distribution over the lattices sites varies strongly between the two methods. In the transversal picture for the total μ calculation a lithium BEC is visible. Due to its low relative density, the thermal fraction is invisible in this representation. The sodium peak column density is more than ten times higher than the lithium peak density calculated by method that allocates the lithium density in the optical dipole to lattice sites. The other method results in a doubled lithium peak density. Due to the experimentally observed strong difference between the two discussed typical ^{7}Li settings in the following graph the optical dipole trap scenario (red line) will be applied.

In subsection 3.3.3 the mixture's density distribution in the optical dipole trap is given for typical experimental parameters. We will now discuss these scenarios, this time in case of the standing light wave potential. In Fig. 3.8 the calculated profiles in lattice direction for the three different scenarios are depicted. The left side gives the key parameter values, the center shows the lithium (sodium) profile in lattice direction in red (blue) and the right side shows the transversal density distribution which is obtained by integrating out the lattice direction.
The first row shows ^{6}Li, for which the envelope of the distribution is only slightly changed compared to the case without the lattice potential (see Fig. 3.5). The sodium column density is more than 15 times higher than the lithium one. The transversal picture shows good penetration of the BEC by the lithium cloud. Many lattice sites are occupied, the outer ones without contact to the sodium BEC.
The second row shows ^{7}Li for small atom numbers. It is the same data as shown in Fig. 3.7 and its optical dipole trap density distribution is shown in the upper part of Fig. 3.6. Although the confinement is increased it remains purely thermal. Due to its compression the sodium and lithium column densities assimilate. The value of the immersed fraction η_{im} and the effective density $\bar{n}_{\mathrm{Na}}$ remain the same. In case of increasing lithium atom numbers and condensation they will grow.
In the lower part the density profiles for high ^{7}Li numbers are depicted. The distribution over the lattice sites shows a clear bimodal distribution that originates from the density distribution in the optical dipole trap. The condensate fraction η_{CF}

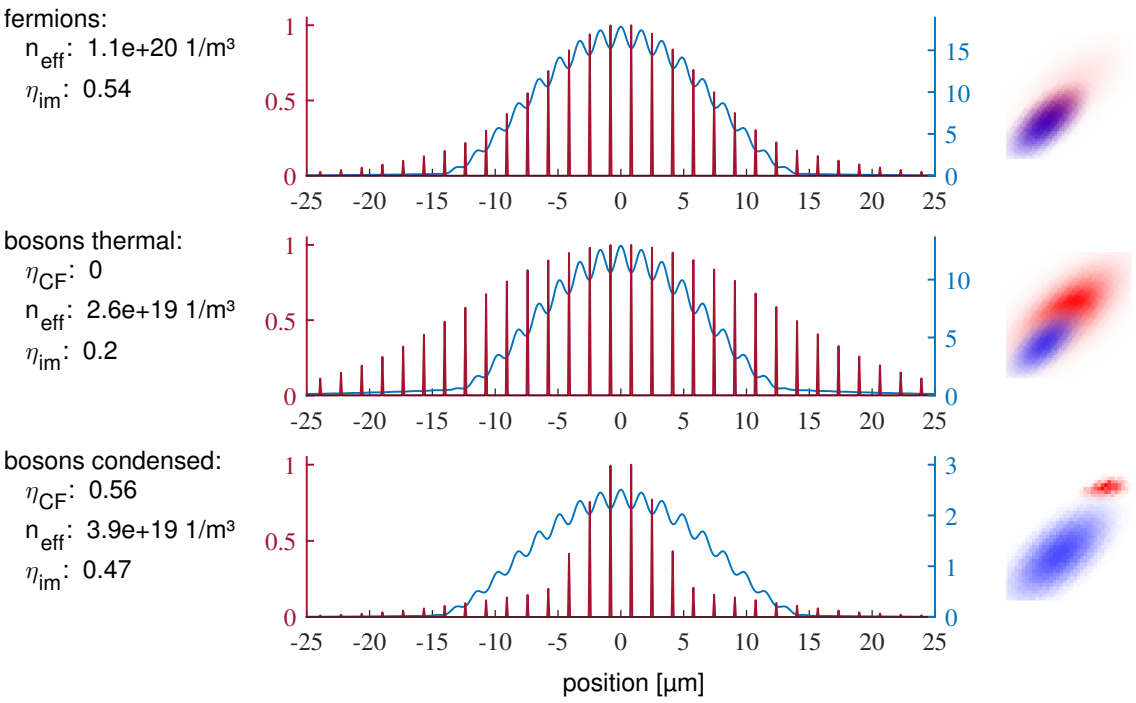

Figure 3.8: Comparison of the density profiles in the three typical scenarios. In all cases the lattice wavelength is 670.5 nm and the lattice frequency for lithium is $\omega = 2\pi \cdot 27.25\,\mathrm{kHz}$. The right panel shows transversal pictures by integration over the lattice direction. Sodium is shown in blue, lithium in red.

increases slightly from 0.53 to 0.56 due to the increased confinement. The values for $\bar{n}_{\mathrm{Na}}$ and η_{im} remain almost unaltered. The maximum of the lithium column density is about half the value of the sodium peak value. Therefore the approximation of no influence on sodium by the lithium density has to be questioned. Still the sodium intra-species scattering length is about three times higher than the interspecies one.

In Fig. 3.9 the relative effect of the wavelength, atom numbers and temperature on the key parameters describing the density distribution for condensed bosonic and fermionic impurities is shown. The upper row depicts the condensed ^{7}Li case, the lower row the ^{6}Li scenario. As we will see in the theory section, ^{7}Li is interesting to us only in case of condensation. Therefore in the next paragraph the thermal case is not discussed.
In the left column the impact of the wavelength on the clouds is addressed. If the lattice is red detuned for lithium, the pancakes are located in sodium BEC density maxima, for blue detuning they are situated in sodium density minima. Our experiments take place at four different wavelengths symmetric to the lithium

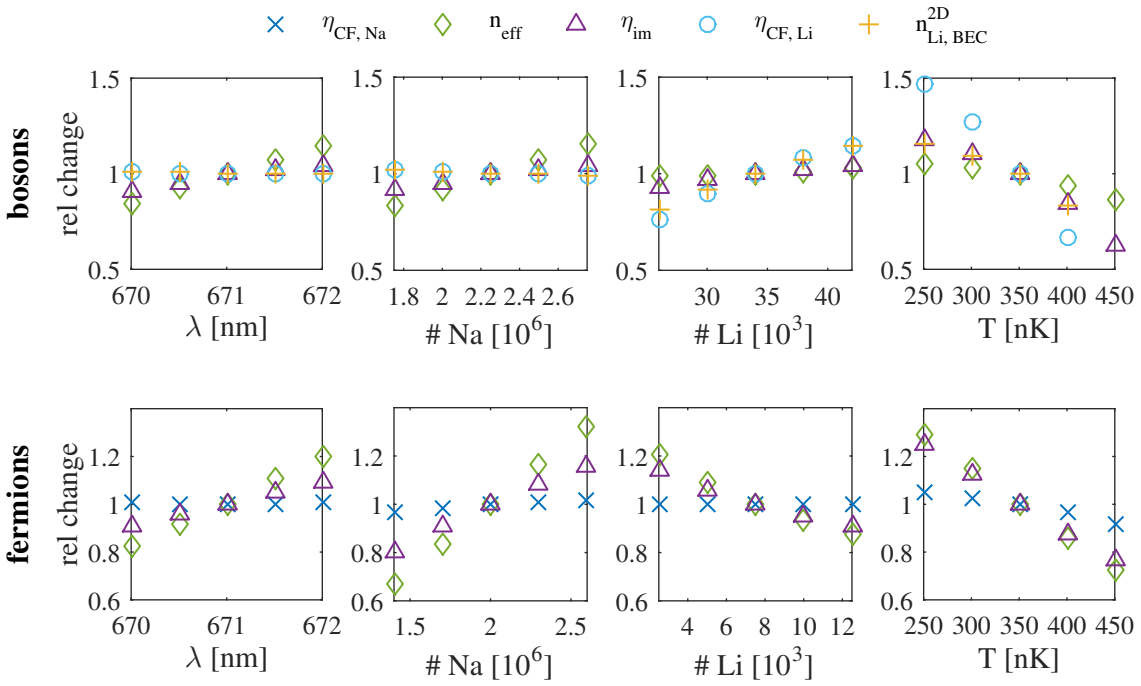

Figure 3.9: The dependence of the overlap characterizing key parameters on the wavelength of the trapping light, the sodium atom number, the lithium atom number and the temperature. The key parameters are the sodium condensate fraction η_{CF}, the effective sodium density $\bar{n}_{\mathrm{Na}}$, the immersed fraction of lithium atoms in the sodium BEC η_{im}, for ^{7}Li BECs the condensate fraction η_{CF} and the 2D BEC density $n^{2\mathrm{D}}_{\mathrm{Li,\,BEC}}$. Shown are the two typical experimental scenarios of interest for phononic effects.

transition and we are interested in a theoretical 5^{th} wavelength, the resonant case for lithium, at which sodium is not affected by the lattice. The reason is that the lithium potential is kept constant, so on resonance the potential impact on sodium is negligible. In order to understand the corresponding behavior a lattice potential of $\omega = 2\pi \cdot 27.25\,\mathrm{kHz}$ is assumed for lithium and the wavelength is scanned, altering the effect for sodium. Red detuning increases lithium immersion η_{im} and effective sodium density $\bar{n}_{\mathrm{Na}}$. The values change up to 20 %. The absolute lithium density distribution is hardly affected, leaving $n^{2\mathrm{D}}_{\mathrm{Li,\,BEC}}$ and the condensed fraction flat. The same is observable for sodium, so the change of the wavelength just displaces the clouds with respect to each other.
All experimental parameters are known with limited precision and to a certain extent target values for atom numbers, temperature and trapping potential can be chosen freely. Therefore the influence of the main parameters on the key values describing the overlap of the two clouds is studied here. Due to the influence of the lattice parameters on the key values, for the data of the following plots a lattice of $\omega = 2\pi \cdot 27.25\,\mathrm{kHz}$

is assumed for lithium but sodium remains unaffected, corresponding to a resonant lattice for lithium. Again the two relevant experimental situations are studied and changes are given relative to the standard value.
In all changes the condensed fraction η_{CF} for sodium is robust, due to the small T/T_{C} values we work at. The sodium distribution does not depend on the impurity species. For clarity the sodium value for η_{CF} it is not plotted in the graphs about the mixtures including ^{7}Li. The lower row shows the fermions. Here we see that higher sodium numbers increase the overlap values. In good approximation $\bar{n}_{\mathrm{Na}}$ is linear in the sodium atom number. Growing temperature decreases the overlap. Temperature is not very critical for fermions, as no sudden transition takes place. Rising lithium numbers cause larger clouds and thereby reduce the key parameters, which are related to the whole clouds, considering the lithium atoms outside the sodium BEC as well.
Bosons are depicted in the upper row. Here a gain in lithium atom number increases the impurity BEC size and density and thereby all overlap values. Especially critically dependent on the lithium atom number is the value for $n^{\mathrm{2D}}_{\mathrm{Li,\,BEC}}$, as it is based on the number of condensed lithium atoms. For bosonic impurities the temperature is more critical than for fermions, as condensation strongly influences the density distribution. On the other hand having this phenomena at hand it is much easier to measure the temperature, see subsection 3.2.3. On a change in temperature of 100 nK the ^{7}Li condensate fraction η_{CF} changes by 50 %.
In the same way as the calculations for Fig. 3.9 error estimations of the theory predictions based on overlap values can be done. The response of infinitesimal changes of the input parameter to the key parameters can be calculated. All input parameter to the simulation have been tested and the above shown prove to be the most significant. This obviously depends as well on the uncertainty to which the experimental parameters are known.

4 Species-Selective Optical Lattice for Lithium

In our setup, we superimpose a periodic optical dipole trap potential, referred to as lattice, onto the optical dipole trap potential retaining the sodium and lithium clouds. It is generated by two interfering laser beams, resulting in good approximation in an array of two-dimensional planes of equal intensity at the location of the atomic cloud. As the frequency of the laser beams creating this lattice is close to resonance for lithium, its strength is much higher for lithium than for sodium. Therefore it is called species-selective or species-specific [80]. The lattice is our main tool to study the impurity-BEC interaction. In this chapter its fundamental characteristics are presented.
First we describe the implementation of the lattice in the experimental setup. Next we summarize the properties of atoms in periodic potentials. Our experiments use the lowest external levels of the lattice. The occupation of the states can be detected using band mapping. By a periodic modulation of the lattice position (shaking), external states can be coupled, resulting in Rabi oscillations. Having the detection and manipulation techniques at hand, we can perform measurements of the energy spacing between the lowest levels by spectroscopy. The achievable precision of the spectroscopic measurements is limited by decoherence due to lithium-sodium collisions and intra-species collisions for ^{7}Li.

4.1 Species-Selective Optical Lattice Setup

Based on the insight we gained on species-selective potentials [48, 52], we implemented a new lattice with slightly altered parameters compared to the former realizations. The lattice is created by two intersecting laser-beams with a waist of about 800 µm. The light is provided by a dye laser, resulting in a small line width and high wavelength tunability. The relative angle of the two intersecting beams ($\approx 23°$) results in a lattice spacing of about 1.65 µm. The lattice is oriented parallel to the horizontal optical dipole trap beam, allowing for band mapping into this beam with high optical density even after long evolution times. Hence relatively low lithium atom numbers

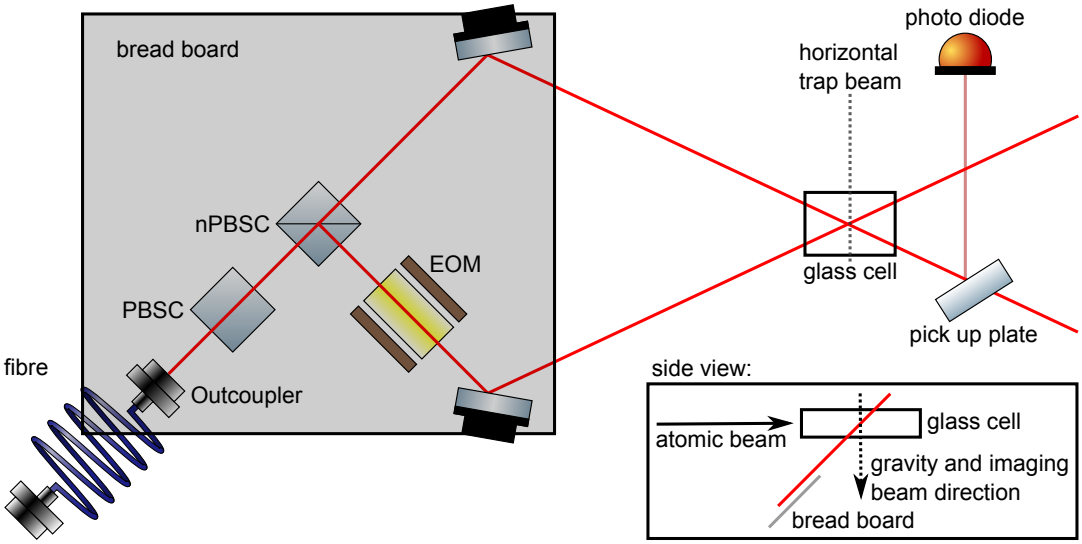

Figure 4.1: The species-selective optical dipole trap setup used as a tool to probe impurity-BEC physics. Gravity trends to the left and into the drawing plane (see side view). All optical elements are mounted on one bread board (gray plane). The laser light is split by a non-polarizing beam splitter cube (nPBSC). The beams interfere at the position of the atoms (inside the glass cell). An electro-optic modulator (EOM) in one of the beam paths allows for a change of the relative phase of the two paths, moving the interference pattern. A fraction of one beam is employed to control the light intensity.

can be used, approaching the impurity physics we aim for. The setup is shown in Fig. 4.1. The fiber collimator delivers a collimated beam, a polarizing beam splitter cube cleans the polarization. It is oriented perpendicular to the drawing plane. A non-polarizing beam splitter cube divides the intensity into two equal parts. The use of a polarization independent element at this position has resulted in an increase of stability in the old setup, as the power stabilization is done on the intensity in one beam, so changes in the power splitting due to polarization fluctuations influence the potential depth at the position of the atoms. In the reflected port of the cube an electro-optic modulator is mounted (EM200T-PM-AR671, Leysop Ltd.). When applying a voltage, it changes the relative phase of the two beams. The electrodes enclose a lithium tantalate crystal which exhibits the Pockels effect when an electric field is applied. The voltage necessary for a phase shift of 2π is about 150 V. Such voltages can be obtained with a high-voltage amplifier, but due to the small amplitudes used for coherent coupling of external states, all experiments presented in chapter 6 are performed with the arbitrary wave function generator directly connected to the electro-optic modulator. The two beams are reflected by two

mirrors, allowing for spatial adjustment onto the position of the atoms. Alignment is done using resonant light and by imaging the beams onto a CCD camera. This way the position of the beams can be compared to the position of the atoms. Behind the glass cell a part of the electro-optic modulator beam is reflected onto a photo diode for power regulation. A calibration yields $44\,\mathrm{mW\,V^{-1}}$ transmitted through the glass cell per beam. The standard working intensity used for our experiments is about 1 V control voltage. All the optomechanical devices are mounted on fixed height posts to a breadboard ($20 \times 25\,\mathrm{cm}$) that is attached via a rotatable large angle bracket to the vertical breadboard on our experimental table. No stability problems e. g. due to vibrations have been observed. The wavelength of the dye laser is measured via a commercial wavemeter and registered. A microcontroller reads out the serial port of the wavemeter, shows the value on several displays within the lab and sends the values to the experiment control PC that saves the values along with all other sequence parameters and the images. The photodiode voltage is recorded as well using an analogue input port of the experiment control system. The value is registered at the end of the lattice loading sequence. As wavelength and intensity are known, the potential depth can be calculated in the data analysis.
The starting condition for all experiments is an as pure as possible ground state occupation, which yields the highest visibility. Therefore the laser light intensity is ramped up adiabatically. Nevertheless some optical dipole trap states are connected to excited states of the lattice [52]. Hence after the lattice ramp-up a waiting period is inserted to let the atoms in the excited state relax to the ground state. The employed lattice loading sequence is the following: within 40 ms the lattice is turned on exponentially with a time constant of 10 ms. Subsequently the atoms are held 20 ms to increase the ground state population. Following this, the experiments are performed.

4.2 Atoms in Periodic Potentials

The periodic potential we apply originates from the interference of two laser beams (wavelength λ, angle α between the beams) and as a result follows a sinusoidal oscillation, see Eq. (3.42). The lattice spacing d_{lat} is related to the lattice vector $\vec{k}_{\mathrm{lat}}$ by:

$$d_{\mathrm{lat}} = \frac{\lambda}{2\sin(\alpha/2)} = \frac{\pi}{|\vec{k}_{\mathrm{lat}}|}, \tag{4.1}$$

and is 1.65 µm for our lattice. Often the lattice potential depth V_0 is indicated in units of the lattice recoil energy: $E_{\mathrm{rec}} = \hbar^2 k_{\mathrm{lat}}^2/(2m)$.
This periodic arrangement is similar to the one of electrons in solid state materials.

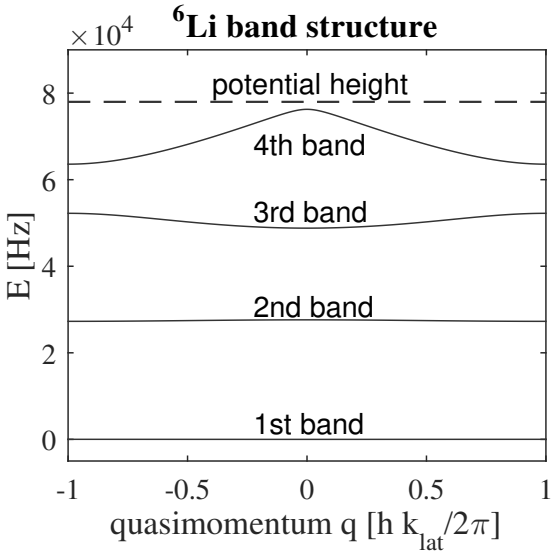

^{6}Li at lattice depth 25.4 E_{rec}:

gap from 1st to 2nd Bloch band 27.3 kHz
gap from 2nd to 3rd Bloch band 21.2 kHz
bandwidth of 1st Bloch band 12 Hz
bandwidth of 2nd Bloch band 347 Hz
bandwidth of 3rd Bloch band 3.4 kHz

^{7}Li at lattice depth 33 E_{rec}:

gap from 1st to 2nd Bloch band 27.2 kHz
gap from 2nd to 3rd Bloch band 23 kHz
bandwidth of 1st Bloch band 3.1 Hz
bandwidth of 2nd Bloch band 108 Hz
bandwidth of 3rd Bloch band 1.4 kHz

Figure 4.2: The band structure for ^{6}Li at the typical experimental lattice depth. Four bands fit into the lattice potential depth. The lower ones exhibit almost no curvature, similar to a harmonic oscillator. The minimum of the lowest band is set to zero. In the right panel characteristic values for gaps and widths are listed for both lithium isotopes.

The corresponding Hamiltonian can be solved assuming an infinite, homogeneous and non-interacting system. The periodicity sets conditions to the wave function. Bloch waves, which are the product of a plain wave and a lattice periodic function, are a solution to this problem [81]. It turns out that the energy spectrum is gapped. The allowed energy ranges are called bands. The calculation is well described in [52]. In Fig. 4.2 the band structure for ^{6}Li at a typical experimental lattice height is displayed, as calculated in a numerical solution of the problem. The lower states are flat, building a conceptual bridge from the deep periodic potential to the harmonic oscillator. In this regime the gap is $\hbar\omega_0 \propto \sqrt{V_0/m}/d$. Although the potential is in good approximation harmonic for the lowest two states with respect to the bandwidth, only 4 bands fit into the lattice potential. The tunneling rate between neighboring lattice sites is 4 times less than the bandwidth for the first Bloch band.
Taking Eq. (3.1) ($V_0 \propto I/\Delta_\lambda$) and the relation $\omega_0 \propto \sqrt{V_0/m}$ into account, we realize that the expression $\sqrt{I/(\Delta_\lambda m\omega_0^2)}$ should be constant. In order to test if our experiments are well controlled and the lattice intensity controlling photo-diode is linear we calculate this ratio for our experimental data. The corresponding results are displayed in Fig. 4.3. The precise measurement of ω_0 is described in subsection 4.4.2. For a better representation the numbers are divided by their mean value. A slight difference between ^{6}Li and ^{7}Li is visible, but no systematic deviations from the expectation are perceivable.

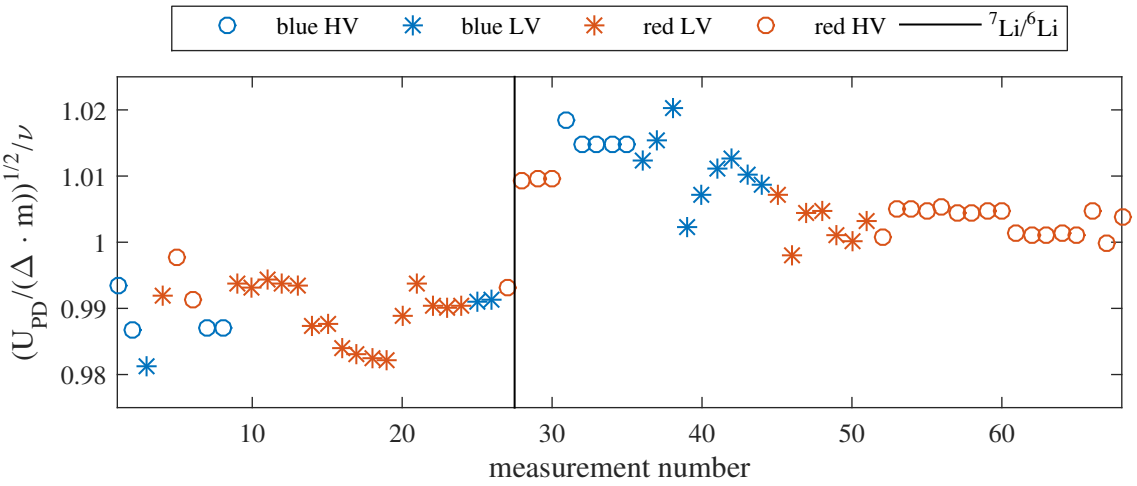

Figure 4.3: Test of the scaling of the lithium potential with the lattice light intensity. For all Ramsey scans the ratio $\sqrt{U_{PD}/\Delta_\lambda m_{Li}}/\nu$ is calculated. The results are divided by their mean value. The lithium isotope changes after scan 27. HV values denote scans with 1.4 V control voltage, LV with 0.7 V respectively. The changes over the course of the measurements are smaller than 2 %.

In our realization of a species specific potential we encounter the challenge that high light intensities influences sodium significantly, so the potential cannot be regarded species selective. For small powers we have to use a small detuning, as we need a sufficient potential depth to suppress tunneling. A small detuning causes high photon scattering and thereby reduces the lifetime of the lithium sample in the lattice. Thus, the species specific lattice as we employ it is a trade-off between these constraints.

4.3 Brillouin Zone Mapping

For a deep potential, the dispersion relation resembles that of a harmonic oscillator. For a vanishing potential it devolves into the dispersion relation of a free particle, a parabola. This can be seen best when the reduced scheme is unfolded, see Fig. 4.4 left panel. It allows for a mapping of the quasimomentum onto the real momentum of the atom when the lattice potential depth is slowly reduced [82, 83]. In order to obtain a high optical density, the horizontal optical dipole trap beam is left on during the expansion. The exponential ramping down of the lattice intensity takes 3 ms with a time constant $\tau = 0.75$ ms. The vertical dipole trap beam is switched off at the beginning of the ramp-down sequence. 10 ms after the start of this sequence an absorption image is taken.

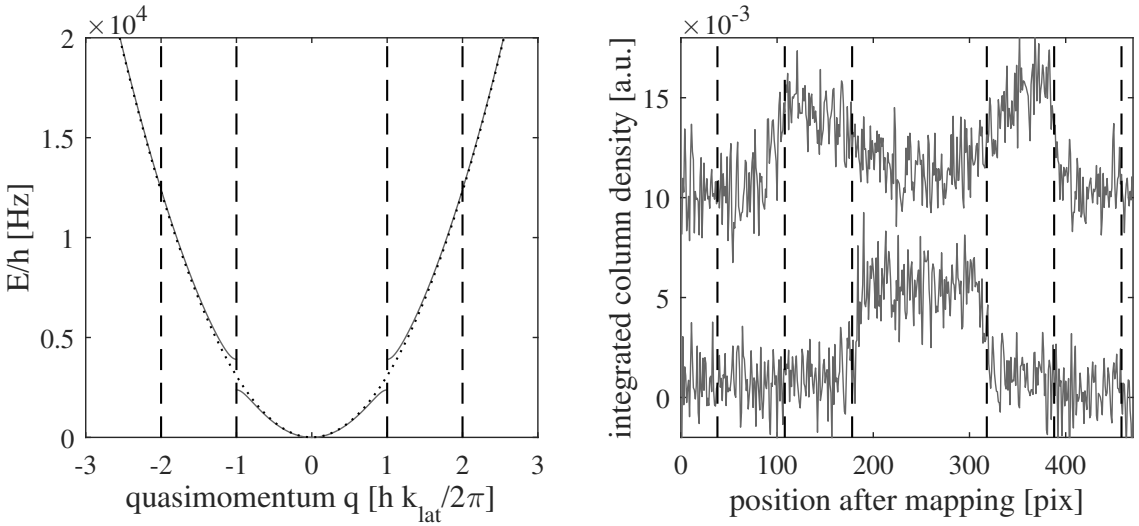

Figure 4.4: For a vanishing potential depth V_0, the dispersion relation approaches the parabola of a free particle (left panel). This can be used for state detection: the potential is adiabatically turned off and the atoms expand along the optical dipole trap beam. Two typical experimental profiles showing low (bottom) and high excitation probabilities (top) are shown in the right panel.

The right panel displays two typical experimental profiles obtained by integrating absorption images perpendicular to the lattice direction. They show low and high occupation of the excited state for a scan with 8000 ^{6}Li atoms. These profiles reveal some detection challenges: due to finite sample size and possibly out of focus imaging the slope of the edges is finite and atoms in the second and third band cannot be unambiguously distinguished. This false assignment reduces the amplitude of the Ramsey fringes and complicates the quantitative comparison of amplitudes to theory. Therefore in the image analysis only the central 50 % of the zones have been considered, which mitigates the erroneous attribution. The other feature is that, although the atoms have been trapped within one beam at the moment of the absorption image and two directions have been integrated out, the profiles are noisy. Still we can derive reliable information from samples with a few thousand atoms. This is a great progress compared to former experiments, where $2 \cdot 10^5$ ^{6}Li atoms have been deployed in order to get a trustworthy signal.
If the experiments are performed with the sodium BEC present, the condensate is removed by in-situ imaging before the mapping of the lithium cloud, as this allows for a better comparison of the procedures and values. Therefore sodium images are in-situ and underestimate the actual atom number because of the large atomic density.
Due to the deep potential, the lattice sites can be assumed to be independent.

Several lattice sites are occupied, resulting in multiple independent realizations of the experiment. Due to the detection method, the measured band population is an average over all sites.

4.4 Coupling of External States

The deeper the periodic potential is, the stronger tunneling is suppressed and the better the lattice is approximated by independent harmonic oscillators. Our goal is the experimental realization of a two level system, but if the potential is close to harmonic, the coupling to the 3rd state becomes resonant as well and the population of the 3rd state rises. Therefore the optimized lattice depth is a compromise between tunneling to adjacent lattice sites and excitation into higher states. Further the splitting between the lowest states has to be large enough to prepare the ground state. If the chemical potential of the sodium BEC is higher than the energy of the excited lattice state, no efficient cooling of lithium to the ground state takes place. A pure as possible ground state preparation yields a high fringe contrast which is necessary for precise spectroscopy.

4.4.1 Rabi Oscillations

The sinusoidal modulation of the lattice position on a small spatial scale ($\approx 0.01 d_{\mathrm{lat}}$) couples different trap levels at individual lattice sites. This process is analogous to the coupling of electronic states in an atom by an oscillating electric field. This dipole type mechanism couples states of different parity. The Rabi frequency is proportional to the amplitude of the oscillation. For high amplitudes atoms are excited into higher bands than the second due to off-resonant coupling. For further reading see [52]. In Fig. 4.5 an exemplary Rabi cycle is depicted. The relative occupation of first and second excited state is shown. It is difficult to specify the contribution of erroneous assignment to the 3rd state. Numerical simulations of a three level system as quantified in the right panel of Fig. 4.4 with additional Rabi coupling show a population oscillation between ground and excited state with non-zero amplitude for the third band. Coupling to the 3rd state is undeniable but hard to quantify, just as the ground state preparation. Here assignment of atoms in the ground state to the first excited state complicate quantitative statements. Our measurements are based on Ramsey spectroscopy, hence the inaccurate mapping reduces the visibility but does not change the position of the fringe, which contains the frequency information. The employed frequency for the Ramsey sequence is set to fit the gap of ground to

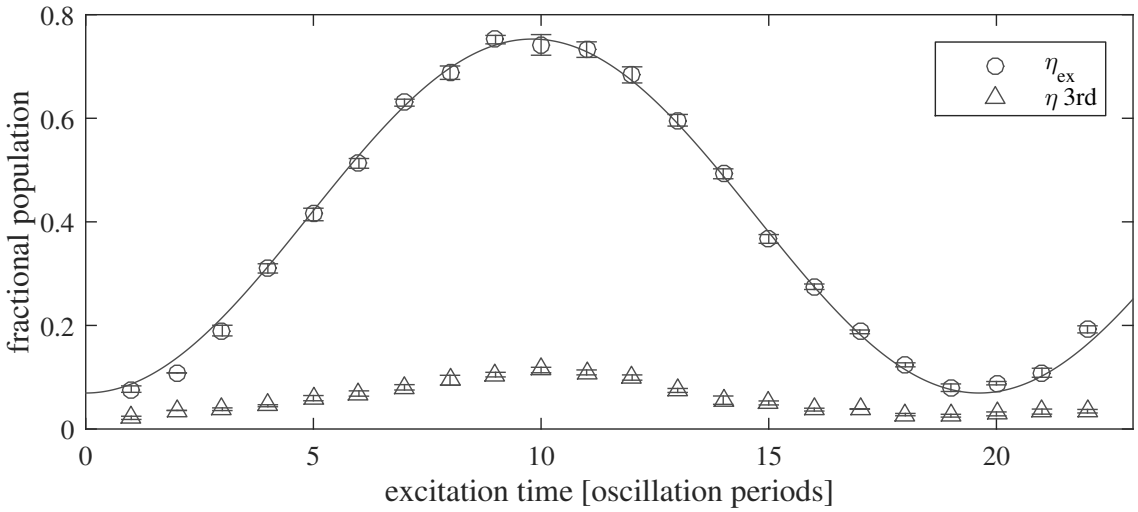

Figure 4.5: Shaking the lattice couples the motional states, resulting in Rabi oscillations as reflected in the relative populations of the different external states. The occupation of the first excited state (circles) reaches about 75 %, the second excited state (triangles) ranges to $\sim 11\,\%$ at the maximum. One Rabi cycle lasts ~ 20 oscillation periods.

first excited state.
Besides the amplitude of the Rabi cycle, its frequency is notable as well. Within 20 oscillation periods of the driving the population has carried out one oscillation. This yields a Rabi frequency of 1.35 kHz or 5 % of the fundamental frequency.

4.4.2 Ramsey Spectroscopy

For a rough measurement of the gap between ground and first excited state, we perform spectroscopy, i. e. Rabi oscillations of low amplitude for a fixed duration at different frequencies. The employed amplitude and duration should be chosen such that the highest relative population of the excited state is well below one. After this rough scan we perform Ramsey spectroscopy to obtain a higher sensitivity [48, 49]. The basic idea is to apply a first pulse that creates a superposition of ground and excited state. For the most part we use a symmetric superposition, which is created by shaking for 5 oscillation periods. Next the system can evolve freely. After some time another coupling pulse is applied (duration 5 oscillation periods, with the same phase). Note that the duration of the coupling pulses also contributes to the phase evolution and thus has to be accounted for in the interpretation of the results. The effect of this pulse depends on the relative phase of the superposition state to the pulse. We observed experimentally and calculated numerically with

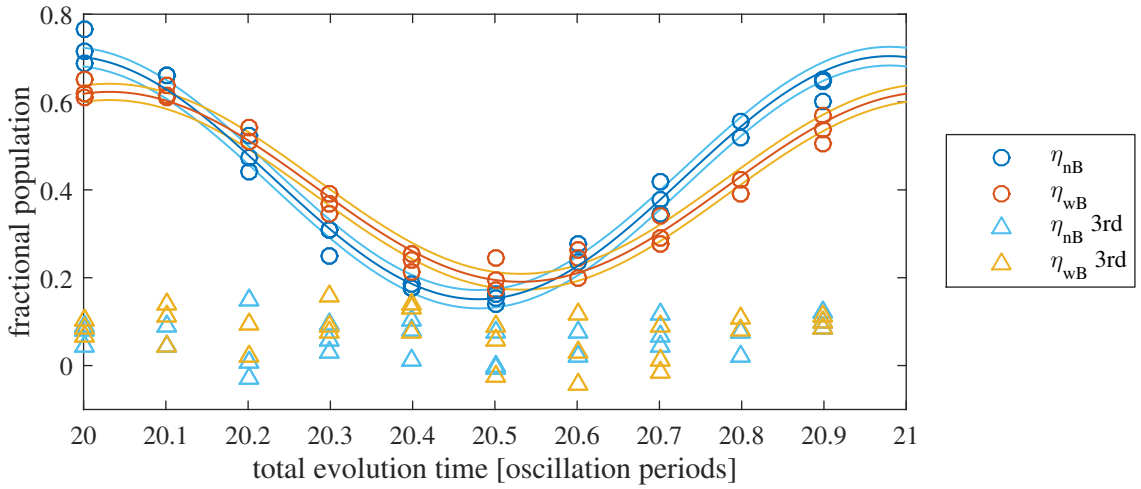

Figure 4.6: Ramsey fringes for a cloud of 8000 ^{6}Li atoms. The excited state population (circles) exhibits a sinusoidal fringe. They are fitted and their 68 % confidence interval is indicated by lines as well. The curve for experiments with background BEC (red) shows a smaller amplitude and a different phase than the scans without BEC (blue). The second excited state is displayed by triangles.

a split-step Fourier simulation that a sudden shift of the lattice causes excitation into higher states. To avoid sudden changes of the lattice position, the second pulse sequence has the identical shape as the first, but it is displaced within one oscillation period, such that the effective phase is changed. In order to sample the interference pattern, 10 different effective phases of the second pulse are employed subsequently. As a result we obtain fringes in the population of the excited state, see Fig. 4.6, whose phase depends on the evolution time and the mismatch between coupling frequency and the energy gap. This way a frequency difference manifests itself as a measurable shift of fringes in the state population. In this case (Fig. 4.6) the background causes a shift of the fringe to the right, which corresponds to a reduction of the energy gap. The next chapter explains background induced effects and in chapter 6 the result of many of such scans are presented. The values displayed there are obtained by an automatic evaluation routine that discards shots with abnormal atom number or lattice potential and performs the fitting. Most of the scans consist of three subsequent repetitions, each of them is constituted by 10 different effective phases. They are measured alternately with and without background BEC to be robust against drifts of the potential. As such drifts actually occur and slowly shift the fringe pattern, every single repetition is fitted by two sine functions (one for measurements with, one for measurements without sodium). We are interested in the background-induced effect on the level splitting. Thus the value of interest is the phase difference between the two sine fringes. For each scan, the confidence weighted

mean of the repetitions is calculated. Expressing the evolution time in oscillation periods and the fringe shift by the relative phase ϕ turns out to be very handy for accessing the relative frequency shifts. If we measure a phase $\phi = 0.1 \cdot 2\pi$ after 20 cycles of evolution time, we can easily calculate the corresponding relative frequency shift:

$$\delta = \frac{\Delta\omega}{\omega_0} = \frac{(\omega - \omega_0)t}{\omega_0 t} = \frac{\phi}{\omega_0 t} = \frac{\phi}{2\pi\nu t} = \frac{\phi}{2\pi}\frac{\nu}{\#\text{Cycles} \cdot \nu} = \frac{\phi}{2\pi \cdot \#\text{Cycles}}. \tag{4.2}$$

In this example $\delta = 0.005$. It turns out that the frequency and absolute time drop out, which is the reason why for most measurements the number of cycles is specified, not the absolute time.

4.5 Decoherence

Lithium atoms interact with the sodium BEC via collisions. If they are in the excited state or in a superposition of ground and excited state, this dissipative process reduces the population of the excited state and the fringe amplitude of the Ramsey sequence. Furthermore dephasing due to an inhomogeneous frequency distribution over the sample can reduce the amplitude of the Ramsey fringes as well. Our previous project with this sodium-lithium experiment studied these phenomena extensively [48, 52]. Therefore only a short summary is given here.
The decay rate of the excited state due to interaction with sodium is called Γ_1, referring to nuclear magnetic resonance. The rate describing the reduction of the superposition amplitude due to collisions with sodium is called Γ_2. The first process is called population decay, the latter decoherence. For a pure two-level system coupled to a continuum, the relation between the two quantities is given by $\Gamma_2 = \Gamma_1/2$. This situation can be addressed by Fermi's golden rule [1, 2].
Dephasing can occur when the different lattice sites exhibit different potential depths e. g. due to the Gaussian lattice beam profile. By a refocusing spin echo pulse, this effect can be compensated for, a technique widely employed in nuclear magnetic resonance [84]. In this thesis no spin echo sequences have been employed as they require longer total evolution times. In fact, besides the amplitude reduction, the reason why we are interested in decoherence is that it renders the measured frequency shift of an inhomogeneous cloud time dependent, see section 5.5.

4.5.1 Population decay due to Na-Li Scattering

As mentioned before, a spin echo technique is necessary to determine the decoherence rate we are interested in. For simplicity we derive the decoherence rate from the population decay rate, which is easier to obtain experimentally. Previous measurements have shown that in our system the ratio is close to the ideal value $\Gamma_2 = \Gamma_1/2$. The population decay rate is, besides some constants, only dependent on the overlap of the clouds. This can be illustrated by a simple collision model. The scattering rate of the lithium atom depends on the scattering cross section with sodium, its velocity and the sodium density $\Gamma = n_{\mathrm{Na}}\sigma\bar{v}$. For an estimate of the velocity we can derive the maximum oscillation speed of a superposition of the two lowest harmonic oscillator states $v_{\max} = \sqrt{\frac{\hbar\omega_0}{2m_{\mathrm{Li}}}}$. The mean velocity in average over time is $\bar{v} = v_{\max}/\sqrt{2}$. The resulting collision rate is $\Gamma = n_{\mathrm{Na}} 4\pi a_{\mathrm{IB}}^2 \sqrt{\frac{\hbar\omega_0}{4m_{\mathrm{Li}}}}$, specified in Eq. (5.61). The sodium density can be assessed by the effective density $\bar{n}_{\mathrm{Na}} = 1/N_{\mathrm{Li}} \int n_{\mathrm{Na}} n_{\mathrm{Li}} \mathrm{d}V$, which is the lithium density weighted mean of the sodium density, see Eq. (3.38). This approach has been presented in our previous publication [48].

In Fig. 4.7 the time evolution of the first excited state of the lattice (after a population inverting pulse) is shown for thermal ^{7}Li and ^{6}Li. It strongly depends on the presence of the sodium BEC. Without it, the excited state is long lived. In the presence of the condensate, however, the lithium atoms collide with the background and decay to the ground state. Due to the stronger interspecies interaction this process is faster for ^{6}Li. The exponential fits have an offset of 0.2. Still, in the long-time limit all lithium atoms that have not been scattered out of the trap end up in the ground state, contradicting the fit for short times. Especially in the case of fermionic lithium, a further, much slower decay is visible. The complete details of the decay process cannot be completely captured by a single exponential function. This is evident, as some of the populated lattice sites are located outside of the sodium BEC and thus have a much lower collision rate, corresponding to the thermal sodium density, which is much lower than the BEC density.
Nevertheless, for a simple theoretical description, the situation is well approximated if we deploy the simple collision model described above and capture the atomic density distributions by the effective sodium density. It yields a collision rate for the decoherence process which can be translated into decay time constants. For the plotted ^{7}Li curve we obtain $\sim 31\,\mathrm{ms}$, close to the fitted result of $\sim 25\,\mathrm{ms}$. The fermionic situation shows less agreement. The calculation results in $\sim 1.2\,\mathrm{ms}$, a factor of three faster than the fitted value. The search for the reason for this discrepancy is an involved discussion. Several factors contain possible defects: the simple collision model, the density distribution calculation, the experimental procedure and neglecting

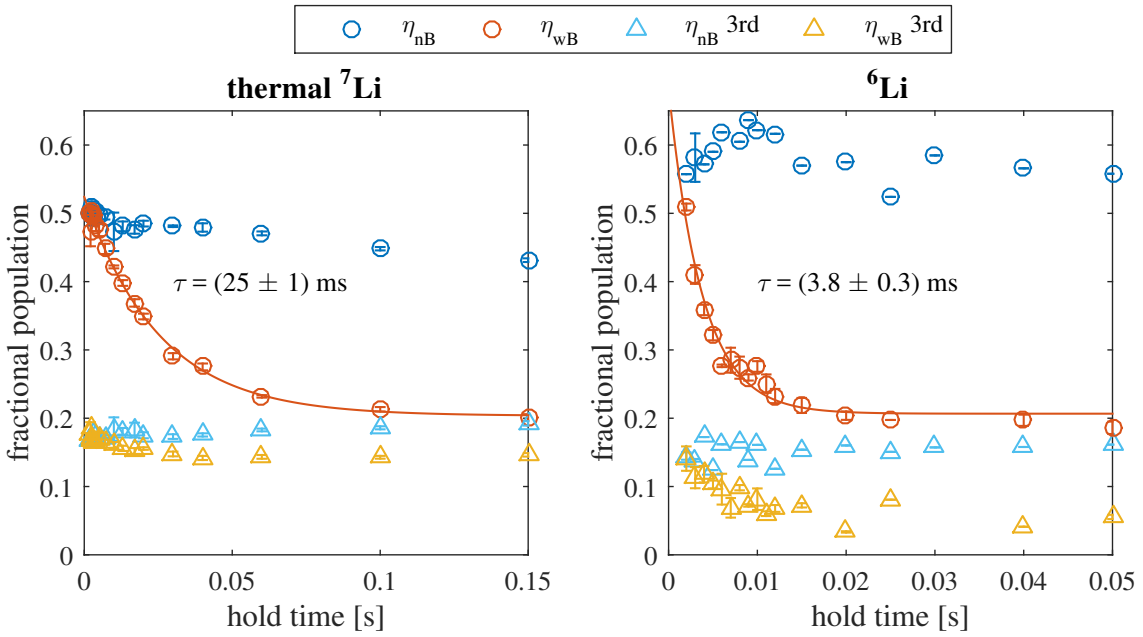

Figure 4.7: Exemplary population decay curves comparing thermal ^{7}Li (left panel) to ^{6}Li (right panel). Via Brillouin zone mapping the population of the states in dependence of time and background is measured after an excitation pulse. The lattice wavelength for these measurements is 672 nm, the sodium atom number about $1.8 \cdot 10^6$, the lithium atom number on the left is $14 \cdot 10^3$ and $8 \cdot 10^3$ on the right. Without BEC the excited state (blue circles) is long lived. If the background BEC is present, the population of the excited state (red circles) decays, the population of the ground state (not plotted) increases. The decay rate is determined by an exponential fit (red line). It is one order of magnitude faster for ^{6}Li than for ^{7}Li due to stronger interspecies interaction.

the deviation from a single exponential process. In conclusion the collision model allows a decent and straightforward description of the sodium density-dependent decoherence.

4.5.2 Population decay for condensed ^{7}Li

The situation is more complex for condensed ^{7}Li. In this case, high lithium densities occur and for bosons intra-species scattering is allowed. Furthermore the transfer of an atom pair from the excited state into ground and second excited state is energetically favorable. In Fig. 4.8 the experimental observation of this feature is

presented. After excitation the population of the excited state decreases even without sodium BEC (blue circles). Correspondingly the relative (right panel) and absolute (left panel) population of the third level rises. The process stops or decelerates at a certain population of the excited state, probably due to its decreased density. The decay of atoms from the second state into ground and third level has been described in similar systems [85].

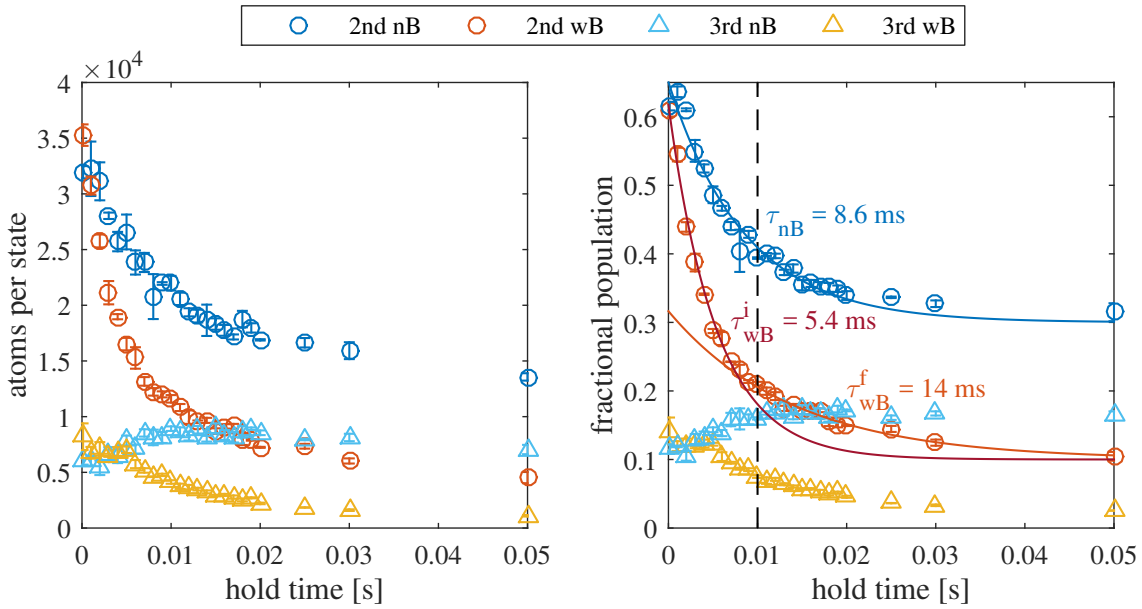

Figure 4.8: Population decay curves for condensed ^{7}Li. The lattice wavelength is 672 nm, the sodium atom number about $2.2{\cdot}10^6$, the lithium atom number is $5 \cdot 10^4$. Bosonic lithium atoms can collide and thereby pairs of atoms in the first excited state (circles) can be transferred into the second excited (triangles) and the ground state. This process does not depend on the sodium BEC and is faster than the population decay due to scattering with sodium atoms. After roughly 10 ms it slows down (dashed vertical line) probably due to the reduced lithium density. The immersed decay curve is bimodal and at the long time limit dominated by the interaction with the sodium cloud.

In case of a sodium background the decrease of the excited state population is further increased. These interleaving processes are hard to distinguish. At approximately 10 ms no further increase of the third state population is observed in case of a pure lithium system and at about this time the immersed system exhibits a kink of the excited state fraction. The decay prior and after this specific moment in time are fitted separately, yielding the decay rates $\tau^{\mathrm{i}}_{\mathrm{wB}}$ for the initial and $\tau^{\mathrm{i}}_{\mathrm{wB}}$ for the final process. The final evolution is dominated by interaction with sodium, the initial one

by the total of intra- and interspecies interaction. Therefore the sum of these rates equals the initial immersed rate:

$$\frac{1}{\tau_{\mathrm{wB}}^{\mathrm{i}}} = \frac{1}{\tau_{\mathrm{wB}}^{\mathrm{f}}} + \frac{1}{\tau_{\mathrm{nB}}} = \frac{1}{14\,\mathrm{ms}} + \frac{1}{8.6\,\mathrm{ms}} = \frac{1}{5.3\,\mathrm{ms}}. \tag{4.3}$$

This is of course only a rough and empirical description of this feature. Nevertheless we can compare the time constant of the derived background-induced decay (14 ms) to the value we obtain by the collision model and the effective density: $\sim 27\,\mathrm{ms}$. It either underestimates the overlap or one or more of the other uncertainties cause this disagreement.
The simple collision model enables us to calculate the decoherence rate as a function of the sodium density. The spread of experimentally relevant sodium densities within one cloud is larger than the mismatch of the observation to the prediction. Therefore it is an essential tool for the time dependent description of the signal of a whole atomic cloud, see section 5.5. Further within the longest experimentally employed evolution time (1.1 ms) only for ^{6}Li decoherence is significant.
The faster intra-species decay process for condensed ^{7}Li does not change the frequency value of the Ramsey spectroscopy. First of all we compare the system with and without sodium background, while the intra-species process takes place in both scenarios. Secondly it only reduces the amplitude of the Ramsey fringe but does not alter its phase. This is true if the affected lithium atoms are only weakly dependent on the sodium density. If the sodium cloud causes strong deformation of the Lithium BEC and the lithium atoms experiencing e. g. especially high sodium densities are stronger affected by Li-Li collisions, the self-energy is underestimated. Furthermore the process is significant only in case of high excitation probabilities during the free evolution. In the respective scans in Fig. 6.8 a reduced amplitude is observable.

5 Theory of an Impurity in a BEC

In the following chapter we will discuss the theoretical description of an impurity atom in a BEC. As the full many body Hamiltonian is intractable to solve, we will study two different approximations for determining the energy shifts: the coupled Gross-Pitaevskii equations (see subsection 3.1.2 for the single species case) and the Fröhlich Hamiltonian. Further, we will consider the density modulation of the BEC by the standing light wave as a second possible source for a background dependent impurity trap level shift. In the last part we will analyze the signal constitution in the experiment, where many impurity atoms at different BEC densities are summed up to one signal.

5.1 Coupled Gross-Pitaevskii equations

We will study the impurity-BEC interaction employing a mean field approach. It leads to the well known Gross-Pitaevskii equation [72, 73], where operators are replaced by c-numbers. The term *mean field* describes that the boson-boson and the boson-impurity interaction are not described microscopically, but by an averaged potential of the respective fields. In general we consider either fermionic or bosonic impurities. In this section the atom number for the fermionic case is set to one and for the bosonic one the particle number ranges from one to N. The impurities are represented by one wave function Φ and are distinguishable from the bosonic background atoms. A wave function for many bosonic atoms depicts a BEC. The background BEC wave function is denoted by Ψ. The coupled time-independent Gross-Pitaevskii equations read:

$$\mu_{\mathrm{B}}\Psi = \left(-\frac{\hbar^2\nabla^2}{2m_{\mathrm{B}}} + g_{\mathrm{BB}}\Psi^*\Psi + g_{\mathrm{IB}}\Phi^*\Phi\right)\Psi, \tag{5.1}$$

$$\mu_{\mathrm{I}}\Phi = \left(-\frac{\hbar^2\nabla^2}{2m_{\mathrm{I}}} + V + g_{\mathrm{IB}}\Psi^*\Psi\right)\Phi. \tag{5.2}$$

See subsection 3.1.1 for a definition of g. The impurity intra-species interaction g_{II} is neglected as we either deal with one impurity atom or with a weakly self-interacting ^{7}Li BEC. For simplification the sodium BEC has no confining potential,

leaving it flat. The eigenvalues of the wave functions are the chemical potentials μ_B (μ_I), respectively. In Eq. (5.1) the first term corresponds to the kinetic energy, the second term to the intra-species interaction of the bosonic bath and the third one to interspecies interaction. In Eq. (5.2) the first term is the kinetic energy, the second term is the potential energy and the third term is the interspecies interaction. As impurity-impurity interaction is neglected, it is the Schrödinger equation of the impurity where to the external potential V the potential of the BEC is added. In this special case the chemical potential is equal to the energy per particle. Only one impurity wave function is considered. This is appropriate if the number of impurities is low. The eigenvalues of the fields can be calculated by multiplication with the complex conjugate and integration over space. For a further evaluation we can utilize the normalization of the impurity wave function $\int \mathrm{d}V|\Phi|^2 = N_\mathrm{I}$. Integration yields:

$$\begin{aligned}\int \mathrm{d}^3x\, \mu_\mathrm{B}|\Psi|^2 &= \int \mathrm{d}^3x \Psi^* \left(-\frac{\hbar^2}{2m_\mathrm{B}}\nabla^2 + g_\mathrm{BB}|\Psi|^2 + g_\mathrm{IB}|\Phi|^2\right)\Psi, \\ \int \mathrm{d}^3x\, \mu_\mathrm{I}|\Phi|^2 &= \int \mathrm{d}^3x \Phi^* \left(-\frac{\hbar^2}{2m_\mathrm{I}}\nabla^2 + V + g_\mathrm{IB}|\Psi|^2\right)\Phi. \end{aligned} \tag{5.3}$$

We will use a simple model to understand the basic principles of these equations.

5.1.1 Analytic Model

We can solve the ansatz of a homogeneous BEC and a trapped impurity initiated above if we make use of further approximations. The impurity density $n_\mathrm{I} = |\Phi|^2$ creates a potential for the BEC of strength: $V_\mathrm{B} = g_\mathrm{IB} n_\mathrm{I}$. In Thomas-Fermi approximation, the kinetic energy of the BEC is small compared to its self-interaction and is neglected. In this case the BEC density fills up this potential $n_\mathrm{B} = (\mu_\mathrm{B} - V_\mathrm{B})/g_\mathrm{BB}$, adapting to the shape of the potential, in our case the impurity density, see Eq. (3.23). As the potential of the impurity is not deep enough to trap all BEC atoms, the density of the bath is modulated with the shape of the impurity density. For an illustration see Fig. 5.2. The resulting BEC density reads:

$$|\Psi|^2 = n_\mathrm{B} = n_0 - \frac{g_\mathrm{IB}}{g_\mathrm{BB}} n_\mathrm{I}. \tag{5.4}$$

As the constant part (n_0) gives just an offset to the energy we can ignore it. We thus have three contributions to the total energy of the system, the energy of the background BEC E_B, the energy of the impurity E_I and the cross interaction energy E_IB. Note that the kinetic energy of the BEC is neglected due to the Thomas-Fermi

approximation.

$$
\begin{aligned}
E_{\mathrm{B}} &= \int \mathrm{d}V \Psi^* \left(g_{\mathrm{BB}} |\Psi|^2 \right) \Psi = \int \mathrm{d}V g_{\mathrm{BB}} n_{\mathrm{B}}^2 \\
&= \int \mathrm{d}V g_{\mathrm{BB}} \left(n_0^2 - 2 \frac{g_{\mathrm{IB}}}{g_{\mathrm{BB}}} n_0 n_{\mathrm{I}} + \frac{g_{\mathrm{IB}}^2}{g_{\mathrm{BB}}^2} n_{\mathrm{I}}^2 \right) \\
&= E_{\mathrm{B}}^0 - 2 g_{\mathrm{IB}} n_0 \int \mathrm{d}V |\Phi|^2 + \frac{g_{\mathrm{IB}}^2}{g_{\mathrm{BB}}} \int \mathrm{d}V |\Phi|^4 \\
&= E_{\mathrm{B}}^0 - 2 g_{\mathrm{IB}} n_0 N_{\mathrm{I}} + \frac{g_{\mathrm{IB}}^2}{g_{\mathrm{BB}}} \int \mathrm{d}V |\Phi|^4, \qquad (5.5) \\
E_{\mathrm{I}} &= \int \mathrm{d}V \Phi^* \left(-\frac{\hbar^2}{2 m_{\mathrm{I}}} \nabla^2 + V_{\mathrm{I}} \right) \Phi = -\frac{\hbar^2}{2 m_{\mathrm{I}}} \int \mathrm{d}V \Phi^* \nabla^2 \Phi + \int \mathrm{d}V V_{\mathrm{I}} |\Phi|^2, \qquad (5.6) \\
E_{\mathrm{IB}} &= \int \mathrm{d}V g_{\mathrm{IB}} |\Phi|^2 |\Psi|^2 = \int \mathrm{d}V g_{\mathrm{IB}} n_{\mathrm{I}} (n_0 - \frac{g_{\mathrm{IB}}}{g_{\mathrm{BB}}} n_{\mathrm{I}}) = E_{\mathrm{IB}}^0 - \frac{g_{\mathrm{IB}}^2}{g_{\mathrm{BB}}} \int \mathrm{d}V |\Phi|^4. \qquad (5.7)
\end{aligned}
$$

By the use of Eq. (5.4) we have effectively substituted Ψ by Φ and all energy terms only depend on Φ. The total energy can be calculated by $E_{\mathrm{tot}} = E_{\mathrm{B}} + E_{\mathrm{I}} + E_{\mathrm{IB}}$. It is interesting to note that within this model E_{B} and E_{IB} cancel out up to some constant terms. For example, attractive interaction causes a density increase of the BEC in the shape of the impurity density, increasing the interaction of the BEC with itself and increasing the cross interaction in absolute value but with negative sign. As in this approximation, only kinetic and potential energy of the impurity are left, the solution of the coupled system reduces to the solution of an impurity in potential V_{I}. The potential of the impurity can be approximated to be cylindrical, as the transverse extension is a parameter in our model. In harmonic approximation:

$$
V_{\mathrm{I}} = \frac{m_{\mathrm{I}} \omega_x^2}{2} x^2 + \frac{m_{\mathrm{I}} \omega_\perp^2}{2} (y^2 + z^2). \qquad (5.8)
$$

For the impurity wave function we assume a Gaussian function, characterized by the harmonic oscillator lengths along (a_x) and perpendicular ($a_\perp$) to the lattice. The wave function is normalized to N_{I}. This scenario corresponds to one fermion, one boson or a condensed impurity of N_{I} atoms. The harmonic oscillator wave functions are the solution within our assumptions, neglecting e. g. BEC density modulation by neighboring impurities. As we want to compare the impurity energy in ground and excited state, the two corresponding harmonic oscillator wave functions Φ_0 and

Φ_1 for N_I particles are:

$$a_x = \sqrt{\frac{\hbar}{m\omega_x}}; \quad a_\perp = \sqrt{\frac{\hbar}{m\omega_\perp}}, \tag{5.9}$$

$$\Phi_0 = \sqrt{N_\mathrm{I}}\frac{1}{a_\perp\sqrt{a_x}\pi^{3/4}}e^{-\frac{y^2+z^2}{2a_\perp^2}-\frac{x^2}{2a_x^2}}, \tag{5.10}$$

$$\Phi_1 = \sqrt{N_\mathrm{I}}\frac{1}{a_\perp\sqrt{a_x}\pi^{3/4}}\frac{\sqrt{2}x}{a_x}e^{-\frac{y^2+z^2}{2a_\perp^2}-\frac{x^2}{2a_x^2}}. \tag{5.11}$$

In the experiment the impurity energy gap of ground and excited state is measured via Ramsey sequences. For the total energy of the impurity we have to add up $E_\mathrm{I} = E_{\mathrm{I\,kin}} + E_{\mathrm{I\,pot}} + E_\mathrm{IB}$, using the corresponding wave functions, Eq. (5.6) and Eq. (5.7):

$$E_{\mathrm{I},\,0} = N_\mathrm{I}\hbar\left(\frac{\omega_x}{4}+\frac{\omega_\perp}{2}\right) + N_\mathrm{I}\hbar\left(\frac{\omega_x}{4}+\frac{\omega_\perp}{2}\right) - \frac{g_\mathrm{IB}^2}{g_\mathrm{BB}}\frac{N_\mathrm{I}^2}{a_x a_\perp^2(2\pi)^{3/2}}, \tag{5.12}$$

$$E_{\mathrm{I},\,1} = N_\mathrm{I}\hbar\left(\frac{3\omega_x}{4}+\frac{3\omega_\perp}{2}\right) + N_\mathrm{I}\hbar\left(\frac{3\omega_x}{4}+\frac{3\omega_\perp}{2}\right) - \frac{g_\mathrm{IB}^2}{g_\mathrm{BB}}\frac{3}{4}\frac{N_\mathrm{I}^2}{a_x a_\perp^2(2\pi)^{3/2}}. \tag{5.13}$$

For a single impurity the measured energy gap corresponds to the intuitive expression: $\Delta E_\mathrm{I} = E_{\mathrm{I},\,1} - E_{\mathrm{I},\,0}$. For an impurity BEC care has to be taken as according to Eq. (5.3) $\mu_\mathrm{I} = E_\mathrm{I}/N_\mathrm{I}$. So in general the gap can be calculated by $\mu_\mathrm{I}^1 - \mu_\mathrm{I}^0$:

$$\begin{aligned}\Delta\mu_\mathrm{I} &= E_{\mathrm{I},\,1}/N_\mathrm{I} - E_{\mathrm{I},\,0}/N_\mathrm{I} \\ &= \frac{\hbar^2}{2m_\mathrm{I}}\frac{1}{a_x^2} + \frac{m_\mathrm{I}}{2}a_x^2\omega_x^2 + \frac{g_\mathrm{IB}^2}{g_\mathrm{BB}}\frac{N_\mathrm{I}}{4a_x a_\perp^2(2\pi)^{3/2}}.\end{aligned} \tag{5.14}$$

Experimentally, we determine the corresponding interaction shifts with a differential measurement of the gaps $\Delta\mu_\mathrm{I}$ with and without background. The value we are interested in is $\Delta\mu_\mathrm{I}^\mathrm{int} - \Delta\mu_\mathrm{I}^0$:

$$\Delta\mu_\mathrm{I}^\mathrm{int} - \Delta\mu_\mathrm{I}^0 = \frac{g_\mathrm{IB}^2}{g_\mathrm{BB}}\frac{N_\mathrm{I}}{4a_x a_\perp^2(2\pi)^{3/2}}. \tag{5.15}$$

Up to some constants the result is given by the impurity density ($N_\mathrm{I}/a_x a_\perp^2$), the impurity-BEC and BEC-BEC interaction. Assuming a symmetric superposition, half of the impurity density can be assigned to the ground state and half of the density to the excited state. This has to be accounted for by dividing the above expression by a factor of 2.
Ground and excited state shift in the same direction and proportional to the transversal impurity density $n_\mathrm{I}^\mathrm{2D} = \frac{N_\mathrm{I}}{a_\perp^2}$ in the respective states:

$$\Delta\mu_{\mathrm{I},\,0} = -\mathrm{const}\cdot n_{\mathrm{I},\,0}^\mathrm{2D}, \tag{5.16}$$

$$\Delta\mu_{\mathrm{I},\,1} = -\mathrm{const}\cdot\frac{3}{4}\cdot n_{\mathrm{I},\,1}^\mathrm{2D}, \tag{5.17}$$

Due to the compact shape of the ground state in lattice direction, its shift is $\frac{4}{3}$ stronger. Its higher density allows for a higher interaction strength. The density of the two states can be related to the total density by the excited fraction η_{ex}: $n^{\mathrm{2D}}_{\mathrm{I},\,1} = \eta_{\mathrm{ex}} n^{\mathrm{2D}}_{\mathrm{I},}$, $n^{\mathrm{2D}}_{\mathrm{I},\,0} = (1-\eta_{\mathrm{ex}}) n^{\mathrm{2D}}_{\mathrm{I}}$. There is a critical value for the excited fraction η_{ex} at which the different shape is compensated by a higher occupation of the excited state, resulting in no change of the trap level gap due to interaction with the background. The value is $\eta_{\mathrm{ex}} = \frac{4}{7}$.
In order to compare our analytical model to numerical 1D calculations, we will now adapt the above scenario to a 1D situation. The relevant expressions are:

$$a_x = \sqrt{\frac{\hbar}{m\omega_x}}, \tag{5.18}$$

$$\Phi_0 = \sqrt{N_{\mathrm{I}}} \frac{1}{\sqrt{a_x}\pi^{1/4}} e^{-\frac{x^2}{2a_x^2}}, \tag{5.19}$$

$$\Phi_1 = \sqrt{N_{\mathrm{I}}} \frac{1}{\sqrt{a_x}\pi^{1/4}} \frac{\sqrt{2}x}{a_x} e^{-\frac{x^2}{2a_x^2}}, \tag{5.20}$$

$$\Delta\mu_{\mathrm{I}}^{\mathrm{int}} - \Delta\mu_{\mathrm{I}}^{0} = \frac{g_{\mathrm{IB}}^2}{g_{\mathrm{BB}}} \frac{N_{\mathrm{I}}}{4a_x\sqrt{2\pi}}. \tag{5.21}$$

The characteristic features of this expression are shown in Fig. 5.1 and compared to numerical results.
In general, it has to be discussed if the condensed bosonic impurity is better described by a Gaussian wave function or (at least for high atom numbers) a Thomas-Fermi profile. The typical trapping frequencies for a bosonic impurity are: $\omega = 2\pi \cdot (26300, 210, 460)\,\mathrm{s}^{-1}$. The corresponding harmonic oscillator length is $a_{\mathrm{HO}} = (0.24, 2.6, 1.8)\mu\mathrm{m}$. Calculating the Thomas-Fermi radii (see Eq. (3.25)) for 3000 atoms, which is a typical value for a highly occupied lattice site results in $r_{\mathrm{TF}} = (0.094, 11, 5.3)\mu\mathrm{m}$. So in the Thomas-Fermi description the impurity is even more anisotropic than the corresponding harmonic oscillator wave functions. The reason for the small extension of the wave function in lattice direction is the lack of kinetic energy that usually increases its size. An extension of a weakly repulsive BEC smaller than the single-atom extension of a wave function $r_{\mathrm{TF}} < a_{\mathrm{HO}}$ is not reasonable. Therefore in lattice direction the use of a Gaussian shape is convincing. The transversal extension will become a parameter $N_{\mathrm{I}}/a_\perp^2$ describing the 2D impurity density in the next section, enabling the comparison between different theories without restricting this ansatz to a certain transversal extension.

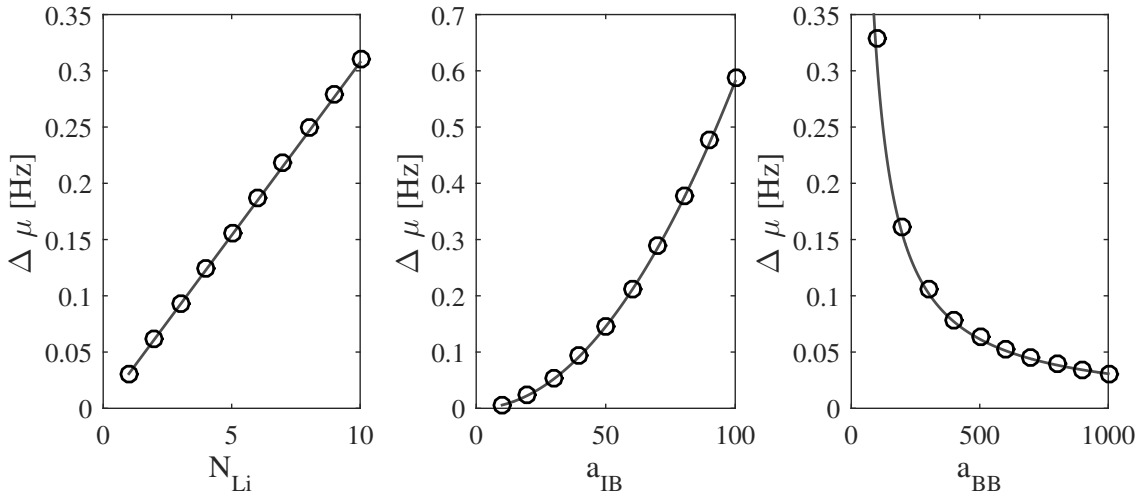

Figure 5.1: Comparison of the numerical solution of the coupled Gross-Pitaevskii equations (circles) to the analytic model of Eq. (5.21) (line). In the regime where the analytic model is valid, it not only reproduces the scaling of the numerics, but also the absolute values agree.

5.1.2 Numerical Model

As we are interested in the ground and excited state of the impurity, we use the Newton method: The basic idea of this method is that the function $f(\Psi) = H\Psi - \mu\Psi$ has a zero even for Ψ being an excited state. Thus, the Newton method can be applied to f but the starting conditions (Ψ_{in}) have to be chosen well. The numerical code used here is based on a version that has been used to describe a Rb mixture of two hyperfine states [86]. Since we want to test our analytic model, which is easily translated into 1D, it is sufficient to use numerics in 1D. The healing length of the condensate in 1D is given by $\xi = a_\perp/\sqrt{2a_{\text{BB}}\tilde{n}}$ [87], where $\tilde{n}$ is the 1D density. To consider the simplest case of uniform external potential for the BEC, we use periodic boundary conditions for the BEC. Left and right edge are connected, thereby creating a ring shape. The impurity is trapped in a harmonic potential with trap frequency ω_0. Using the above detailed procedure to numerically find the stationary solutions of our coupled systems we expect to find the results of the model described before as long as the Thomas-Fermi approximation for the BEC is valid. In Fig. 5.2 the procedure is described. As a guess for Φ we use a harmonic oscillator ground (upper row) and excited state (lower row) and for Ψ we use a flat density distribution, which are exact solutions for the case without interaction (first column). The numerical calculation solve the coupled Eq. (5.3), leading to a distortion of the initial guess for Ψ and Φ (see second column). By bare eye only the modulation of the BEC is visible. The right column provides the difference in density due to the coupling of Na and Li.

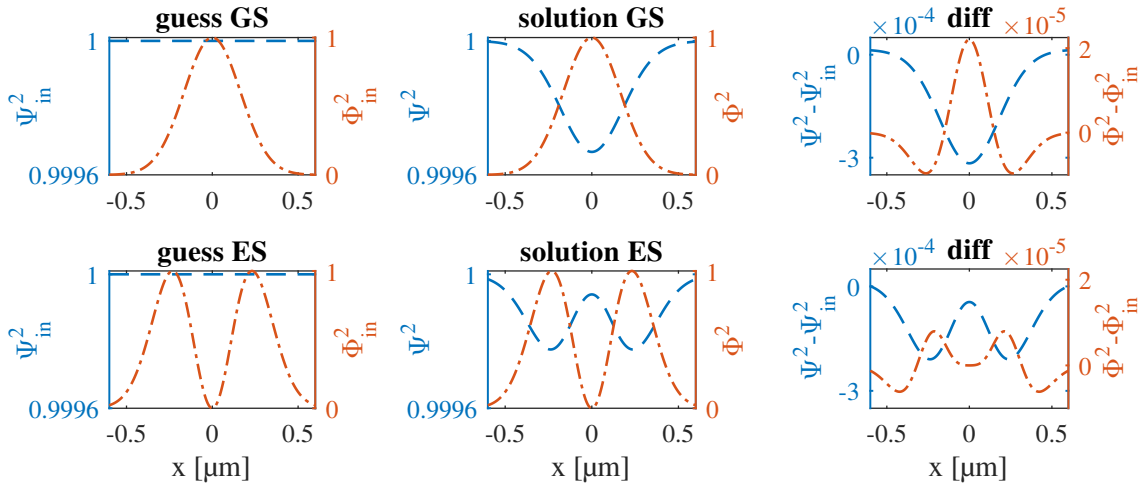

Figure 5.2: Working principle of the numerical solution of coupled Gross-Pitaevskii equations in 1D. The upper row shows the Na (blue) and Li (red) density in the ground state, the lower row the excited state. The plotted functions are normalized to their maximum value. The first column shows the starting densities (non-interacting), the second column the results for numerically found stationary states (interacting). In the right column the difference between interacting and non-interacting solution is shown.

In this example, the interaction is repulsive, which leads to a dip of the sodium BEC with the shape of the impurity density. The impurity density is compressed due to interaction and the peak density is increased.

The background-induced frequency shift we are interested in can be calculated using $\Delta\mu_{\mathrm{I}}^{\mathrm{int}} - \Delta\mu_{\mathrm{I}}^{0}$. In order to obtain the difference $\Delta\mu$, ground and excited state have to be calculated. As the reference, the non interacting case is determined by setting g_{IB} to zero. In total for each calculation of the interaction induced change of the energy gap the complete numerical procedure has to be repeated four times.

As a test for the validity of the analytic model, the ratio of numerical results and analytics is plotted in Fig. 5.3. For small ξ the analytic model is valid. It starts to deviate as soon as the healing length ξ is larger than the harmonic oscillator length. This can easily be understood: The Thomas-Fermi approximation gives good agreement if $N_{\mathrm{B}} a_{\mathrm{BB}}/a \gg 1$ [65, p. 157]. So ξ must be small compared to the the size of the impurity. Only in this case, the BEC density can adapt to the impurity density. In the analytic model the BEC modification is fixed to the shape and size of the impurity in all settings, which corresponds to the limit of a vanishing healing length. Deformation on a small length scale causes high overlap and thereby high interaction energy. Therefore $\Delta\mu$ is overestimated, resulting in a small ratio $\Delta\mu_{\mathrm{num}}/\Delta\mu_{\mathrm{ana}}$. For

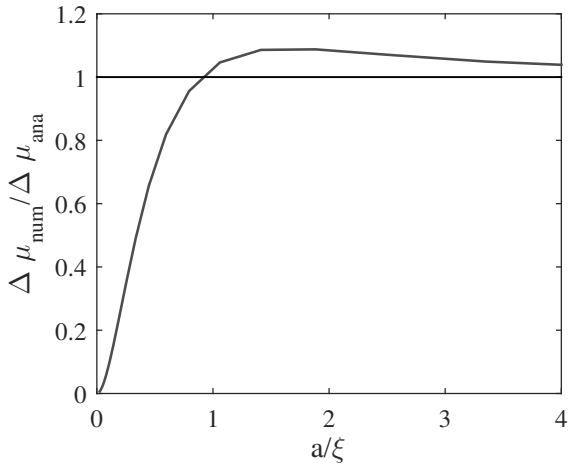

Figure 5.3: Test of the analytic model by comparing the obtained gap with a numerical solution of the coupled Gross-Pitaevskii equations. The ratio a/ξ compares the length scale of the BEC to the harmonic oscillator length of the impurity. For small ξ simulated and calculated energies coincide. For large ξ the analytic model overestimates the cross interaction, as the numerics find that the BEC cannot adapt to the impurity shape.

$\xi \approx a$ and smaller it is easy to calculate the cross interaction of the impurity and the BEC with the analytic model described in the previous subsection.

In order to get a further understanding, we compute the kinetic and potential energy as well as intra-species and interspecies interaction energy and compare them in Table 5.1. The assumed harmonic oscillator frequency for the impurity is $\omega_0 = 2\pi \cdot 27\,\mathrm{kHz}$. The table's upper panel is for large sodium interspecies scattering lengths, the lower part is for small ones, resulting in short and long healing length, respectively. For sodium, only the contribution of the deformation is given. The potential energy vanishes as $V = 0$ for the BEC. In the analytic model, the kinetic energy of the BEC is zero, as this is the main assumption of the Thomas-Fermi approximation. In the upper part analytic and numeric approach agree. In the lower part the numerics give a kinetic energy for the BEC, showing that it cannot be neglected. Further the interspecies interaction energy is overestimated in the analytic scenario due to the perfect overlap. Hence at short a/ξ values the BEC is not described correctly in Thomas-Fermi approximation. Therefore the values for the cross interaction do not agree.

In the experiment, the sodium BEC is harmonically trapped and thus lithium atoms probe a BEC density between zero and a maximal value. This leads to a ξ distribution between $0.2\,\mu\mathrm{m}$ at the peak density and ∞. This has to be compared to the impurity

Table 5.1: List of energy contributions (kinetic, potential, intra- and interspecies interaction energy) calculated both numerically (nu) and analytically (an). The upper panel is for $a_{\mathrm{BB}} = 1000a_0$, the lower part for $a_{\mathrm{BB}} = 1a_0$ where the Thomas-Fermi approximation is invalid, resulting in disagreement between the two methods.

	GS				ES			
E [Hz]	Li an	Li nu	Na an	Na nu	Li an	Li nu	Na an	Na nu
kin	$\nu_0/4$	$\nu_0/4 + 0.02$	0	0.00	$\nu_0 3/4$	$\nu_0 3/4 + 0.04$	0	0.00
pot	$\nu_0/4$	$\nu_0/4 - 0.02$	0	0	$\nu_0 3/4$	$\nu_0 3/4 - 0.04$	0	0
intra	0	0	0.12	0.11	0	0	0.09	0.08
inter	-0.12	-0.12	-0.12	-0.12	-0.09	-0.08	-0.09	-0.08
kin	$\nu_0/4$	$\nu_0/4 + 2$	0	9	$\nu_0 3/4$	$\nu_0 3/4 + 3$	0	6
pot	$\nu_0/4$	$\nu_0/4 - 2$	0	0	$\nu_0 3/4$	$\nu_0 3/4 - 3$	0	0
intra	0	0	123	29	0	0	92	25
inter	-123	-47	-123	-47	-92	-36	-92	-36

harmonic oscillator length of 0.25 µm. In Fig. 5.8 the calculated ξ distribution for ^{6}Li is shown, in Fig. 5.11 the distribution for ^{7}Li, respectively. In the center of the BEC, where the density is high, it is justified to use the Thomas-Fermi approximation, at the border of the BEC this is questionable. So the analytic model is not perfectly valid but should still yield a reasonable estimate.

In summary, we can calculate the impurity energy difference due to interaction well with the simple analytic model as long as the Thomas-Fermi approximation is valid.

5.1.3 Variational Method

In our analytical model, we set the BEC deformation length scale to be the harmonic oscillator length of the impurity. We observed that for $a < \xi$ this cannot be true. Using another ansatz in which the impurity and BEC deformation are described by harmonic oscillator states, but with independent widths, it can be shown that for $a > \xi$ both have the same size (the harmonic oscillator length of the impurity). For $a < \xi$ the BEC density is modulated on a length scale of ξ, the smallest length scale it can react to. This implies that in Eq. (5.15) the harmonic oscillator length a has to be replaced by ξ for small a. Due to the length of the calculation and its intuitive result it is not shown here, but we will come back to this point in section 5.3.

5.2 Fröhlich Hamiltonian and Self-Energy by Green's Function

The full many-body Hamiltonian for interacting mixtures cannot be solved exactly. Up to now we have discussed the Gross-Pitaevskii approach. Another method for describing an impurity atom in a BEC is the Fröhlich Hamiltonian. As long as the interspecies interactions are sufficiently weak only the lowest lying harmonic excitations of the BEC (phonons, see subsection 3.1.3) affect the impurity properties. In this case the complexity of the full Hamiltonian can be reduced by performing the Bogoliubov approximation with respect to the BEC degrees of freedom. The resulting mathematical description is referred to as Fröhlich model and was first derived in the 1950s in connection with the electron-phonon interaction in semiconductors [12, 13, 27, 32]. Although this model is not exactly solvable, too, it offers a very intuitive picture as it allows for an effective description of impurity dynamics in terms of quasiparticles called polarons. The Hamiltonian reads:

$$H = \sum_k E_k \, \hat{a}_{\mathbf{k}}^\dagger \hat{a}_{\mathbf{k}} + \sum_q \omega_q \, \hat{b}_{\mathbf{q}}^\dagger \hat{b}_{\mathbf{q}} + \sum_{k,q\neq 0} V_{\mathbf{q}} \hat{a}_{\mathbf{k}+\mathbf{q}}^\dagger \hat{a}_{\mathbf{k}} (\hat{b}_{\mathbf{q}} + \hat{b}_{-\mathbf{q}}^\dagger), \tag{5.22}$$

where E_k describes the energy levels of the bare impurities and ω_q correspondingly the energy of the uncoupled phonons. The creation and annihilation operators for the impurity are represented by $\hat{a}_{\mathbf{k}}^\dagger$ and $\hat{a}_{\mathbf{k}}$. For the phonons they are denoted by $\hat{b}_{\mathbf{q}}^\dagger$ and $\hat{b}_{\mathbf{q}}$, respectively. The last term describes the density-density interaction between impurity and BEC. Here the absorption or emission of a phonon changes the momentum of the impurity atom, characterized by the coupling strength $V_{\mathbf{q}}$:

$$V_{\mathbf{q}} = \lambda \left[(\xi q)^2 / ((\xi q)^2 + 2) \right]^{1/4}, \tag{5.23}$$

where the BEC-impurity interaction amplitude is described by $\lambda = g_{\mathrm{IB}} \sqrt{n_{\mathrm{B}}}$, see e. g. [27, 31, 32, 88]. For further reading [17, 89] is recommended.

In collaboration with Andreas Komnik (ITP Uni Heidelberg) the self-energies of the two lowest external impurity states considering the coupling to a BEC have been derived. Due to the relative weakness of the interspecies interaction one can use perturbation theory in order to access the single-particle impurity properties. The most convenient approach is the Feynman diagrammatic expansion. It allows for the computation of the Green's function, which is the key quantity of the approach and from which one can extract energy shifts as well as effective parameters of the impurities. For weak λ the leading order process is $\sim \lambda^2$ and corresponds to emission/absorption and reabsorption/reemission of the same phonon by the impurity. The lowest order self-energy approximation takes into account an infinite series of

these processes taking place one after the other in an uncorrelated manner. The terms of order λ are zero and therefore not calculated. It is this coupling to phonons that leads to a mass renormalization of a free particle (polaron) and to the Lamb shift for a bound particle. The actual self-energy calculation assumes zero temperature and a uniform 3D BEC of density n_B and healing length ξ, see Eq. (3.28).

The self-energy for a free particle can be interpreted as an impurity with an effective mass. In case of a bound particle the shift of the energy levels corresponds to the Lamb shift known from the hydrogen atom. Still, the electron mass used to compute the (uncoupled) energy levels of the atom is mainly caused by the coupling of the electron to the vacuum. In order to further illustrate the comparison we calculate the effective mass of a free impurity atom in a uniform BEC in the same manner as for the electron in vacuum [17]. To first order, the mass increase is $m_\mathrm{I}^*/m_\mathrm{I} = 1 + \nu\alpha$, where α is the dimensionless interaction strength and ν and α are given by:

$$\nu = \frac{4}{3\pi}\left(1+\frac{m_\mathrm{I}}{m_\mathrm{B}}\right)^2 \int_0^\infty \mathrm{d}x \sqrt{\frac{x^2}{2+x^2}} \frac{x^4}{\left(x^2 + \frac{m_\mathrm{I}}{m_\mathrm{B}} x\sqrt{2+x^2}\right)^3}, \tag{5.24}$$

$$\alpha = \frac{a_\mathrm{IB}^2}{a_\mathrm{BB}\xi}. \tag{5.25}$$

The integrals can be calculated for the mass ratios employed in our setup. For ^{6}Li ($m_\mathrm{I}/m_\mathrm{B} = 6/23$) $\nu = 0.36$, for ^{7}Li ($m_\mathrm{I}/m_\mathrm{B} = 7/23$) $\nu = 0.34$. Using additionally typical experimental values for the sodium BEC healing length ($\xi = 0.33\,\mu\mathrm{m}$ for ^{6}Li; $\xi = 0.66\,\mu\mathrm{m}$ for ^{7}Li) we get $m_\mathrm{I}^*/m_\mathrm{I} = 1 + 6\cdot 10^{-3}$ and $m_\mathrm{I}^*/m_\mathrm{I} = 1 + 2.2\cdot 10^{-4}$ (^{6}Li, ^{7}Li). The mass increase causes a reduction of the trap energy levels as $\omega^*/\omega = \sqrt{m/m^*}$. The shift of the harmonic oscillator states due to increased mass results in:

$$\Delta E^\mathrm{meff} = E^* - E \tag{5.26}$$

$$= \hbar\omega^*(n+1/2) - \hbar\omega(n+1/2) \qquad \omega^* = \omega\sqrt{m/m^*} \tag{5.27}$$

$$= \hbar\omega(n+1/2)(\sqrt{m/m^*} - 1) \qquad \sqrt{m/m^*} = 1 - 1/2\nu\alpha \tag{5.28}$$

$$= \hbar\omega(n+1/2)(-1/2\nu\alpha), \tag{5.29}$$

$$\Delta E_0^\mathrm{meff} = -\frac{\nu\alpha\hbar\omega}{4}, \tag{5.30}$$

$$\Delta E_1^\mathrm{meff} = -\frac{3\nu\alpha\hbar\omega}{4}. \tag{5.31}$$

The shift due to the increased mass is of the same order of magnitude as the self-energy shifts. Still, the gap between ground and excited state is reduced in case of an increased mass which is not true for the shifts derived for a bound state. Here the downshift of the ground state is stronger than the shift of the excited state, increasing the gap. In Fig. 5.4 the energy shift of ground and excited state as a function of the sodium BEC characteristics (a/ξ) for ^{7}Li are plotted.

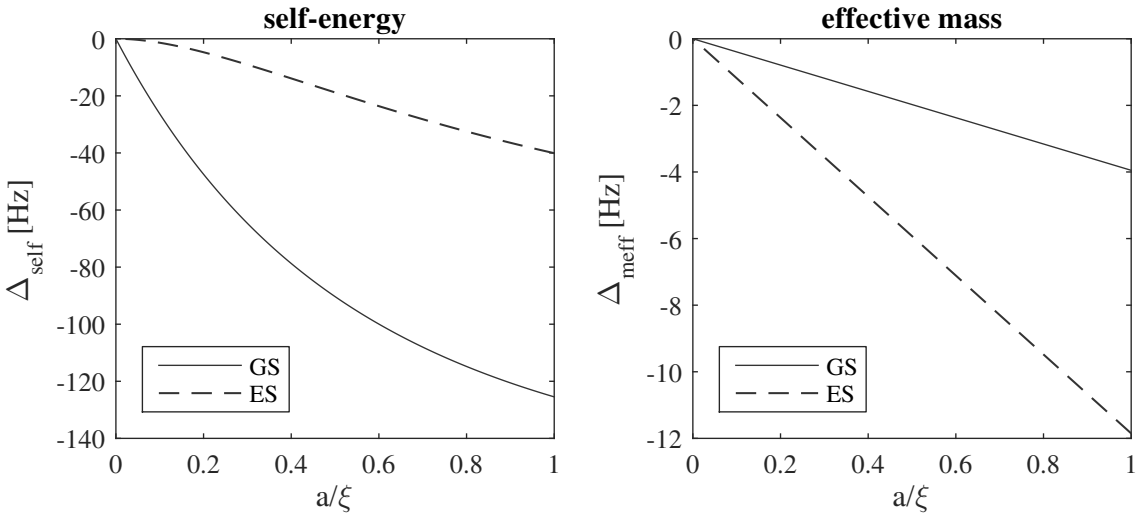

Figure 5.4: Phononic coupling causes a mass increase for free particles and level shifts for bound particles (left panel). The mass increase by itself shifts energy levels (right panel). The levels are denoted by GS (ES) for the ground (excited) state, respectively. The mass increase reduces the gap, as the upper state shifts stronger, unlike the self-energy behavior. Here the situation is plotted for bosonic impurities. Bosonic enhancement in case of the self-energy shift causes larger absolute values.

In case of confined impurities, the calculation assumes a potential with trapping frequency ω_0 in lattice direction, giving rise to the length scale $a = \sqrt{\hbar/\omega_0 m_\mathrm{I}}$ in x-direction and transversally free impurities. The impurities occupy the two lowest lying states in lattice direction. Their eigenstates have energies $E_{n,k} = \hbar\omega_0(n + 1/2) + \hbar^2 k^2/2m_\mathrm{I} - \mu$, where $\mathbf{k}$ is a 2D wave vector and n labels the state of the confinement potential. The bare impurity Hamiltonian is:

$$H_\mathrm{I} = \sum_n \int \frac{\mathrm{d}^2\mathbf{k}}{(2\pi)^2} E_{n,k}\, \hat{a}^\dagger_{n,\mathbf{k}} \hat{a}_{n,\mathbf{k}}\,. \tag{5.32}$$

The impurities are scattered on the harmonic modes of the BEC. The corresponding interaction terms have been derived in the weak depletion limit in [27]. Adapting it to the present setup leads to the following interaction term:

$$H_\mathrm{int} = \int \frac{\mathrm{d}^2\mathbf{k}}{(2\pi)^2} \int \frac{\mathrm{d}^3\mathbf{q}}{(2\pi)^3} \sum_{n_1,n_2} V_\mathbf{q}\, A(n_1, n_2, q_x) \times \hat{a}^\dagger_{n_1,\mathbf{k}+\mathbf{q}'} \hat{a}_{n_2,\mathbf{k}} (\hat{b}_\mathbf{q} + \hat{b}^\dagger_{-\mathbf{q}}), \tag{5.33}$$

where $\mathbf{q}' = (q_y, q_z)$ denotes the transverse component of $\mathbf{q}$. A is the matrix element for the transition between the harmonic oscillator energy levels:

$$A(n_1, n_2, q_x) = \int \mathrm{d}x\, \Phi^*_{n_1}(x)\, \Phi_{n_2}(x)\, e^{-iq_x x}, \tag{5.34}$$

$\Phi_n(x)$ are the wave functions of the n-th eigenstate. The Hamiltonian of the phonons is

$$H_{\mathrm{ph}} = \int \frac{\mathrm{d}^3\mathbf{q}}{(2\pi)^3}\,\omega_q\,\hat{b}^\dagger_{\mathbf{q}}\hat{b}_{\mathbf{q}}, \tag{5.35}$$

where $\omega_q = cq\sqrt{1+(\xi q)^2/2}$ with the sound velocity c, see subsection 3.1.3. Matrix elements for the impurity-phonon scattering are given by Eq. (5.23). The weak interspecies interaction g_{IB} allows a perturbative treatment of the problem (see beginning of this subsection). The necessary Green's functions have the same shape for both bosonic and fermionic case. For fermions, an equal superposition of the two lowest states in the direction of strong confinement is assumed. Both states shift downwards, reducing their energy. Due to its smaller spatial extension, the ground state shifts stronger than the excited state, approximately by a factor of two. As the shift depends on a and ξ, the necessary numerical integrals are calculated at several sampling points (up to $a/\xi = 0.8575$) and fitted by a numerical approximation of $\Delta E(a/\xi)$. It reads:

$$\Delta E\left(\frac{a}{\xi}\right) = \frac{\lambda^2 m_{\mathrm{B}}}{8\pi^2\hbar^2\xi} f\left(\frac{a}{\xi}\right), \tag{5.36}$$

$$f\left(\frac{a}{\xi}\right) = -0.11 + \frac{0.95}{a/\xi}. \tag{5.37}$$

This result is implicitly dependent on the impurity density. A typical experimental value for the chemical potential was used for the evaluation. For 600 atoms in the central pancake the chemical potential is about 15 kHz.

In case of bosonic impurities, strong shifts can be generated due to bosonic enhancement. In particular the scattering by phonons into occupied states is enhanced. This macroscopic occupation dominates and thermal atoms (occupation number small, around one) are neglected. The increased signal results in higher sensitivity and allows for an enhanced experimental study. The fundamental coupling mechanism is scattering, therefore the impurity density is important as well. Due to the presence of the lattice potential, in this scenario the 2D density has to be employed. The shift of ground ($\Delta\mu_0$) and excited ($\Delta\mu_1$) state are calculated in dependence of the relative densities of impurity states ($n^{\mathrm{2D}}_{\mathrm{I},\,0}$, $n^{\mathrm{2D}}_{\mathrm{I},\,1}$). The 2D densities can be related to the calculated atomic densities taking into account the relative excitation η_{ex}:

$$n^{\mathrm{2D}}_{\mathrm{I},\,0} = (1-\eta_{\mathrm{ex}})n^{\mathrm{2D}}_{\mathrm{Li,\,BEC}}, \tag{5.38}$$

$$n^{\mathrm{2D}}_{\mathrm{I},\,1} = \eta_{\mathrm{ex}} n^{\mathrm{2D}}_{\mathrm{Li,\,BEC}}. \tag{5.39}$$

$\Delta\mu$ is used to describe the level shift for bosons, as E has been used to describe the total energy of an atomic cloud and $\Delta\mu = \Delta E/N_{\mathrm{I}}$. For bosonic impurities the

expressions for the level shifts and the cross interaction are given by the following terms:

$$\Delta\mu_{00} = -\frac{\lambda^2 m_\mathrm{B}}{8\pi^2\hbar^2\xi} n^0_{\mathrm{I,\,2D}} \left[\sqrt{32}\pi^2\xi^2 \exp\left(\frac{a^2}{\xi^2}\right)\left(1-\mathrm{erf}\left(\frac{a}{\xi}\right)\right)\right], \tag{5.40}$$

$$\Delta\mu_{01} = -\frac{\lambda^2 m_\mathrm{B}}{8\pi^2\hbar^2\xi} n^1_{\mathrm{I,\,2D}} \left[4\pi a^2 \int_0^\infty d\eta_x \eta_x^4 \frac{\exp\left(-\frac{a^2\eta_x^2}{2\xi^2}\right)}{\eta_x\left(1+\frac{\eta_x^2}{2}\right) - 2\left(\frac{m_\mathrm{B}}{m_\mathrm{I}}\frac{\xi^2}{a^2}\right)^2}\right], \tag{5.41}$$

$$\Delta\mu_{11} = -\frac{\lambda^2 m_\mathrm{B}}{8\pi^2\hbar^2\xi} n^1_{\mathrm{I,\,2D}} \left[\sqrt{32\pi^3}\xi a - \sqrt{32}\pi^2 a^2 \exp\left(\frac{a^2}{\xi^2}\right)\left(1-\mathrm{erf}\left(\frac{a}{\xi}\right)\right)\right], \tag{5.42}$$

$$\Delta\mu_{10} = -\frac{\lambda^2 m_\mathrm{B}}{8\pi^2\hbar^2\xi} n^0_{\mathrm{I,\,2D}} \left[\pi\xi^2 \int_0^\infty d\eta_x \eta_x^2 \left(1-\frac{a^2\eta_x^2}{\xi^2}\right)^2 \frac{\exp\left(-\frac{a^2\eta_x^2}{2\xi^2}\right)}{\eta_x\left(1+\frac{\eta_x^2}{2}\right) - 2\left(\frac{m_\mathrm{B}}{m_\mathrm{I}}\frac{\xi^2}{a^2}\right)^2}\right]. \tag{5.43}$$

Here $\Delta\mu_{01}$ denotes a shift of the ground state due to occupation of the excited state. Calculating the numbers in the relevant parameter regime reveals that the cross terms $\Delta\mu_{01}$ and $\Delta\mu_{10}$ are one order of magnitude smaller and can be neglected. This facilitates numerical calculations, as no integrals have to be solved.

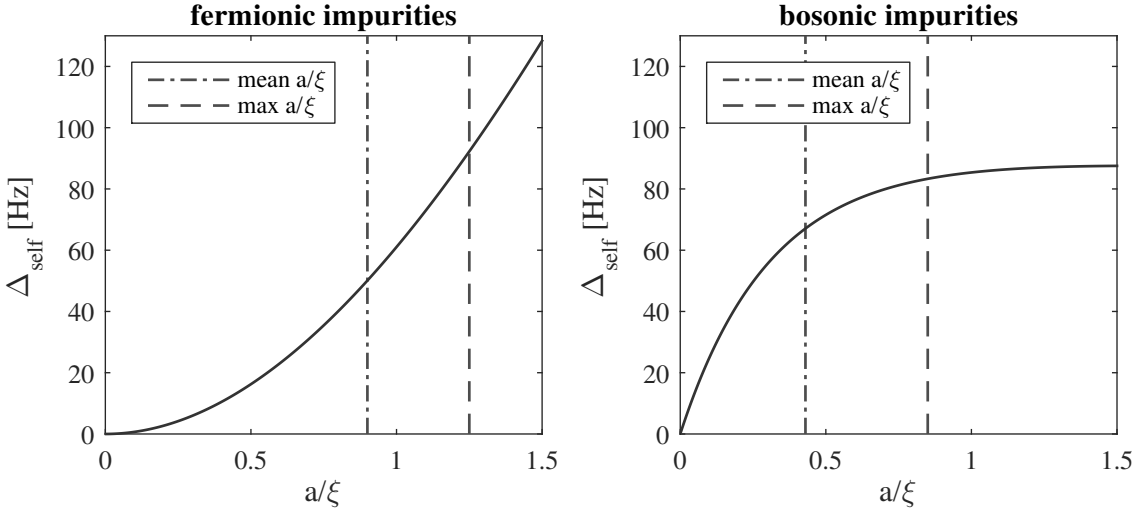

Figure 5.5: Healing length dependence of the energy level gap due to phononic coupling. For bosonic impurities this function additionally depends on the 2D impurity density. Here $n^{\mathrm{2D}}_{\mathrm{Li,\,BEC}} = 38\,\mu\mathrm{m}^{-2}$ in a symmetric superposition is plotted. Experimentally relevant a/ξ values are depicted by vertical bars.

In Fig. 5.4 $\Delta\mu_{00}$ and $\Delta\mu_{11}$ are depicted as a function of a/ξ. Further, we can now study the dependence of the energy gap $\Delta\mu = \Delta\mu_{11} - \Delta\mu_{00}$ on the ratio a/ξ for bosonic and fermionic impurities. The result is plotted in Fig. 5.5. High BEC densities correspond to a short healing length. Hence we get the intuitive result that higher BEC densities cause larger shifts. For bosonic impurities this function saturates at about $a/\xi = 1$. Note that for describing the experimental results, one has to keep in mind that we realize many different ξ in one experimental run. Due to the non-linearity of the functions we have to consider the distribution of ξ.

The shift of the ground state $\Delta\mu_{00}$ and the shift of the excited state $\Delta\mu_{11}$ depend on the impurity occupation of the respective states. For the same 2D density the ground state shifts more than the excited state, see Fig. 5.4. This can be compensated by an increased occupation of the excited state η_{ex}. The critical excitation leading to no change of the energy gap by coupling to the background can be calculated by:

$$(1 - \eta_{\text{ex}})\Delta\mu_{00} = \eta_{\text{ex}}\Delta\mu_{11} \tag{5.44}$$

$$\eta_{\text{ex}} = \Delta\mu_{00}/(\Delta\mu_{00} + \Delta\mu_{11}). \tag{5.45}$$

It is plotted in Fig. 5.6 as a function of the BEC healing length. The mean critical η_{ex} and a/ξ for our ^{7}Li setup are indicated by dashed lines. They do not intersect at the function due to the averaging over the function's non-linearity.

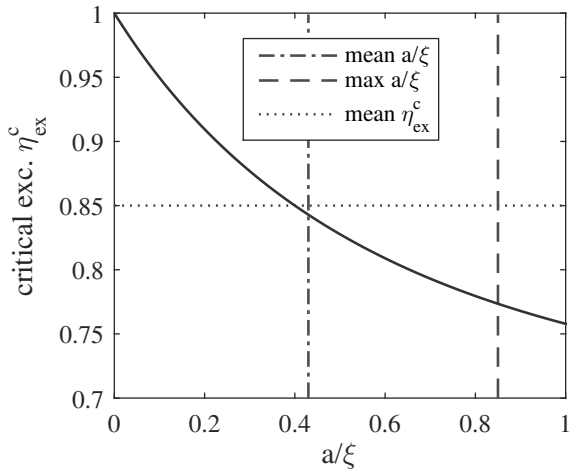

Figure 5.6: The critical excited fraction η_{ex} for a vanishing background induced energy gap change as a function of the BEC healing length. The mean values for averaging over the clouds are plotted as dashed dotted and dotted lines. The highest ratio is depicted by a dashed line.

5.3 Comparison of the two Approaches: Gross-Pitaevskii Equation versus Fröhlich Hamiltonian

The first part of this chapter approached the impurity BEC interaction via the Gross-Pitaevskii equation. In the second part a microscopic treatment via the Fröhlich Hamiltonian was performed. We now investigate if there is a regime where both approaches are valid. As the Gross-Pitaevskii equation works best for high atomic densities, the results of Eq. (5.15) are compared to the self-energy expression for condensed bosons (Eq. (5.40)). It is recast in a form where the mean value of the numerical part is ≈ 1, so that it is justified to neglect it.

$$\Delta\mu_{\mathrm{I}}^{\mathrm{GPE}} = \frac{g_{\mathrm{IB}}^2}{g_{\mathrm{BB}}} \frac{N_{\mathrm{I}}}{4a_z a_\perp^2 (2\pi)^{3/2}} \tag{5.46}$$

$$\Delta\mu_{\mathrm{I}}^{\mathrm{self}} \approx \frac{\lambda^2 m_{\mathrm{B}} \xi}{2\pi\hbar^2} n_{\mathrm{I,\,2D}} \qquad \lambda = g_{\mathrm{IB}}\sqrt{n_{\mathrm{B}}} \tag{5.47}$$

$$= \frac{g_{\mathrm{IB}}^2 n_{\mathrm{B}} m_{\mathrm{B}} \xi}{2\pi\hbar^2} n_{\mathrm{I,\,2D}} \qquad n_{\mathrm{B}} = 1/(8\pi\xi^2 a_{\mathrm{BB}}) \tag{5.48}$$

$$= \frac{g_{\mathrm{IB}}^2 m_{\mathrm{B}}}{16\pi^2\hbar^2 \xi a_{\mathrm{BB}}} n_{\mathrm{I,\,2D}} \qquad g_{\mathrm{BB}} = 4\pi\hbar^2 a_{\mathrm{BB}}/m_{\mathrm{B}} \tag{5.49}$$

$$= \frac{g_{\mathrm{IB}}^2}{4\pi g_{\mathrm{BB}} \xi} n_{\mathrm{I,\,2D}} \qquad n_{\mathrm{I,\,2D}} = N_{\mathrm{I}}/a_\perp^2 \tag{5.50}$$

$$= \frac{g_{\mathrm{IB}}^2}{g_{\mathrm{BB}}} \frac{N_{\mathrm{I}}}{a_\perp^2} \frac{1}{\xi} \frac{1}{4\pi} \qquad \xi \approx a_z \tag{5.51}$$

$$\approx \frac{g_{\mathrm{IB}}^2}{g_{\mathrm{BB}}} \frac{N_{\mathrm{I}}}{a_\perp^2} \frac{1}{a_z} \frac{1}{4(2\pi)^{3/2}} \tag{5.52}$$

$$= \Delta\mu_{\mathrm{I}}^{\mathrm{GPE}}. \tag{5.53}$$

In a parameter regime where a and ξ are of the same order of magnitude the two approaches coincide. The connection is even more universal, as the reason for a to show up in the expression for $\Delta\mu_{\mathrm{I}}^{\mathrm{GPE}}$ is the Thomas-Fermi approximation. For $a > \xi$ the deformation of the BEC is determined by a, for $a < \xi$ the healing length ξ is decisive.

In current literature, it is still a matter of debate whether a classical field theory can calculate an effect based on fluctuations. Some strongly support this view [90–92] but their opinion has been questioned as well [93].

In our case, the comparison works better for bosonic impurities than for fermionic ones, as the structure of the Fermi sea changes the fundamental characteristics of the system. Even for $T = 0$ most of the fermions occupy states with finite momenta

which is not the case for bosons. Furthermore the Gross–Pitaevskii description is best for high atomic densities, which is tenuous for a single fermion.
The deeper foundations causing the accordance are still to be studied in future work.

5.4 Effect on Lithium by the Sodium BEC Modulation Resulting from the Lattice

Our studies have shown that an impurity atom in a BEC distorts the condensate. This change in BEC density changes the effective impurity potential, altering the energy levels of the trapped states. However, in practice this effect has to be differentiated from the impact by modifications of the otherwise flat BEC via an external potential. In our experiment this can be observed, as the optical potential used to address the impurities has an effect on the BEC as well. We will call the depth of this potential for the impurity V_I and the depth for the background BEC V_B. Due to the large detuning for sodium, the ratio $V_\mathrm{B}/V_\mathrm{I}$ is small. Using Eq. (3.1) we can calculate the potential for impurity and BEC resulting from the laser intensity $I(\vec{r})$ of the standing light wave at frequency ω_lat. Please note that due to the large detuning for sodium, the application of the rotating wave approximation changes the values by several %, therefore it is not used here. For the resonance frequencies ω_I and ω_B of the impurity and the background atoms, we find a ratio of:

$$\frac{V_\mathrm{I}}{V_\mathrm{B}} = \frac{\omega_\mathrm{B}^3}{\omega_\mathrm{I}^3}\left(\frac{\Gamma_\mathrm{I}}{\omega_\mathrm{lat}-\omega_\mathrm{I}}+\frac{\Gamma_\mathrm{I}}{\omega_\mathrm{lat}+\omega_\mathrm{I}}\right)\left(\frac{\Gamma_\mathrm{B}}{\omega_\mathrm{lat}-\omega_\mathrm{B}}+\frac{\Gamma_\mathrm{B}}{\omega_\mathrm{lat}+\omega_\mathrm{B}}\right)^{-1}. \tag{5.54}$$

We performed experiments ranging from wavelengths of about 670 nm to 672 nm, while the lithium transition is at 671 nm. For the experimentally employed values $V_\mathrm{I}/V_\mathrm{B}$ ranges from $\pm 0.5\,\%$ to $\pm 1.1\,\%$. The change in sign expresses the fact that the potential is always attractive for sodium but can be attractive or repulsive for lithium, depending on the wavelength.
As in subsection 5.1.1 we use the Thomas-Fermi approximation, yielding a BEC density of $n_\mathrm{B} = (\mu_\mathrm{B} - V_\mathrm{B})/g_\mathrm{BB}$. If $\mu_\mathrm{B} \gg V_\mathrm{B}$, we can write this as $n_\mathrm{B} = n_0 - V_\mathrm{B}/g_\mathrm{BB}$. This describes a flat BEC with a modulation of $V_\mathrm{B}/g_\mathrm{BB}$ on top. This modulated BEC density adds a potential for the impurity:

$$\tilde{V_\mathrm{I}} = V_\mathrm{I} + g_\mathrm{IB} n_\mathrm{B} = V_\mathrm{I} - \frac{g_\mathrm{IB}}{g_\mathrm{BB}} V_\mathrm{B} = V_\mathrm{I}\left(1 - \frac{g_\mathrm{IB}}{g_\mathrm{BB}}\frac{V_\mathrm{B}}{V_\mathrm{I}}\right). \tag{5.55}$$

We approximate the potential to be harmonic with trapping frequency ω_0 for the impurity. In this case, the modified trap frequency $\tilde{\omega}/\omega_0 = \sqrt{\tilde{V_\mathrm{I}}/V_\mathrm{I}}$. This leads to a

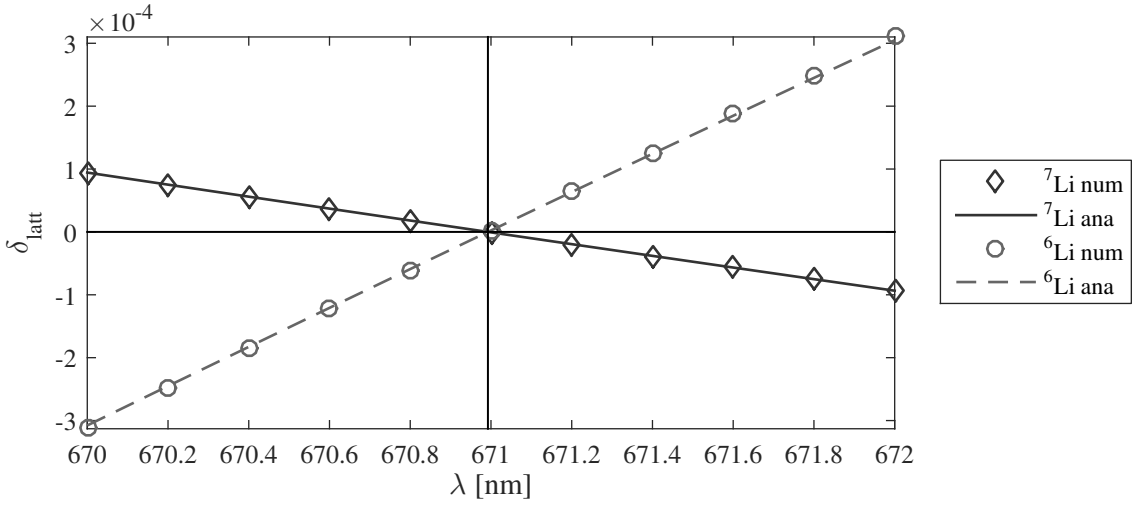

Figure 5.7: The relative frequency change for lithium induced by the external modulation of the sodium BEC through the lattice can be calculated by Eq. (5.56) (lines), as long as the Thomas-Fermi approximation is valid. It can be derived numerically (markers) solving the coupled Gross-Pitaevskii equations, revealing excellent agreement. For ^{7}Li (diamond/line) the effect is weaker and inverted compared to ^{6}Li (circle/dashed line).

relative change of the frequency:

$$\delta_{\mathrm{latt}} = \frac{\Delta\omega}{\omega_0} = \frac{\tilde{\omega}-\omega_0}{\omega_0} = \sqrt{\frac{\tilde{V_\mathrm{I}}}{V_\mathrm{I}}} - 1 = \sqrt{1 - \frac{g_{\mathrm{IB}}}{g_{\mathrm{BB}}}\frac{V_\mathrm{B}}{V_\mathrm{I}}} - 1 = -\frac{1}{2}\frac{g_{\mathrm{IB}}}{g_{\mathrm{BB}}}\frac{V_\mathrm{B}}{V_\mathrm{I}}, \tag{5.56}$$

where the approximation $\sqrt{1+x} \approx 1 + x/2$ has been used. In order to test this expression numerically, several approaches are possible. The modified impurity potential V_I can be calculated and fitted quadratically, the potential can be diagonalized numerically revealing the eigenstates and the corresponding energies or the background potential can be implemented into the numerical solution of the coupled Gross-Pitaevskii equations (see subsection 5.1.2). We will deploy the latter, as it has already been introduced.
The system size is set to a multiple of the lattice spacing to avoid jumps of the potential which is necessary due to the employed periodic boundary conditions. The assumed lattice periodicity is 1.65 µm, as in the experiment, and the system extends over 6 lattice sites. In order to avoid population of several lattice sites, a harmonic potential with curvature ω is assumed for lithium, whereas sodium is exposed to a sine potential. In order to extract the effect induced by the lattice, the lithium energy gap of excited and ground state is calculated. Afterwards the gap of the system without sodium modulation is determined and subtracted. In Fig. 5.7 the potential for lithium is kept constant, while the wavelength of the potential is

scanned. Depending on the wavelength, the intensity of the potential has to be adapted resulting in a different strength for sodium. As long as the wavelength is shorter than 671 nm the potential is repulsive for lithium and attractive for sodium, resulting in lithium being located in sodium density minima. At a wavelength larger than the lithium D-line transitions, the optical potential is attractive for both species, lithium being located in sodium BEC maxima. Therefore, the effect changes sign at the resonance frequency of lithium at $\lambda = 671\,\mathrm{nm}$. For ^{6}Li the potential depth is $25.4\,E_{\mathrm{rec}}$, while for ^{7}Li the depth is $33\,E_{\mathrm{rec}}$, corresponding to a gap of roughly $\omega_0 = 2\pi \cdot (27.25\,\mathrm{kHz})$. The effect of the optical potential on the sodium cloud is calculated by Eq. (5.54). In Fig. 5.7 the prediction of Eq. (5.56) is confirmed, showing a linear dependence on the detuning. Due to the difference in a_{IB}, the slope is larger for fermionic lithium and has opposite sign compared to the bosonic line.
In a regime where Thomas-Fermi approximation is not valid any more, the BEC modulation is suppressed and the analytic model will overestimate the effect. For a full discussion on the validity of the Thomas-Fermi approximation see subsection 5.1.2.

5.5 Signal Constitution for a Sample of Many Impurities

Based on chapter 3 we can calculate and characterize the density distribution of the two-species mixture in the trap. As explained in the previous sections, there are two main contributions to the energy shifts of lithium atoms due to the sodium BEC. Lithium atoms immersed in the sodium BEC experience a background induced energy shift due to the deformation of the BEC by the impurity and due to the deformation of the BEC by the lattice. The strength of the potential change for impurities depends on the position, as the sodium density varies. The read-out averages over the whole lithium sample. Hence, in order to compare our theory to experimental data, we need to take this averaging over the clouds into account.

The time evolution of the coherent superposition is given by $e^{-i\omega t}$ where $\omega = \Delta E/\hbar$. The dominant energetic contribution $\omega_0 \approx 27\,\mathrm{kHz}$ is given by the external potential and gives rise to a phase evolution $\phi = \omega_0 t$. Lithium atoms in contact with the sodium BEC have an additional BEC density dependent energy term, causing a phase evolution $(\omega_0 + \Delta\omega)t = \phi + \epsilon$. The oscillatory phase evolution of the superposition is mapped on an oscillation in the population of states by the second interferometer pulse in the employed Ramsey scheme (see subsection 4.4.2). We observe a sine function in the population of the excited state:

$$\eta_{\mathrm{ex}} = 0.5\sin((\omega_0 + \Delta\omega)t) + 0.5. \tag{5.57}$$

When ω_0 is known, which we need for strong coupling of the external states, the observation of an interference fringe allows the definite determination of $\Delta\omega$. This is especially true as we work at short evolution times t, $\Delta\omega t \ll \pi$. Due to the unambiguous assignment we will not discuss η_{ex}, but the signal, its phase or frequency itself. In the experiment decoherence and dephasing cause decreased amplitudes. These effects reduce the sensitivity, but do not change the unique relation between the excited fraction and the phase evolution.

When scanning the effective phase of the Ramsey readout pulse, a sine shaped fringe is expected. We will now discuss the question, how the signal of various frequencies looks like. First, we can differentiate between lithium atoms in contact with the sodium BEC (immersed fraction η_{im}) and lithium atoms outside the BEC. The latter ones have a phase evolution $\phi = \omega_0 t$. The atoms inside the BEC have an additional phase $\Delta\omega t = \epsilon$. For small ϵ we find:

$$\begin{aligned}
\sin(\phi_{\mathrm{obs}}) =& (1-\eta_{\mathrm{im}})\sin(\phi) + \eta_{\mathrm{im}}\sin(\phi+\epsilon) \\
=& (1-\eta_{\mathrm{im}})\sin(\phi) + \eta_{\mathrm{im}}(\sin(\phi)\cos(\epsilon) + \cos(\phi)\sin(\epsilon)) \\
\approx& (1-\eta_{\mathrm{im}})\sin(\phi) + \eta_{\mathrm{im}}(\sin(\phi) + \epsilon\cos(\phi)) \\
=& \sin(\phi) + \eta_{\mathrm{im}}\epsilon\cos(\phi) \\
\approx& \sin(\phi)\cos(\eta_{\mathrm{im}}\epsilon) + \cos(\phi)\sin(\eta_{\mathrm{im}}\epsilon) \\
=& \sin(\phi + \eta_{\mathrm{im}}\epsilon).
\end{aligned} \tag{5.58}$$

So as long as $\Delta\omega t$ is small, we still expect to observe a sine function at full amplitude with a slightly changed phase compared to the free evolution. However, a problem remains that short times and small frequency shifts are easy to describe but hard to measure due to the finite time of the experimental sequence. We will now take the full density distribution into account. The average frequency shift can be calculated by the weighted arithmetic mean as a sum over many volume elements partitioning the atomic clouds:

$$\begin{aligned}
\Delta\omega &= \frac{\sum_i w_i (\Delta\omega)_i}{\sum_i w_i} \\
&= \sum_{x,y,z} \frac{n_{\mathrm{Li}}^{x,y,z}\mathrm{d}V}{N_{\mathrm{Li}}} \Delta\omega_{x,y,z} \\
&= \frac{1}{N_{\mathrm{Li}}} \int n_{\mathrm{Li}}(\vec{r})\Delta\omega(\vec{r})\mathrm{d}V.
\end{aligned} \tag{5.59}$$

The signal weight is given by the lithium density $n_{\mathrm{Li}}(x,y,z)$. This expression is correct for $t = 0$. In order to expand it to $t > 0$ the oscillatory behavior of the phase evolution has to be regarded. When two atoms accumulate a relative phase of π, their summed signal vanishes. Hence, instead of calculating the weighted mean of

the frequency, the weighted mean value of $\sin(\omega t)$ should be applied:

$$\Delta\omega_{\text{eff}} = \arcsin\left(\frac{1}{N_{\text{Li}}}\int n_{\text{Li}}(\vec{r})\sin\left((\omega_0+\Delta\omega(\vec{r}))t\right)\mathrm{d}V\right)/t. \tag{5.60}$$

Here we assumed that the signal is still given by a sine function, which is legitimate for small phases due to the considerations in Eq. (5.58). The signal amplitude is damped due to decoherence. This effect is due to collisions with sodium and therefore depends on the sodium density. Here the thermal sodium density can be included, but it causes only minor changes. In close analogy to [48] we employ a simple model for decoherence:

$$\Gamma = n_{\text{Na}}\sigma v = n_{\text{Na}} 4\pi a_{\text{IB}}^2\sqrt{\frac{\hbar\omega_0}{4m_{\text{Li}}}}, \tag{5.61}$$

where we assume that the mean velocity can be estimated from the oscillation speed of the superposition of ground and excited state ($\bar{v} = v_{\max}/\sqrt{2}$). The time-dependent signal of the cloud can be calculated by:

$$S(t) = \frac{1}{N_{\text{Li}}}\int n_{\text{Li}}(\vec{r})\exp(-\Gamma(\vec{r})t)\sin\left((\omega_0+\Delta\omega(\vec{r}))t\right)\mathrm{d}V. \tag{5.62}$$

For small $\Delta\omega(\vec{r})$ it is a sine with reduced amplitude:

$$A(t) = \frac{1}{N_{\text{Li}}}\int n_{\text{Li}}(\vec{r})\exp(-\Gamma(\vec{r})t)\mathrm{d}V. \tag{5.63}$$

The reduced amplitude diminishes the slope of the fringe, hence for the extraction of the effective phase $\Delta\omega_{\text{eff}}$ the amplitude cannot be neglected. It has to be taken into account that the weight is time dependent:

$$\sin(\phi_{\text{eff}}(t)) = \frac{\int n_{\text{Li}}(\vec{r})\exp(-\Gamma(\vec{r})t)\sin\left((\omega_0+\Delta\omega(\vec{r}))t\right)\mathrm{d}V}{\int n_{\text{Li}}(\vec{r})\exp(-\Gamma(\vec{r})t)\mathrm{d}V}, \tag{5.64}$$

$$\Delta\omega_{\text{eff}}(t) = \arcsin\left(\sin(\phi_{\text{eff}}(t))\right)/t. \tag{5.65}$$

If large $\Delta\omega(\vec{r})$ become relevant, the amplitude can furthermore be reduced by dephasing. In this case Eq. (5.63) does not yield correct amplitude values (see Fig. 5.12) and therefore Eq. (5.65) is invalid as well. Still, Eq. (5.62) is correct and enables us to calculated the signal at all times, but the analytic derivation of the phase is intractable.

The energy shifts in dependence on the densities have been denoted in section 5.2. The shifts are strongly dependent on the BEC density. In Fig. 5.8 these expressions are applied to the calculated ^{6}Li density distribution. On the left, the distribution of the probed healing length is shown, on the right the corresponding frequencies.

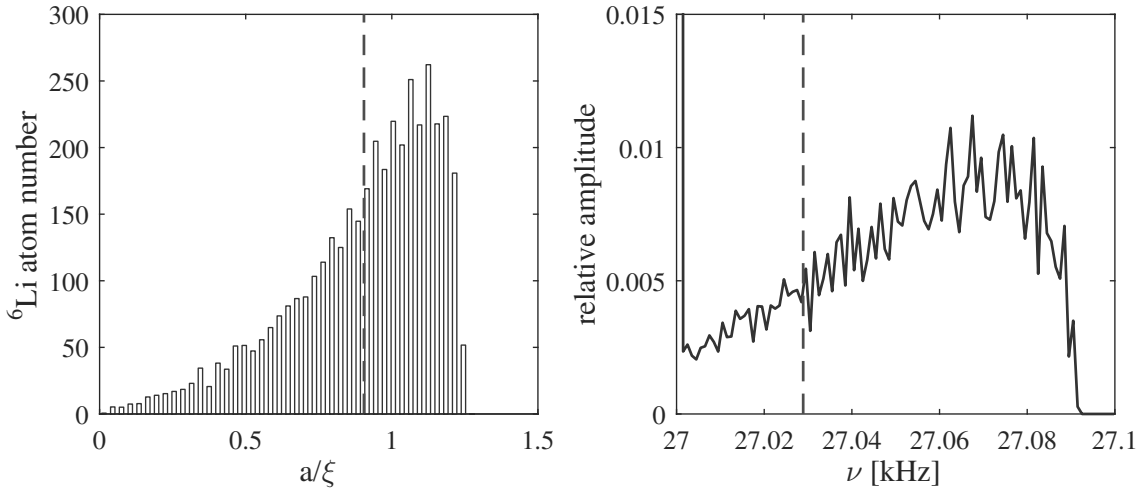

Figure 5.8: The ^{6}Li cloud probes all parts of the sodium BEC, resulting in the shown histogram of the healing length (left). It translates into a distribution of frequencies (right). In both cases the mean values are indicated by vertical bars. On the right lithium atoms outside the BEC are accounted for, but the peak at $\nu_0 = 27\,\mathrm{kHz}$ is truncated for a better recognizability.

There is a difference, as only the immersed fraction $\eta_{\mathrm{im}} = 54\,\%$ of the fermions penetrate the BEC. Therefore the relative amplitude at $\nu_0 = 27\,\mathrm{kHz}$ is 0.46 but cut off to depict the structure of the distribution. The atoms outside the BEC reduce the mean frequency (see Eq. (5.59)) which is not the case for the mean a/ξ value. Some wiggly modulation of the spectrum is observable. Every lattice site has a strong peak at ν_0 and a characteristic extension, given by the maximum sodium density within the volume of the lattice site. Their sum therefore shows an oscillatory shape.

Only for $t = 0$ it is correct to average over the frequencies. For $t > 0$ the oscillatory behavior of the phase has to be taken into account. Further decoherence and dephasing occur. In Fig. 5.9 the distribution of $\sin(\phi)$ is shown (dotted line) for 1.1 ms, the longest experimentally realized evolution time. Dephasing is not significant in this case, as the highest values are about 0.6, corresponding to a phase of $\pi/5$. However, for ^{6}Li decoherence is relevant due to the strong inter-species interaction and high overlap. Employing the decoherence model Eq. (5.61) we see that especially large phases, corresponding to high sodium densities, are greatly reduced (see black line) and their mean value is roughly halved compared to the scenario without decoherence. On the right side, the time evolution of the effective frequency shift is depicted. It can be approximated by a monoexponential decay based on the effective

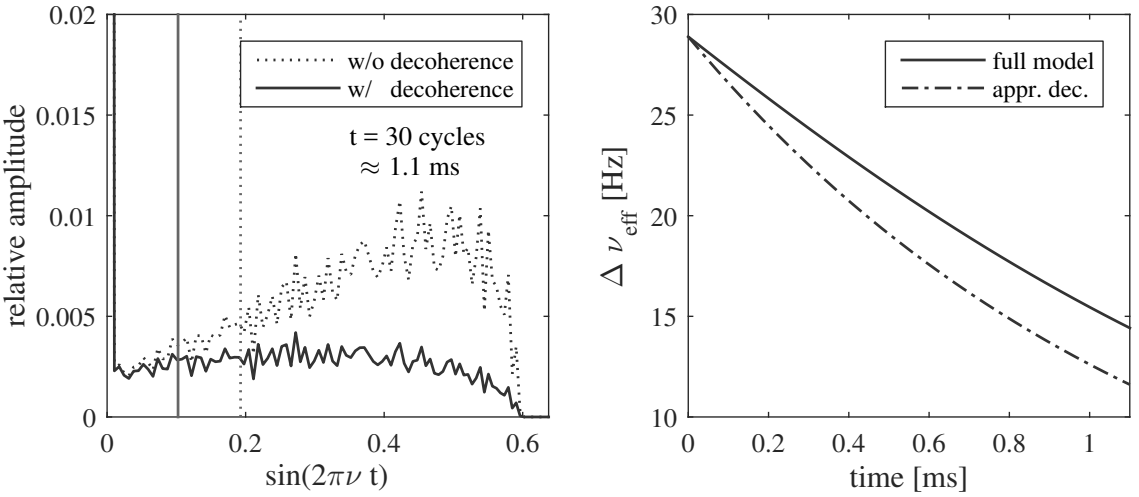

Figure 5.9: Time evolution of the signal value for a ^{6}Li cloud. On the left the impact of decoherence on the signal distribution is shown. The corresponding mean values are depicted as vertical bars. On the right the time evolution of the effective frequency shift is depicted (line). It is approximated by a simple exponential model (dash dotted line, Eq. (5.67)).

sodium density for immersed lithium atoms:

$$\bar{n}_{\mathrm{Na}}^{\mathrm{im}} = \frac{\int_{\mathrm{BEC}} n_{\mathrm{Li}}(\vec{r}) n_{\mathrm{Na}}(\vec{r}) \mathrm{d}V}{\int_{\mathrm{BEC}} n_{\mathrm{Li}}(\vec{r}) \mathrm{d}V} = \frac{\int_{\mathrm{BEC}} n_{\mathrm{Li}}(\vec{r}) n_{\mathrm{Na}}(\vec{r}) \mathrm{d}V}{\eta_{\mathrm{im}} N_{\mathrm{Li}}}, \tag{5.66}$$

$$\Delta\nu_{\mathrm{eff}}(t) = \Delta\nu_{\mathrm{eff}}(t=0) \cdot \exp(-\Gamma^{\mathrm{im}} t), \tag{5.67}$$

where Γ^{im} can be calculated from $\bar{n}_{\mathrm{Na}}^{\mathrm{im}}$ by Eq. (5.61). The origin of the mismatch lies in the structure of the spectrum. We can see in Fig. 5.10 that this decoherence approach fits the amplitude decay much better (dash-dotted line in the left panel). But in the description of the time evolution of the amplitude we encounter the problem of this static model: Due to its lack of lithium motion only atoms inside the BEC decay on a short timescale. Half of the lithium atoms are outside the BEC, interacting with the low thermal sodium density and hence exhibiting an extremely slow collision rate. The signature of this situation is a clear bimodal decay that is not observed in the experiment. Nevertheless no lithium motion is included here as the short time behavior is well captured. For long times the static model underestimates the frequency and overestimates the amplitude. In Eq. (3.38) an effective density $\bar{n}_{\mathrm{Na}}$ averaging over the whole cloud is introduced:

$$\bar{n}_{\mathrm{Na}} = \frac{\int n_{\mathrm{Li}}(\vec{r}) n_{\mathrm{Na}}(\vec{r}) \mathrm{d}V}{\int n_{\mathrm{Li}}(\vec{r}) \mathrm{d}V} = \frac{\int_{\mathrm{BEC}} n_{\mathrm{Li}}(\vec{r}) n_{\mathrm{Na}}(\vec{r}) \mathrm{d}V}{N_{\mathrm{Li}}}. \tag{5.68}$$

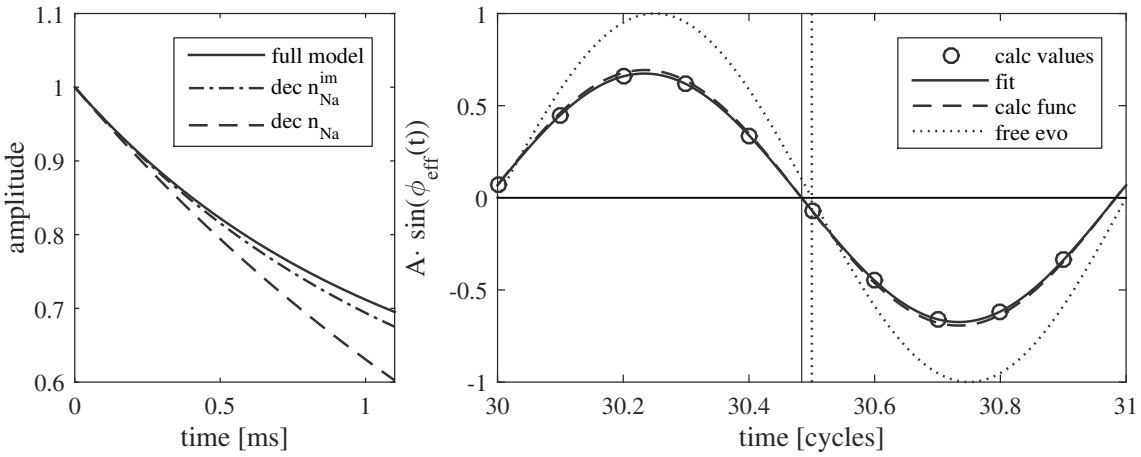

Figure 5.10: Time evolution of the signal amplitude for a ^{6}Li cloud (left). The amplitude of the introduced model (Eq. (5.63), line) is approximated by Eq. (5.70) (dash dotted line) and Eq. (5.69) (dashed line). On the right, 10 signal values at 1.1 ms are calculated by use of Eq. (5.62) (circles). As dephasing is negligible, the model Eq. (5.65) captures the fringe well, revealing a insignificant difference between the calculated function (dashed line) to the fit (line). In the experiment this fringe has to be compared to the free evolution (dotted line).

It enables us to describe the amplitude time evolution of the whole cloud as a monoexponential decay:

$$A(t) = A(t=0) \cdot \exp(-\Gamma t), \tag{5.69}$$

where again Γ can be calculated from $\bar{n}_{\mathrm{Na}}$ by Eq. (5.61). This approach has been used in [48] and is plotted as a dashed line. Although its decay constant is smaller (lower effective density) than the two section model, the absolute decay itself is quicker, as it drops to zero and does not just affect the immersed lithium part. The dash dotted line describes the situation where the amplitude of the immersed lithium atoms η_{im} decays at Γ^{im}, the part outside the BEC does not decay at all:

$$A(t) = A(t=0)\left(\eta_{\mathrm{im}} \exp(\Gamma^{\mathrm{im}} t) + (1-\eta_{\mathrm{im}})\right). \tag{5.70}$$

It approaches the full model, but exhibits an obvious discrepancy for long times.
As a last step we test the validity of the model derived in the beginning of this section. It is susceptible to dephasing and has to be used carefully. Therefore an exemplary fringe at the longest experimentally employed evolution time of 1.1 ms is displayed on the right panel of Fig. 5.10. The calculated values can be well described by a sine function. The fit reveals no significant difference to the plotted function based on Eq. (5.65) and Eq. (5.64). The ideal fringe obtained after a free evolution

is plotted as a dotted line. The experimental challenge is to differentiate between the vertical bars (line and dotted). As for ^{6}Li the background modulation effect is dominant, the experimentally measured phase shifts between the fringes are larger, but only a small part is due to the phononic coupling. The plotted and discussed situation neglects the sodium BEC modulation by the lattice, its wavelength is set to lithium resonance.

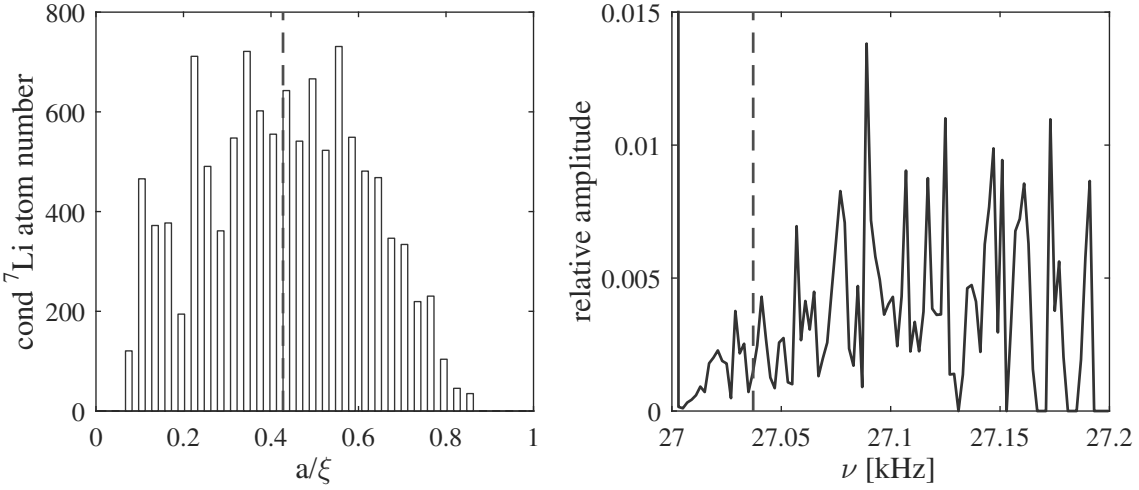

Figure 5.11: The ^{7}Li BEC probes only the surface of the sodium BEC. The left panel shows a histogram of the probed sodium BEC healing length. Taking $n^{2D}_{\text{Li, BEC}}$ into account it translates into a broad distribution of frequency shifts. In the right panel the peak at $\nu_0 = 27\,\text{kHz}$ is cut off for better visualization. Mean values are indicated by vertical bars.

The probed sodium BEC healing length ξ and corresponding frequency distributions for ^{7}Li differ from the ones for fermions. As explained in the previous sections only the condensed impurities contribute to the frequency shift. Therefore, the left panel of Fig. 5.11 displays the sodium BEC a/ξ values, which are probed by the condensed impurities. The sodium BEC itself is almost the same as in the fermionic case, so values of up to $a/\xi = 1.22$ are realized. Due to interspecies repulsion the highest probed values are 0.85. Still, when converting the probed sodium and lithium density into frequencies, values about twice as high as in case of ^{6}Li are realized. The reason is the bosonic enhancement. Again most of the atoms (66 %) contribute to ν_0. Here the reason is twofold: the condensate fraction is $\eta_{\text{CF}} = 0.57$ and the immersion of the BEC is 0.6. A broad spectrum promotes dephasing, as the time evolution differs strongly.

In Fig. 5.12 the time evolution for the bosonic impurity case is studied. At the longest experimentally employed evolution time of 1.1 ms the distribution of $\sin(\phi)$ stretches almost up to 1, corresponding to a phase difference of $\pi/2$ between the

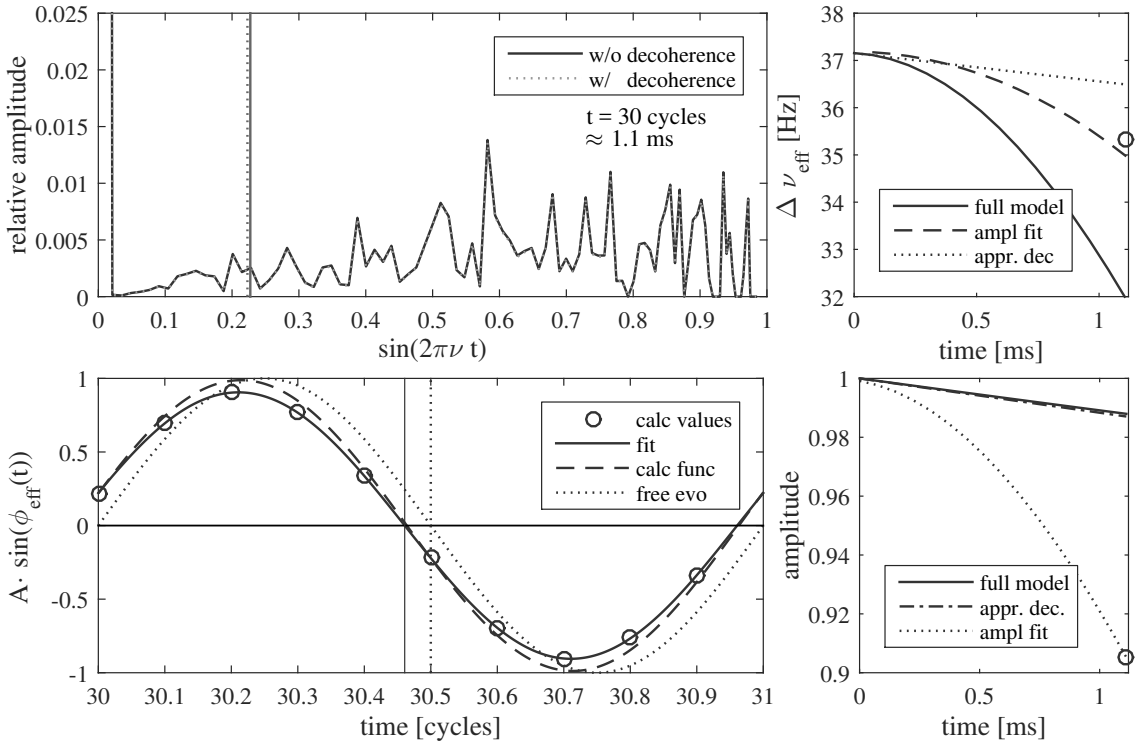

Figure 5.12: Time evolution of the signal for a ^{7}Li cloud. The values of $\sin(\phi)$ approach unity for long evolution times. Therefore dephasing becomes important. In the lower left panel 10 points are calculated using Eq. (5.62). Their fit differs from a modeled function using Eq. (5.63) as the amplitude is not captured correctly in case of dephasing. This is highlighted by the lower right panel, where the analytic expression (line) and its approximation Eq. (5.70) (dash dotted line) deviate from the fitted amplitudes (dotted line). As the amplitude is important for the frequency derivation if the phase is derived from a function value except zero, in the upper right graph the calculated values (Eq. (5.65), line) contradict the frequencies derived using the fitted amplitude (dashed line). They agree with the phase of the fit to the sine fringe (circle). For a comparison to the effect of decoherence the prediction of Eq. (5.67) is depicted (dotted line).

atoms experiencing the strongest shift and the atoms outside the sodium BEC. Because of the sinusoidal dependence the phase distribution corresponding to high frequencies is compressed compared to the spectrum in Fig. 5.11. The fringe at 1.1 ms evolution time (lower left) illustrates the failure of the model due to dephasing. Decoherence is low due to the small interaction ($\Gamma \propto a_{\mathrm{IB}}^2$) and the low sodium BEC density probed. The model (dashed line) takes only decoherence into account and

overestimates the accurate amplitude values (circles). The zero of the fringe is correct, but the effective frequency is calculated from the absolute value at the former zero (here 30 cycles). This works out only if the correct fringe amplitude is considered. If this is not the case, the energy shift is underestimated (black line upper right). If the amplitude is determined by a fit, proper values can be derived (dashed line). The effective frequency derived from the fringe fit is depicted as a circle. The dotted line indicates the time evolution of the shift assuming only decoherence (see Eq. (5.67)). On the lower right panel amplitudes calculated by Eq. (5.63) and Eq. (5.70) are plotted as well as the fitted values. The discrepancy is easily visible. In conclusion, for large phases the fringe has to be calculated at several points and fitted.

The model can be extended to include the sodium BEC modulation by the lattice (see section 5.4). Every lithium atom inside the BEC gets an additional $\Delta\omega_{\mathrm{latt}}$. For bosonic impurities the fraction experiencing δ_{latt} is different to the portion experiencing the self-energy shift as all lithium atoms within the sodium BEC see a potential modification due to the sodium BEC modulation by the lattice, but only condensed lithium atoms within the sodium BEC are considered to distort the sodium BEC efficiently. In sum, high effective frequency shifts with noticeable dephasing are obtained for fermionic as well as bosonic impurities. Hence for the theoretical predictions in section 6.3 both scenarios are analyzed by fitting of the calculated fringes, which we have found to be robust against dephasing effects.

6 Spectroscopy of Impurities in a BEC

In this chapter we present our Ramsey type spectroscopy measurements of lithium impurities immersed into a sodium BEC. First the data representation is explained. Next measurements on fermionic and subsequently on bosonic impurities are shown. These experimental results are compared to theoretical expectations.

The Ramsey sequence determines the gap between the two lowest external states of the lattice (trapping frequency ω_0). The background-induced gap modification ($\Delta\omega$) is isolated by performing the pulse sequence with and without sodium BEC. The two obtained fringes exhibit a phase difference of ϕ. It is handy to characterize the change of the energy gap by the dimensionless quantity (see Eq. (4.2)):

$$\delta = \frac{\Delta\omega}{\omega_0} = \frac{\phi}{2\pi \cdot \#\text{cycles}}, \tag{6.1}$$

where the number of cycles refers to the periods of the harmonic oscillator (ω_0) for the whole duration of the Ramsey scheme, including the pulses. More information on the experimental technique can be found in subsection 4.4.2.
We identified two different mechanisms how the background modifies the impurity potential: off-resonant modulation of the sodium BEC through the lattice and the self-energy shift (see chapter 5). We extract the self-energy shift by interpolating to a resonant lattice for lithium, corresponding to no sodium BEC modulation. In Eq. (5.56) the lattice effect is given to be proportional to the ratio $V_\mathrm{B}/V_\mathrm{I}$. This ratio is, besides some constants, solely determined by the wavelength creating the potential. Therefore the most obvious way of analyzing the data is to plot δ over the lattice wavelength. Due to experimental necessities (consistent band structure for Li) we have to keep the potential height for lithium constant. In order to scan $V_\mathrm{B}/V_\mathrm{I}$ we employ red and blue detuned lattices with a detuning of about $\pm 0.5\,\mathrm{nm}$ and $\pm 1\,\mathrm{nm}$, respectively. To adapt the lithium potential, we adjust the lattice light intensity to $0.7\,\mathrm{V}$ and $1.4\,\mathrm{V}$ respectively on the controlling photo diode (power of $44\,\mathrm{mW\,V^{-1}}$ per beam). Thereby the absolute value of V_I is kept constant and V_B and the relative sign is scanned. In first approximation V_B is proportional to the light intensity, as the detuning is large. The ratio $V_\mathrm{B}/V_\mathrm{I}$ has been calculated from the employed wave length and atomic properties, see Eq. (3.1).

6.1 Fermionic Impurities

For fermions, the dominant background-induced effect is via the sodium BEC modulation through the lattice. Therefore we first show the dependence of the relative frequency changes δ on the evolution time and the lattice potential ratio V_B/V_I (see Fig. 6.1). Further, the absolute fringe amplitudes are depicted as they contain information about decoherence and dephasing. As asymmetric Ramsey pulses ($\neq \pi/2$) influence the amplitudes as well, these scans (see Fig. 6.4) are excluded from the plots containing absolute amplitudes. As we will see later (Fig. 6.3), the lithium atom number for these plots has to be post-selected. The median lithium atom number of the plotted scans is between $4 \cdot 10^3$ and $11 \cdot 10^3$. Time is given in multiples of the oscillation period, the lattice frequency is about 27 kHz, corresponding to a time scale of 37 µs.

In the lowest row of Fig. 6.4 the offset and slope of the linear fits to the four datasets are plotted. The error bars correspond to the 68 % confidence level. Analyzing the δ-values over time we cannot retrieve a distinct time evolution. The data shows high uncertainties and at the last time step dephasing gets important (see next paragraph). If any time evolution of δ can be conjectured, the tendency hints at a decrease in time. To our knowledge there are no time-dependent effects, but decoherence affects only the immersed part and therefore causes a time-dependent total δ value. Thus, these results are in agreement with the assumption that we are studying a constant frequency shift due to the background interaction. Therefore it is natural to merge all data taken at different times and to benefit from the reduced uncertainty due to a higher number of measurements.

The highest possible fringe amplitude is 0.5, see Eq. (5.57). In our setup we typically reach 0.3 to 0.4, see subsection 4.4.1 for more information. The marker showing the amplitude values are slightly displaced for presentation. For short times the amplitudes with (A_{wB}) and without (A_{nB}) background are very similar. For longer times, the decoherence gets stronger, but even the amplitude without background is reduced due to dephasing of different lattice sites.
The values at high potential ratios decrease more than the center ones due to the background interaction. This can be understood by a second dephasing mechanism: differentiating between immersed lithium atoms and atoms outside the sodium BEC, we get large phase differences for long times. Here (at 30 cycles and $V_B/V_I = \pm 0.012$) the total value is $\phi = 0.2\,\pi$. Assuming a typical immersion of $\eta_{im} = 0.4$, the phase difference of immersed to unaffected atoms is $0.2/0.4\,\pi = 0.5\,\pi$. At π the amplitude would be decreased to 0.2 times the initial value and the observed phase would be zero. Hence at 30 cycles and strong sodium modulation this dephasing mechanism gets important, visible by an amplitude reduction with background.

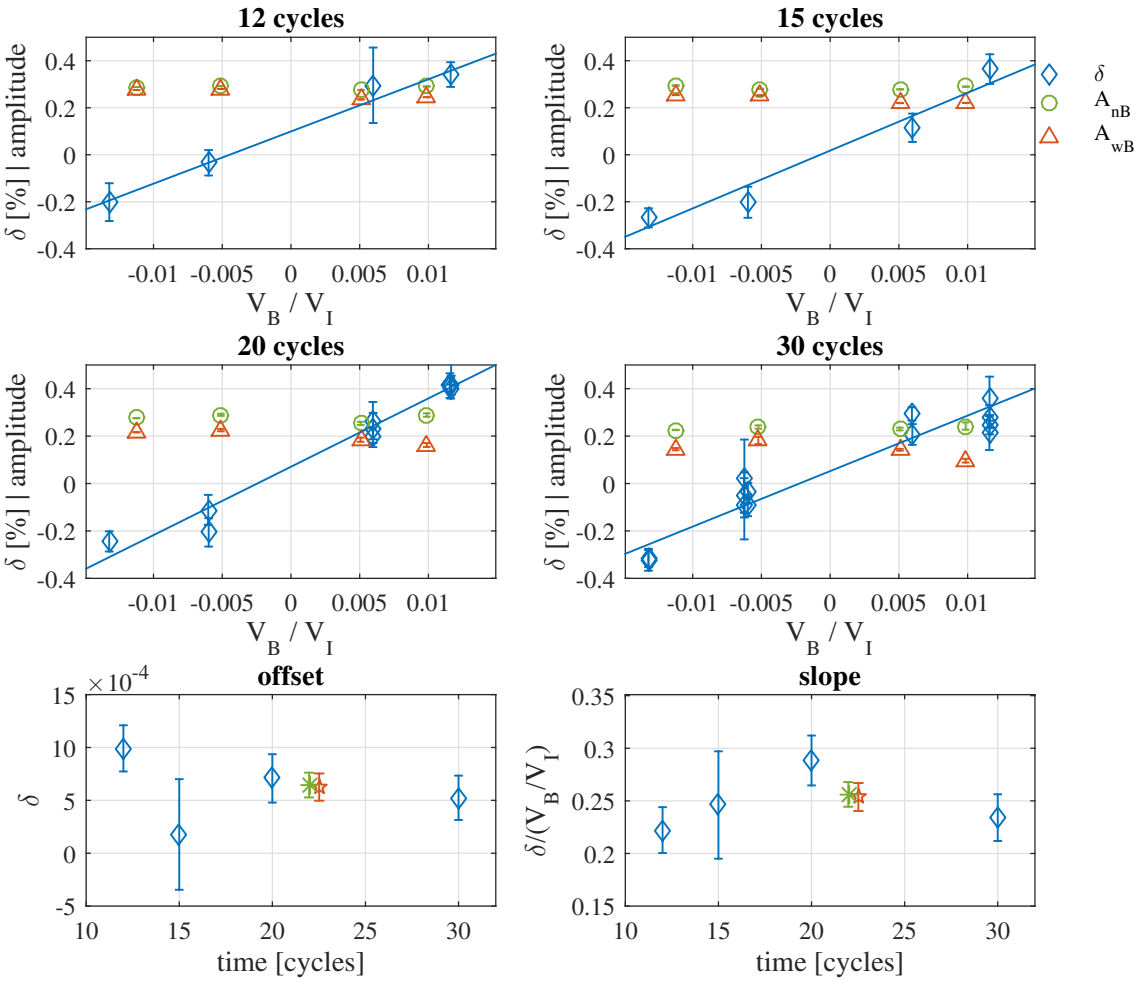

Figure 6.1: Time evolution of background-induced effects for ^{6}Li atoms. The upper four plots depict δ (diamond) along with a linear fit and the amplitudes of the fringes over time as a function of $V_\mathrm{B}/V_\mathrm{I}$. The fringe amplitude without background $\mathrm{A_{nB}}$ is depicted by a circle, with background $\mathrm{A_{wB}}$ by a triangle. The lower part summarizes the linear fits. The red pentagram is a fit to all above shown data points at once, the green star includes even more data points with an unbalanced excitation.

Another interesting aspect is the difference between red and blue detuning regarding the overlap. At positive potential ratios the decoherence seems to be stronger than at negative ones. At large $V_\mathrm{B}/V_\mathrm{I}$ the lattice is at $\lambda \approx 672\,\mathrm{nm}$ and thus is red detuned for both, sodium and lithium. The sodium modulation is rather strong and the effective density is about 50 % higher than at $\lambda = 670\,\mathrm{nm}$ (see Fig. 3.9). The stronger decoherence decreases the observed total δ value, as the unaffected part does not

undergo decoherence. This might contribute to the surprisingly small δ-value at 30 cycles and $U = 1.44\,\mathrm{V}$.

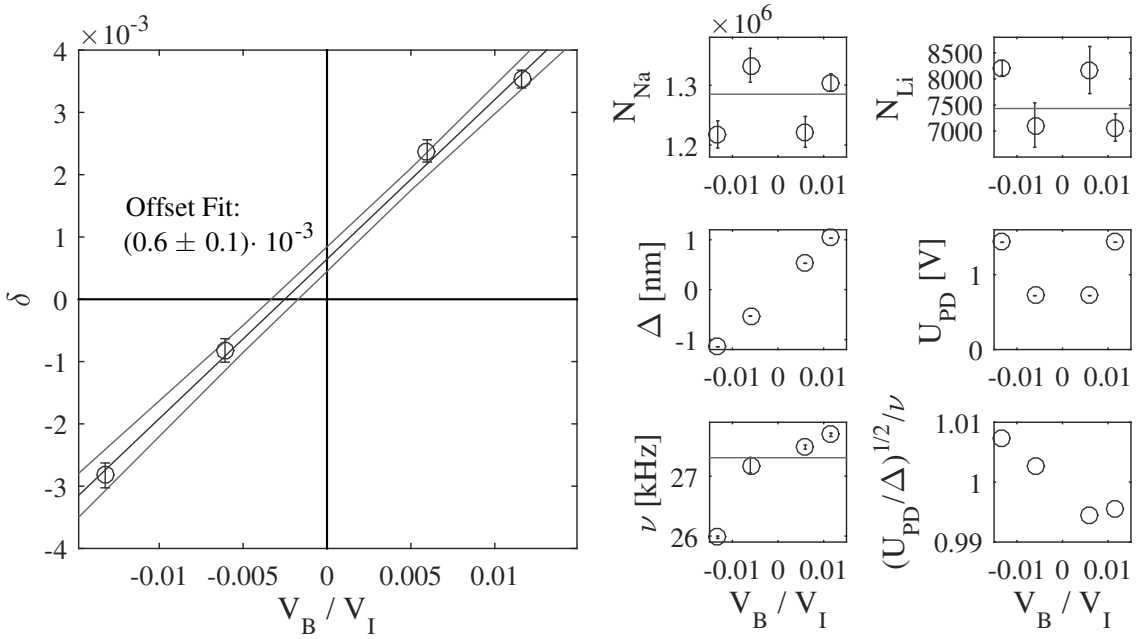

Figure 6.2: Summary of the background-induced energy shift δ for fermions (left). Outer lines indicate the 1-σ trust region of the fit. On the right hand side the corresponding relevant experimental parameters are displayed. N_{Na} and N_{Li} describe the atom numbers, the detuning of the lattice for lithium is denoted by Δ, U_{PD} is the voltage of the light intensity controlling photo diode, $\nu = \omega_0/2\pi$ is the trapping frequency and the bottom-right graph is a relative measure for the resonance condition (see Fig. 4.3).

To reduce the statistical uncertainties, in Fig. 6.2 all ^{6}Li scans at adequate atom number (median between $4 \cdot 10^3$ and $11 \cdot 10^3$) are combined, including scans at asymmetric excitation, as we do not observe any imbalance dependence for fermions (see Fig. 6.4). The weighted means of the δ values are plotted over the lattice potential ratio $V_{\mathrm{B}}/V_{\mathrm{I}}$ which is about 1 %. The data points show a linear behavior which is fitted. The fit line displays a clear offset at the resonance condition for lithium. This offset corresponds to an energy shift of $\Delta E/\hbar = 2\pi \cdot (18 \pm 3)\mathrm{Hz}$. Here the uncertainty corresponds to the 1-σ trust region of the fit. For completeness the right side displays important experimental parameters. The mean values of all scans are plotted as a horizontal line. The atom numbers (N_{Na}, N_{Li}) do not show any relevant trend which certifies that the effect is not due to unwanted fluctuations. The sodium atom numbers are underestimated by a factor of 1.6 due to in-situ imaging. The lattice detuning to lithium resonance is labeled Δ, the controlling photo diode

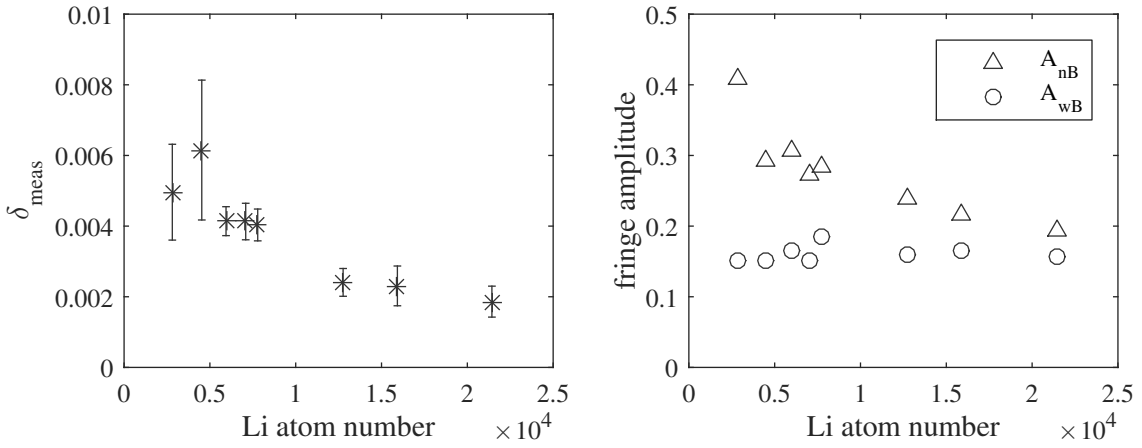

Figure 6.3: Dependence of δ (stars) and fringe amplitudes on the ^{6}Li atom number. The amplitude without BEC (A_{nB}) is denoted by triangles, in case of a BEC (A_{wB}) by circles. Displayed scans have symmetric Ramsey pulses, 20 cycles of total evolution time and $U_{PD} = 1.4\,V$. For small atom numbers a good overlap is revealed by large δ values and stronger decoherence in the presence of sodium background.

voltage U_{PD}. The trapping frequency is indicated by $\nu = \omega_0/2\pi$. The lower right side depicts a measure how resonant the lithium lattice is (see Fig. 4.3).

In the last two plots only measurements for a certain range of lithium atom numbers were displayed. In Fig. 6.3 we can see why this is necessary. Both background-induced effects depend on the overlap. As we have not performed systematic scans of V_B/V_I for several lithium atom numbers, we cannot differentiate between the two effects and therefore the displayed data is without correction for lattice modulation of the BEC. The measured sodium atom number is decreased from $1.4 \cdot 10^6$ to $0.9 \cdot 10^6$ with rising lithium atom number. For vanishing lithium atom numbers, the measurement uncertainty increases strongly, but the values for δ and the overlap are very high. This can be seen on the ratio of amplitudes on the right of Fig. 6.3, showing strong decoherence. Larger ^{6}Li atom numbers result in smaller values for δ, as less lithium atoms are in contact with the sodium BEC. Furthermore larger lithium clouds occupy many lattice sites, which causes dephasing due to varying lattice depths at different lattice sites. This reduces the amplitude values A_{nB}. The amplitude A_{wB} remains almost constant, as the amplitude reduction by dephasing is compensated for by diminished decoherence due to reduced overlap.

Our last systematic study for fermions examines the dependence of δ on the population of states during the free evolution time. We varied the number of excitation cycles of the first Ramsey pulse to prepare an imbalanced superposition of ground and excited

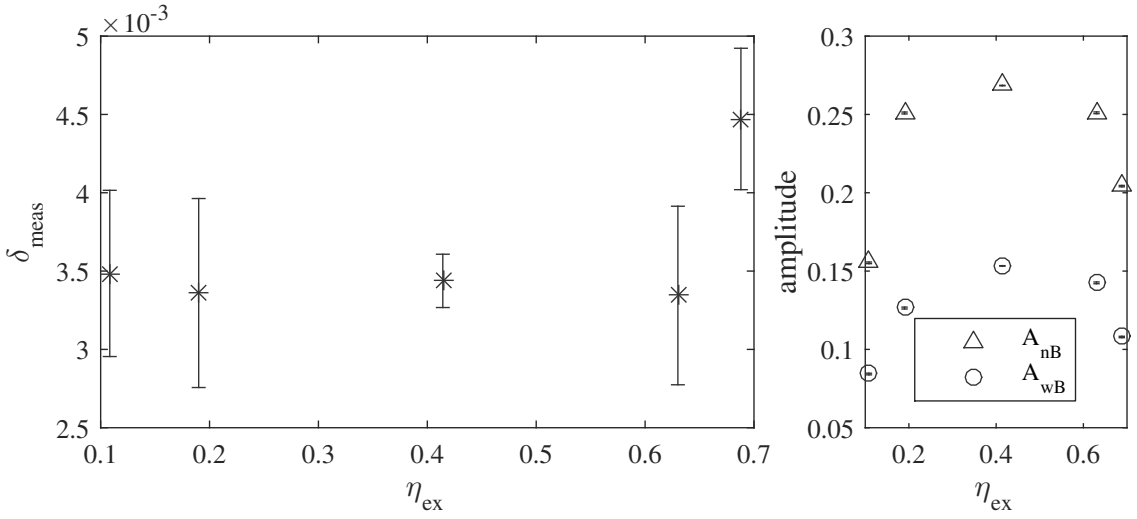

Figure 6.4: Dependence of δ on the excited fraction η_{ex} during free evolution for ^{6}Li. No trend is observable. On the right the corresponding amplitude values are depicted. the case without BEC (A_{nB}) is depicted by triangles, the amplitude for scans with BEC (A_{wB}) by circles. The amplitudes are reduced for strong imbalances. As for the *delta* values the uncertainty weighted mean of the fits is calculated for the amplitudes.

state. The second pulse always consists of 5 cycles ($\widehat{=}\pi/2$). The number of cycles is converted into a fraction of excited atoms η_{ex} by the Rabi fringe in subsection 4.4.1. Fig. 6.4 displays the results. These scans are performed at $U_{\mathrm{PD}} = 1.4\,\mathrm{V}$ and have not been corrected for the lattice effect, so raw measurement data is shown. The median lithium atom number of the displayed scans is between $4 \cdot 10^3$ and $11 \cdot 10^3$. Within the uncertainties no systematic trend with the excited fraction is visible. In the right panel the amplitudes are plotted. Obviously the fringe contrast is reduced in asymmetric pulse schemes.

6.2 Bosonic Impurities

We studied bosonic lithium in two typical scenarios, condensed and thermal. Bose-Einstein condensation in this species is experimentally controlled by the lithium atom number and temperature (see section 2.6). The corresponding density distributions are described in subsection 3.3.4. As highlighted in chapter 5, thermal bosonic impurities show a similar behavior to ^{6}Li, but have different atomic properties. The main distinction is the repulsive and weaker interaction between sodium and ^{7}Li. It results in negligible decoherence on the time scales of our experiments.

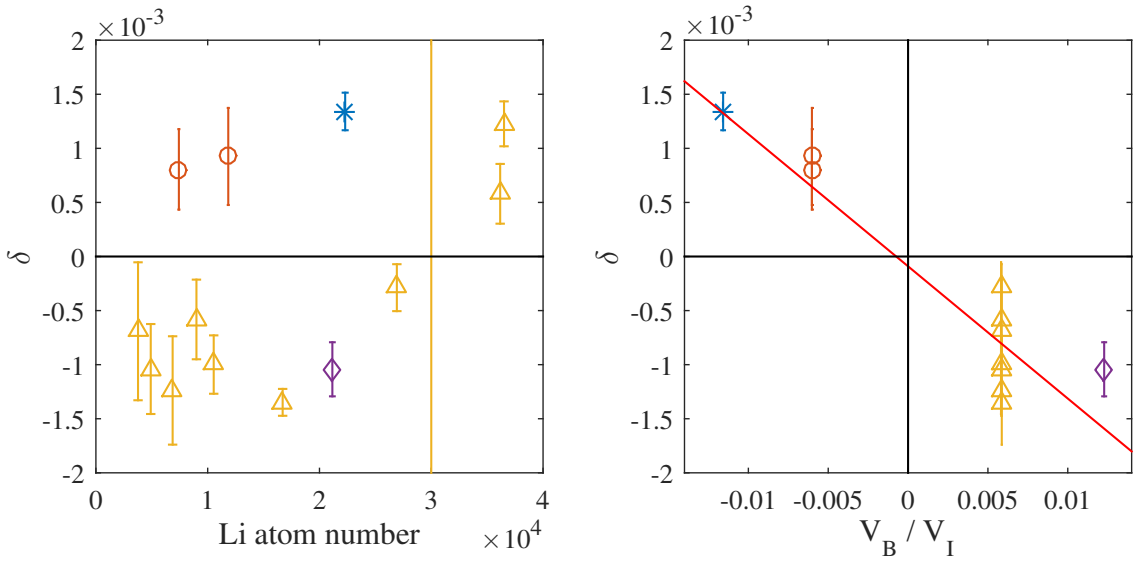

Figure 6.5: Summary of results for thermal ^{7}Li. On the left δ values for different $V_\mathrm{B}/V_\mathrm{I}$ are plotted over the atom number, showing no dependence until condensation sets in, displayed by a yellow vertical line. In the right panel only the scans with median atom number below $3 \cdot 10^4$ atoms are plotted, for which the lithium atoms are still thermal. The δ values of these thermal scans are depicted in dependence of the ratio $V_\mathrm{B}/V_\mathrm{I}$.

All experiments with bosonic impurities are performed with a total duration of 1.1 ms. In Fig. 6.5 all measurement values for the thermal ^{7}Li scenario are depicted. On the left side the relative background-induced frequency change δ is plotted over the lithium atom number. The scans were performed at different values of $V_\mathrm{B}/V_\mathrm{I}$, which are indicated by the different colors (see right panel). For $\lambda = 670.485\,\mathrm{nm}$ (orange triangles) measurements at many atom numbers have been performed. For small lithium atom numbers the uncertainty increases due to the reduced absorption signal. For larger atom numbers the δ values increase, as Bose-Einstein condensation of ^{7}Li sets in. Therefore, for the study of the potential effect on the right only measurement data with scans below $3 \cdot 10^4$ atoms are shown. As for the fermionic case we get a linear dependence with a rather large uncertainty of data points. The slope of the fit can be used to correct for the potential effect. The δ over N plot with subtracted potential effect is shown in Fig. 6.6. This figure includes the amplitudes as well. The potential effect is compared to the condensed case in Fig. 6.7.

In the condensed case we observe a strong dependence on the sodium BEC modulation by the lattice and the lithium atom number. In order to study these effects separately, the δ values have to be corrected for these parameters. This cannot be done independently, as there is no dataset scanning only one of the parameters. Therefore

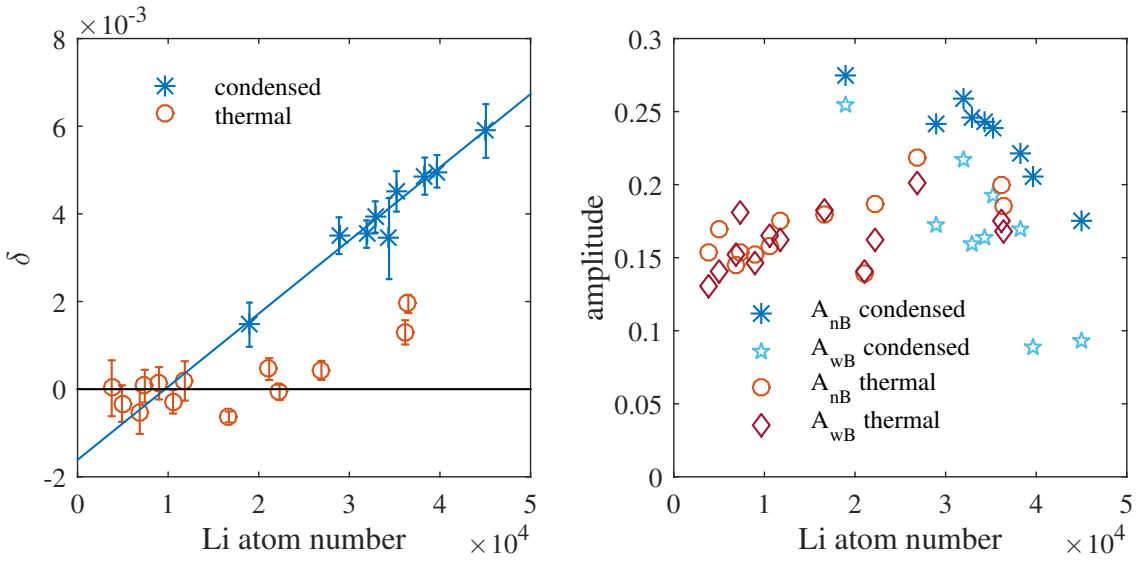

Figure 6.6: Dependence of δ on the atom number. For the scenario called thermal (circles), values increase due to condensation when reaching lithium atom numbers of more than $3 \cdot 10^4$. Condensed impurities (stars) show a linear behavior over the whole experimentally tested range. On the right the fringe amplitudes are depicted where the index nB denotes no background and wB with background.

the linear fitting of the atom number and for $V_\mathrm{B}/V_\mathrm{I}$ is done iteratively. First the δ/N dataset is fitted linearly. It allows the scaling of δ for every data point to $34 \cdot 10^3$ lithium atoms. These values are then plotted over $V_\mathrm{B}/V_\mathrm{I}$ and fitted linearly as well. In a next step the δ values at lithium resonance ($U_\mathrm{PD} = 0$) can be calculated. They are plotted over the lithium atom number and fitted. The procedure quickly converges. In the next three plots the data for condensed impurities has been corrected like this.

In Fig. 6.6 all population balanced scans for ^{7}Li are shown. The data points are interpolated to lithium resonance. Over the range of lithium atom numbers δ for the condensed case behaves strictly linear. It is not a line through the origin as condensation sets in above a certain atom number. For ^{7}Li solely condensed atoms exhibit a considerable non-zero δ. In the blue scenario, where the high field hybrid trap has been deployed, the fit line crosses the x-axis at 10^4 atoms, where the formation of a BEC starts. In the red setup, without the high field hybrid trap and therefore much higher sample temperature, δ values get significantly positive at about $3 \cdot 10^4$ lithium atoms.
The study of the amplitudes on the right is very insightful. For small atom numbers the thermal samples reveal no decoherence, as the fringe amplitude with and without

sodium background is the same. For increasing atom number the amplitude tends to get larger, as condensation results in smaller clouds and the occupation of less lattice sites. The occupation of few lattice sites reduces dephasing, as every lattice site has a slightly different depth. For the condensed data a difference between with and without sodium BEC is increasing with N_{Li} but should not be attributed to decoherence. The maximum amplitude (for small N_{Li}) is very high, as only a few lattice sites are populated. With increasing Lithium atom number the energy difference increases as well. This is only true for lithium atoms immersed into the sodium BEC. Parts of the lithium cloud do not probe the BEC and do not accumulate a different phase than the one by the trap (ω_0). This is another reason for dephasing, causing the fringe amplitude in case of background to shrink. There are two types of dephasing, one due to inhomogeneity of the standing light wave intensity and one due to inhomogeneity of the sodium BEC density which is probed by the lithium atoms. No decoherence can be measured and is expected due to the small intra-species interaction.

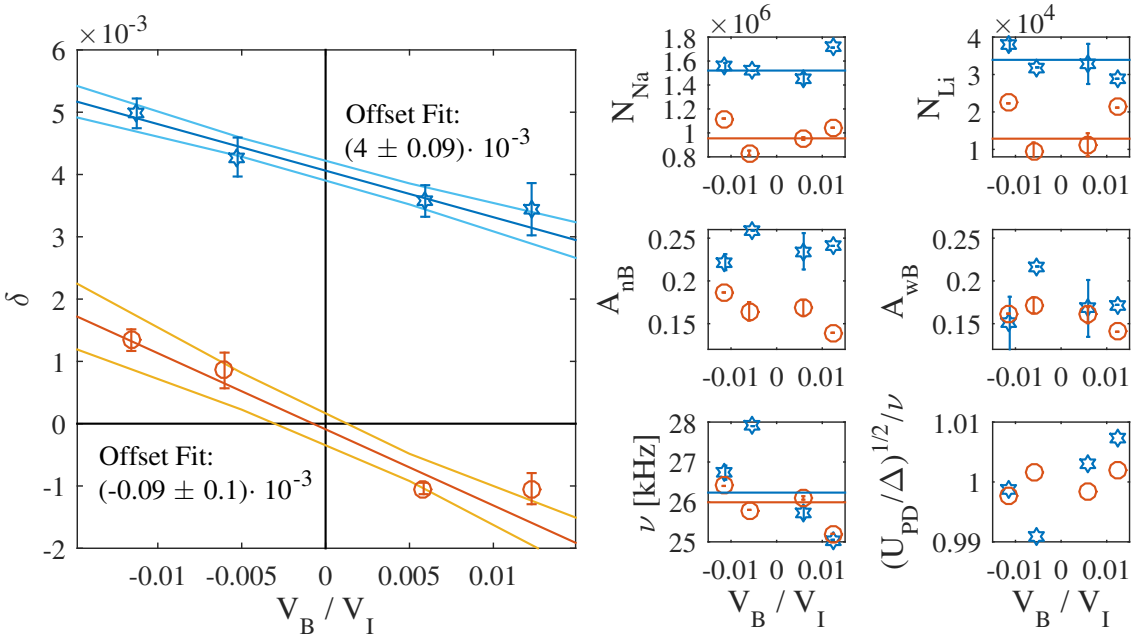

Figure 6.7: The lattice potential effect for bosons. Condensed impurities (blue) are compared to thermal ones (red). Bothe are linearly fitted and the 68 % confidence area is plotted as well. No shift at lithium resonance can be extrapolated in the thermal case but a strong one in case of condensation. On the right experimental parameters are summarized, see Fig. 6.2 for a description of the parameters.

Fig. 6.7 allows the determination of the self-energy for bosonic impurities. The condensed δ values are interpolated to $34 \cdot 10^3$ lithium atoms. The thermal lithium

sample does not exhibit an energy shift, in accordance with the theoretical expectations. The condensed cloud shows an energy shift of $\Delta E/\hbar = 2\pi \cdot (107 \pm 2)$Hz. All plotted and mentioned uncertainties correspond to 1-σ confidence intervals. The slope of the fit in the condensed case is reduced compared to the thermal one, as a BEC can evade the repulsive sodium BEC more easily when the overlap is changed due to potential changes. On the right side experimental parameters are shown, mean values are given as horizontal lines. The same reasoning as given in the previous paragraph is valid for the explanation of the fringe amplitudes. Several types of dephasing occur.

Fig. 6.8 shows agreement with theory, depending only weakly on the difficult to calculate overlap (see Fig. 5.6). We expect ground and excited state to shift proportional to their population. In our parameter regime the population of the ground state causes a negligible energy shift of the excited state and vice versa, see section 5.2 for details. Due to the higher density of the ground state, its shift is stronger. This can be compensated by a higher population in the excited state, leading to no effective energy shift. The corresponding experimental data is shown in Fig. 6.8. All δ values are interpolated to $N_{\mathrm{Li}} = 34 \cdot 10^3$ and $V_{\mathrm{B}}/V_{\mathrm{I}} = 0$. In theory a linear dependence of the energy shift on the population of states is expected and at 85 % of the impurity atoms in the excited state the shifts of ground and excited state cancel out. The challenge is to map our experiment onto this two-level theory. The reason is twofold: a part of the atoms in highly occupied states are attributed to other states due to detection noise. Another reason is that in the experiment we cannot completely neglect the 3$^{\mathrm{rd}}$ band. The potential is rather harmonic and the coupling strength is quite high. Therefore the 3$^{\mathrm{rd}}$ band gets populated. This is shown in the lower left panel of the figure. At the point of highest excitation into the 2nd band 11 % of atoms are detected in the 3rd band and 14 % of the atoms are assigned to the 1st band, see subsection 4.4.1 for more information. In order to account for this problem, on the right panel the same data is plotted, but the fraction of excited atoms η_{ex} is renormalized to $\eta_{\mathrm{ex}} = \eta_2/(\eta_1 + \eta_2)$ (see lower right panel). This shifts the data point of highest excitation from $\eta_{\mathrm{ex}} = 0.69$ to $\eta_{\mathrm{ex}} = 0.76$. The deployed number of excitation cycles are encircled in blue. The light red line is a linear fit to the data points and the dark red dashed line is a fit with the theoretically expected x-axis crossing at $\eta_{\mathrm{ex}} = 0.85$. The free fit crosses the x-axis at 0.81 ± 0.07 (red bar) giving good agreement with theory.
The cross interaction between the population of states is negligible, implying that a population of one state does not influence the other one. Thus, we can deduce the energy shift of the ground state for $34 \cdot 10^3$ ^{7}Li atoms to be $\Delta E_0/\hbar = 2\pi \cdot (-230 \pm 10)$Hz and the excited state shift to be $\Delta E_1/\hbar = 2\pi \cdot (-53 \pm 30)$Hz, both plotted as red bars. The fact that the ground state shifts more than four times stronger than the excited state emphasizes the problem of the population assignment: In a two level system atoms that are not in the excited state are in the ground state and are expected to

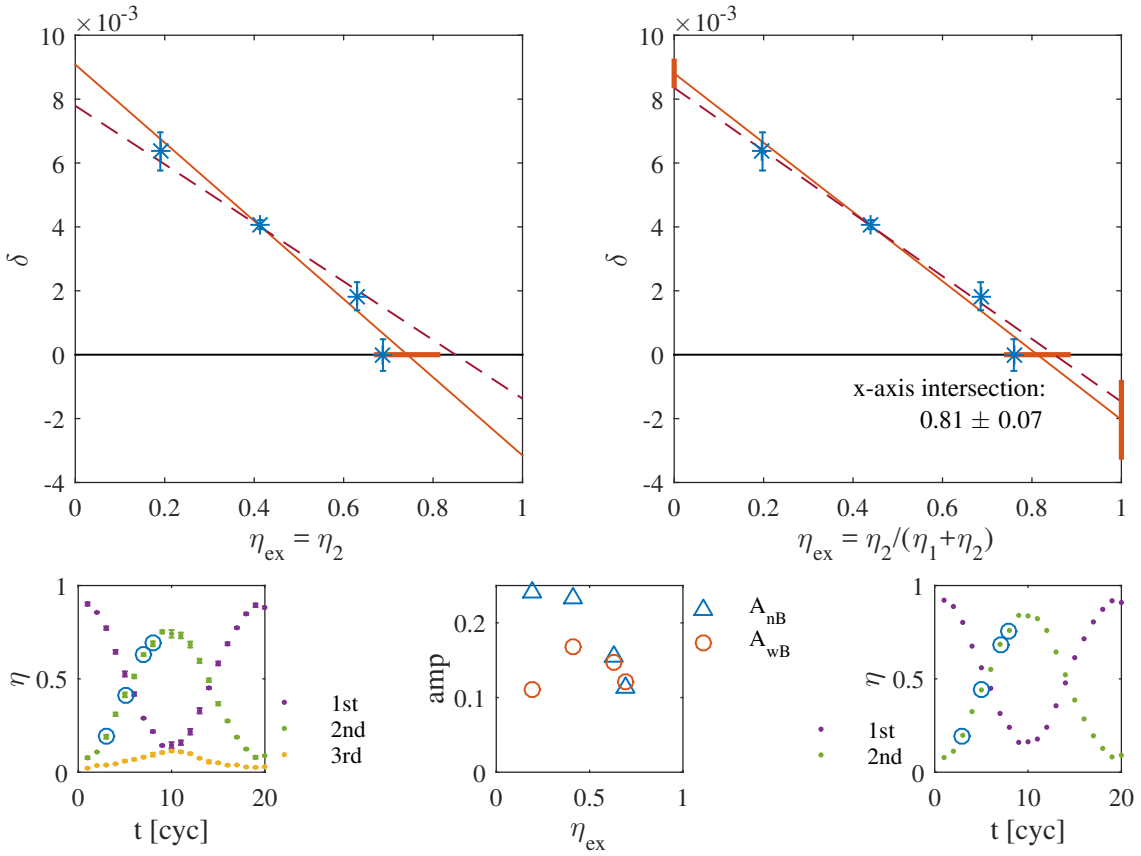

Figure 6.8: Effect of population imbalance during free evolution on the measured energy shift. On the left side the lithium population is distributed on three trap levels like we detect it in our experiment. Theory considers two levels only, therefore on the right the plot is repeated with a renormalized excited fraction η_{ex}. The underlying calibration Rabi cycles are plotted below the panels, experimentally employed pulses are encircled. In both cases the measured δ values (stars) are fitted linearly (line) and by a line with a fixed zero predicted from theory (dashed). The 68 % confidence interval of the free fit at $\eta_{ex} = 0$ and 1 is depicted by a red bar as well as the zero of the fit line. In the center the measured fringe amplitudes are plotted with (A_{wB}) and without (A_{nB}) background.

cause a strong shift. But the atoms are in the 3rd band yielding a negligible shift. This is why the renormalization to a two level system is justified and necessary.
In the central lower part the fringe amplitudes as a function of η_{ex} are shown. Again we see that without background we have high fringe amplitudes and for strong energy shifts the amplitudes with background are reduced. A new characteristic appears here: for high η_{ex} the amplitude is small even without background. This

feature is caused by Li-Li scattering from the 2nd band to the 1st and 3rd bands, see subsection 4.5.2.

6.3 Comparison of Experiment to Theory

Our theoretical considerations are based on the calculated overlap of the clouds and treat two different aspects: the self-energy shift due to phononic coupling and the energy shift due to density modulation of the sodium BEC by the lattice. Both rely on the density calculation but in the δ over V_B/V_I plot they can be separated. At the crossing of the y-axis only the self-energy contribution is present. In Fig. 6.9 experimental data and theory for the scan of V_B/V_I and the dependence on the ^{6}Li atom number are depicted. For the left panel the median atom number of the plotted scans ranges from $4 \cdot 10^3$ to $11 \cdot 10^3$, the calculations are based on the mean number, 7400. The calculated values (stars) bend at high potential ratios. The reason are the large phase values that are calculated, which result in small net values due to the sinusoidal behavior. The cause of the large phase values is an overestimation of the lattice effect. It is based on the Thomas-Fermi approximation and can only be precise

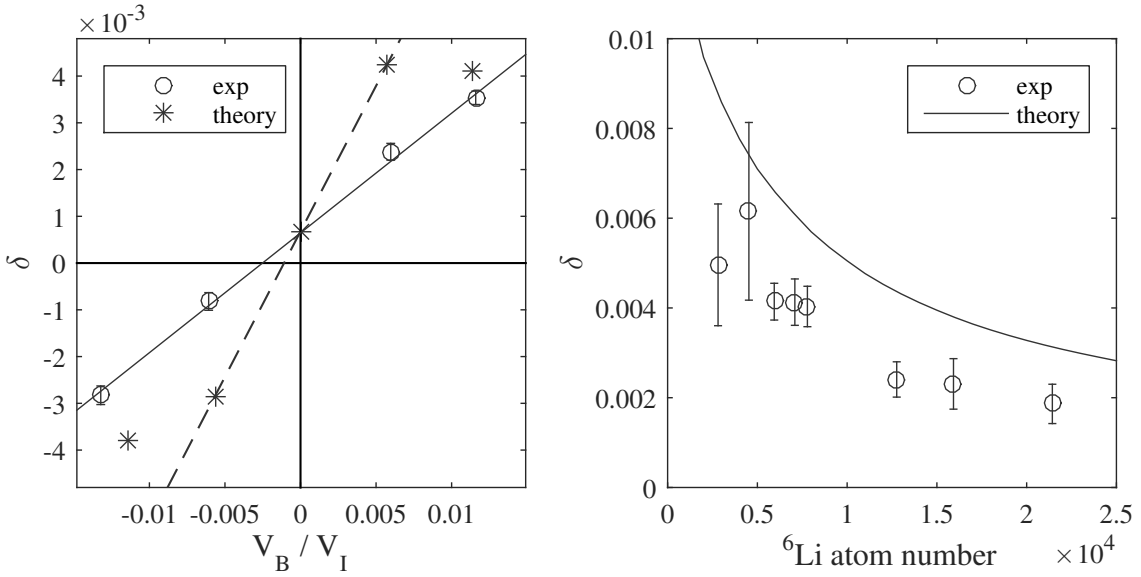

Figure 6.9: Comparison of experimental data to theory for ^{6}Li. In the left panel the lattice wavelength is scanned, plotted as the ratio of potentials. Measured data is plotted as circles, calculated values as stars. In the right panel the ^{6}Li atom number is scanned, strongly changing the overlap. Here theory is depicted by a line.

when $\xi < a$. As discussed thoroughly in Fig. 5.8 this is not everywhere the case in our system. The dashed line is a fit to the calculated points at $|V_\mathrm{B}/V_\mathrm{I}| = 0.005$. This fit nicely intersects at the calculated value for vanishing BEC potential. This gives the confirmation that for moderate phase values a deduction of the pure self-energy shift can be done from the values that are dominated by the lattice modulation. The slope of the dashed line surpasses the slope of the fit to experimental data by a factor of 2.4. The self-energy shift which is the intersection of the y-axis is met very well. It does not rely on the Thomas-Fermi approximation but takes the calculated ξ values into account. In summary, for fermions the overlap calculation seems reasonable and results in a good self-energy estimation, but the lattice effect is strongly overestimated.
This poses a challenge for further analyses. We want to see if the behavior in dependence of the impurity atom number is described well. But for fermionic impurities the lattice effect is dominant. In the right panel a calculated line and measured points are plotted. Here the potential ratio is $V_\mathrm{B}/V_\mathrm{I} = 0.011$, so it refers to the data point at the far right of the left panel. The evolution times for the two plots are slightly different, leading to a difference from the theoretical value on the left to the function value at 7400 atoms on the right. The lattice effect is proportional to η_im which is the geometrical overlap of the clouds. The trend of the data points is reproduced well, but one has to keep in mind that the small mismatch is due to the bending of the sine function for large phase values, see the left panel at $|V_\mathrm{B}/V_\mathrm{I}| = 0.012$. The increased uncertainty of the data points at small atom numbers might not just be due to detection issues, but have its root as well in the steep slope of δ at fluctuating lithium atom numbers. The criticality of the prediction clearly shows, why lithium atom numbers have to be postselected. The strong increase of δ in this graph gives an impression of the impurity-BEC interaction that can be reached in case of good geometrical matching of the clouds.

In case of ^{7}Li the self-energy becomes more important, at least for the condensed case. In Fig. 6.10 the corresponding comparison of calculated to measured data is shown. Again we study the values as a function of $V_\mathrm{B}/V_\mathrm{I}$ to differentiate between phononic effects and the density modulation of the sodium BEC by the far detuned lattice. For the bosonic impurity we distinguish two scenarios at different temperatures and call them condensed and thermal, whereby at high enough densities (atom numbers) condensation sets in even in the thermal case. On the left the assumed atom number for the condensed study is $34 \cdot 10^3$, for the thermal one it is $13 \cdot 10^3$. The condensed setting is plotted in blue and the calculated values (stars) are fitted like described for ^{6}Li (dashed line). Again the slope of the dashed line is twice as high as the slope of the fit to measurement data. But this time the self-energy shift is underestimated by a factor of three. This will become even more pronounced in the right panel.
The thermal scenario is well described by theory. For the self-energy (the y-axis intersection) this is clear, as we do not have BEC formation, leading to no substantial

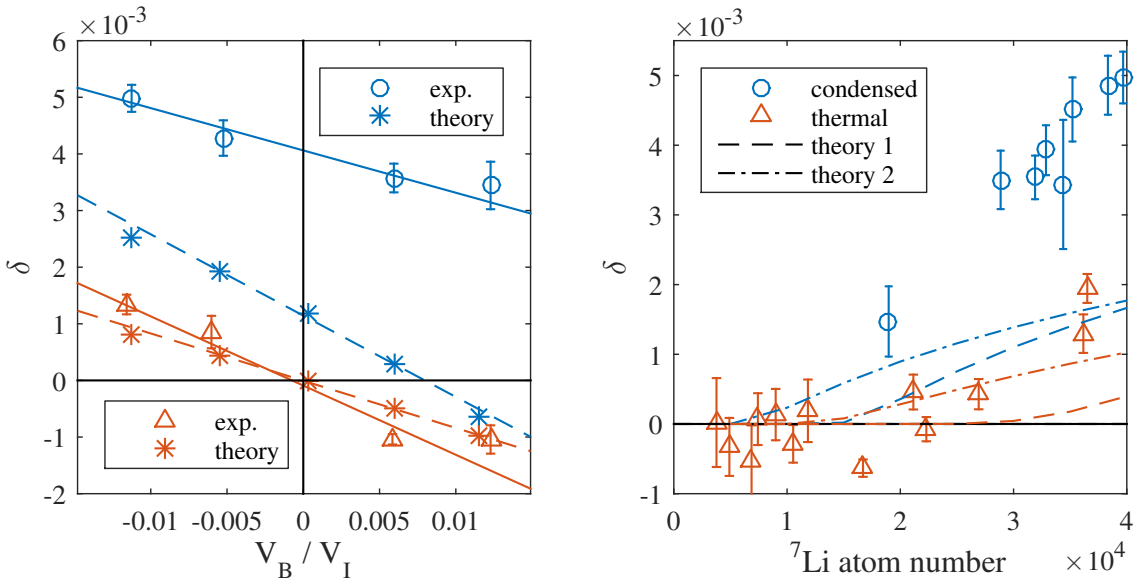

Figure 6.10: Comparison of experimental data to calculated values for ^{7}Li. Two scenarios at different temperatures are depicted (red and blue) and named condensed and thermal. On the left calculations are depicted as stars and fitted linearly (dashed line), on the right they are shown as dashed lines. Another calculation approach is plotted as dash dotted line.

shift. But the fit to the calculated data lies close to the fit to experimental values. As argued before, we expect the simple calculation to overestimate the lattice effect and therefore to exceed the experimental values. This indicates a mismatch. As $\delta_{\mathrm{latt}} \propto \eta_{\mathrm{im}}$ it is reasonable to assume that the geometrical matching of thermal cloud and sodium BEC η_{im} is underestimated by a factor of two, e. g. due to an incorrect temperature.

In the right panel the dependence on the atom number is studied. Here the lattice effect is subtracted, assuming it is similar for all impurity atom numbers. Calculated values are displayed as lines. The values represented by the dashed line are based on calculations that slice the lithium density in the optical dipole trap according to the lattice spacing and assigns the corresponding lithium atom numbers to the lattice sites, where the final density is calculated assuming a 2D situation. For the calculation of the dash-dotted line the lithium atoms are distributed over the trap assuming one overall chemical potential. Again the final density is calculated separately for each lattice site in 2D. See Fig. 3.7 for more information on the two techniques. The onset of condensation varies with the calculation approach, but the values at the atom numbers we are especially interested in are similar. There is

a large gap between theory and measurement showing that the self-energy shift is underestimated.
For the y-axis intersection in the left panel an error estimation can been performed. The most critical and unknown parameters are the atom numbers and the temperature. Increasing the sodium and lithium atom number by 20 % and reducing the temperature by 50 nK to 300 nK results in an absolute δ value of 61 Hz, roughly half of the measured 107 Hz. So in order to explain the mismatch for ^{7}Li a systematical error of the calculations or an incorrect parameter needs to be found. Further the backaction of lithium onto sodium has been neglected which in case of condensed ^{7}Li might be wrong as the lithium density gets very high. Still, in a naive picture taking the backaction into account reduces the overlap, as the interaction is repulsive. The mismatch of the theoretical description might be due to the failure of the Thomas-Fermi approximation. Furthermore it is an open question, if the relevant effects of two interacting BECs can be straightforward captured by the Fröhlich Hamiltonian.

7 Conclusion and Outlook

In this thesis some aspects of the Fröhlich Hamiltonian and its implementation in a mixture of ultracold atomic gases have been discussed. The observed increase of the energy level splitting is a clear signal of the Lamb shift, as it contradicts the expectation based on an increased effective mass.
The validity of a description of an impurity atom immersed into a BEC by the Fröhlich Hamiltonian relies on the description of the BEC via the Bogoliubov transformation. This transformation is based on a macroscopic occupation of the ground state. Strong interaction or high temperature reduce this number. In our experiment the sodium BEC is well suited for a description via the Bogoliubov theory. A further prerequisite for the mapping of the Fröhlich Hamiltonian onto the impurity-BEC scenario is a sufficiently small interspecies interaction strength [29]. The sodium-lithium interaction in our setup is sufficiently weak for both lithium isotopes. The impurity density should be low, as impurity-impurity interaction via the phonons is neglected in this description. The theory for ^{6}Li presented in section 5.2 takes the trap geometry and the Pauli blocking into account. For fermions the possibilities of scattering is reduced by occupied states. We discuss a single atom effect influenced by quantum statistics of the system. Still it is no polaron-polaron interaction, as the fermions do not interact via phonons. The low ^{6}Li density and the quantitative agreement between theory and measurements indicate that polaron-polaron interaction is not vital for the description in our experiment. Furthermore it is a process of higher order, having a marginal effect on the absolute value. In the case of condensed ^{7}Li, the atomic density is high. As these atoms are described by a single wave function, they can only interact with the ^{7}Li BEC at the next lattice site, which is relatively far away. In summary all constraints for the description of our experiments by the Fröhlich Hamiltonian are fulfilled.
In case of high impurity densities (condensed ^{7}Li), the Gross–Pitaevskii equation is a trustable theory as well and delivers analogous results. Still it is less controlled from a theoretical point of view. The Feynman diagrams attributed to the Fröhlich Hamiltonian are well understood, whereas they are unidentified for the Gross-Pitaevskii approach. For ^{6}Li the significance of the Gross–Pitaevskii result has to be questioned due to the low atomic density.// In contrast to the good agreement between experiment and theory for fermionic impurities, bosonic impurities show a much larger energy shift due to phononic coupling (≈ 3 times) than predicted. Several causes

for this mismatch are possible. The density calculation is difficult due to the strong variations resulting from the ^{7}Li condensation. Further, the impact of the lithium density onto the sodium cloud is neglected, which might affect the results due to the much higher densities for the bosonic species. Moreover, the potential of the optical dipole trap can deviate from the assumption of a three dimensional harmonic oscillator. In addition the partial immersion of the ^{7}Li BEC into the sodium BEC weakens the application of a homogeneous theory. A derivation of the corresponding results from the Fröhlich Hamiltonian for an inhomogeneous and finite BEC could clarify this question.
The second background-induced effect arises from the modulation of the sodium BEC by the lattice, which is captured within a Thomas-Fermi approximation in our description, overestimating the result. Better agreement of this trivial effect can be achieved by a numerical solution of the Gross-Pitaevskii equation for the whole system.
The measurements of the energy level spacing via Ramsey sequences are based on superpositions of the corresponding states. These are subject to decoherence, which causes a quickly decreasing contrast of the signal. An increase in interspecies interaction increases decoherence as well. The energy shift amplification by a condensed impurity is a fine workaround. Nevertheless, the strong coupling limit is in principle experimentally accessible and provoking as theory still does not deliver unique predictions. In our setup tuning of scattering lengths via Feshbach resonances has proven to cause strong losses, but some atomic mixtures exhibit less losses and have higher background scattering lengths. Another line of interest might be the possibility of observing a signature of polaron-polaron interaction [94, 95].
For the future a change of the geometry of the setup is promising. Experiments with homogeneous BECs have been reported [96, 97]. Such a realization obviates the need for complex density calculations and allows for direct comparison of experiments to theory. In the context of a finite but homogeneous BEC the controlled motion of an impurity atom is intriguing and can reveal dynamical effects [98], but experiments with a lattice of the type we already use have been proposed as well [31]. In both cases a good imaging resolution is necessary, as minute effects are expected in our atomic mixture.
In addition a reduction of the background dimension increases the probability of reabsorption of an emitted phonon. Thereby superradiance can be caused in a chain of impurity atoms in the excited state of the lattice. The resonance condition that has to be fulfilled is the matching of the phonon wavelength that is emitted when an impurity decays into the ground state to the distance of the lattice sites. In a next step the complexity of the system can be enhanced by a chiral bath [99].
An inspirational aim is the observation of the famous Casimir effect [100]. In its original version it describes a force attracting two parallel electrically conducting plates due to vacuum fluctuations. Its translation into ultracold atomic systems has been proposed for one-dimensional systems [101].

List of Figures

Bibliography

[1] P. A. M. Dirac. *The Quantum Theory of the Emission and Absorption of Radiation.* Proc. R. Soc. A Math. Phys. Eng. Sci. **114**, 243–265 (1927).

[2] J. Orear and E. Fermi. *Nuclear Physics: A Course Given by Enrico Fermi at the University of Chicago*. Midway Reprints (University of Chicago Press, 1950).

[3] E. Schrödinger. *Quantisierung als Eigenwertproblem.* Ann. Phys. **384**, 361–376 (1926).

[4] P. A. M. Dirac. *The Quantum Theory of the Electron.* Proc. R. Soc. A Math. Phys. Eng. Sci. **117**, 610–624 (1928).

[5] W. E. Lamb and R. C. Retherford. *Fine Structure of the Hydrogen Atom by a Microwave Method.* Phys. Rev. **72**, 241–243 (1947).

[6] D. J. Berkeland, E. A. Hinds, and M. G. Boshier. *Precise Optical Measurement of Lamb Shifts in Atomic Hydrogen.* Phys. Rev. Lett. **75**, 2470–2473 (1995).

[7] S. Bourzeix, B. de Beauvoir, F. Nez, M. D. Plimmer, F. de Tomasi, L. Julien, F. Biraben, and D. N. Stacey. *High Resolution Spectroscopy of the Hydrogen Atom: Determination of the 1S Lamb Shift.* Phys. Rev. Lett. **76**, 384–387 (1996).

[8] H. A. Bethe. *The Electromagnetic Shift of Energy Levels.* Phys. Rev. **72**, 339–341 (1947).

[9] P. W. Milonni. *The Quantum Vacuum: An Introduction to Quantum Electrodynamics* (Academic Press, 1994).

[10] T. Aoyama, M. Hayakawa, T. Kinoshita, and M. Nio. *Tenth-Order Lepton Anomalous Magnetic Moment—Sixth-Order Vertices Containing Vacuum-Polarization Subdiagrams.* Phys. Rev. D **84**, 053003 (2011).

[11] L. D. Landau. *Über die Bewegung der Elektronen im Kristallgitter.* Phys. Z. Sowjetunion **3**, 644–645 (1933).

[12] L. D. Landau and S. I. Pekar. *EFFECTIVE MASS OF A POLARON.* Zh. Eksp. Teor. Fiz. **18**, 419–423 (1948).

[13] H. Fröhlich. *Electrons in lattice fields.* Adv. Phys. **3**, 325–361 (1954).

[14] R. P. Feynman. *Slow Electrons in a Polar Crystal.* Phys. Rev. **97**, 660–665 (1955).

[15] J. Hodby, G. Jenkin, K. Kobayashi, and H. Tamura. *Cyclotron resonance of electrons and of holes in thallium chloride and in thallium bromide.* Solid State Commun. **10**, 1017–1020 (1972).

[16] J. W. Hodby, T. E. Jenkins, C. Schwab, H. Tamura, and D. Trivich. *Cyclotron resonance of electrons and of holes in cuprous oxide, Cu 2 O.* J. Phys. C Solid State Phys. **9**, 1429–1439 (1976).

[17] G. D. Mahan. *Many-Particle Physics*. 3rd ed. (Springer US, Boston, MA, 2000) pp. XII, 785.

[18] J. Devreese and S. Alexandrov. *Froehlich Polaron and Bipolaron: Recent Developments.* Rep. Prog. Phys. **72**, 131 (2009).

[19] A. S. Mishchenko, N. Nagaosa, K. M. Shen, Z.-X. Shen, X. J. Zhou, and T. P. Devereaux. *Polaronic metal in lightly doped high-T c cuprates.* EPL (Europhysics Lett. **95**, 57007 (2011).

[20] M. E. Gershenson, V. Podzorov, and A. F. Morpurgo. *Colloquium : Electronic transport in single-crystal organic transistors.* Rev. Mod. Phys. **78**, 973–989 (2006).

[21] I. N. Hulea, S. Fratini, H. Xie, C. L. Mulder, N. N. Iossad, G. Rastelli, S. Ciuchi, and A. F. Morpurgo. *Tunable Fröhlich polarons in organic single-crystal transistors.* Nat. Mater. **5**, 982–986 (2006).

[22] P. M. Platzman. *Ground-State Energy of Bound Polarons.* Phys. Rev. **125**, 1961–1965 (1962).

[23] B. A. Mason and S. Das Sarma. *Phonon-induced shift in shallow donor levels of semiconductor quantum structures.* Phys. Rev. B **33**, 8379–8384 (1986).

[24] T. Mitra, A. Chatterjee, and S. Mukhopadhyay. *Polarons.* Phys. Rep. **153**, 91–207 (1987).

[25] R. C. Brandt and F. C. Brown. *Induced Infrared Absorption due to Bound Charge in the Silver Halides.* Phys. Rev. **181**, 1241–1250 (1969).

[26] P. E. Simmonds, J. M. Chamberlain, R. A. Hoult, R. A. Stradling, and C. C. Bradley. *Far-infrared spectroscopy of bound and free electrons in III-V and II-VI semiconductors. I. Transitions between excited states observed in Zeeman spectroscopy of the shallow donor impurities.* J. Phys. C Solid State Phys. **7**, 4164–4184 (1974).

[27] J. Tempere, W. Casteels, M. K. Oberthaler, S. Knoop, E. Timmermans, and J. T. Devreese. *Feynman path-integral treatment of the BEC-impurity polaron.* Phys. Rev. B **80**, 184504 (2009).

[28] F. M. Cucchietti and E. Timmermans. *Strong-Coupling Polarons in Dilute Gas Bose-Einstein Condensates.* Phys. Rev. Lett. **96**, 210401 (2006).

[29] M. Bruderer, A. Klein, S. R. Clark, and D. Jaksch. *Polaron physics in optical lattices.* Phys. Rev. A **76**, 011605 (2007).

[30] I. Bloch, J. Dalibard, and W. Zwerger. *Many-body physics with ultracold gases.* Rev. Mod. Phys. **80**, 885–964 (2008).

[31] F. Grusdt, A. Shashi, D. Abanin, and E. Demler. *Bloch oscillations of bosonic lattice polarons.* Phys. Rev. A **90**, 063610 (2014).

[32] F. Grusdt, Y. E. Shchadilova, a. N. Rubtsov, and E. Demler. *Renormalization group approach to the Fröhlich polaron model: application to impurity-BEC problem.* Sci. Rep. **5**, 12124 (2015).

[33] T. Yin, D. Cocks, and W. Hofstetter. *Polaronic effects in one- and two-band quantum systems.* Phys. Rev. A **92**, 063635 (2015).

[34] A. Schirotzek, C.-H. Wu, A. Sommer, and M. W. Zwierlein. *Observation of Fermi Polarons in a Tunable Fermi Liquid of Ultracold Atoms.* Phys. Rev. Lett. **102**, 230402 (2009).

[35] M. Koschorreck, D. Pertot, E. Vogt, B. Frohlich, M. Feld, and M. Kohl. *Attractive and repulsive Fermi polarons in two dimensions.* Nature **485**, 619–622 (2012).

[36] C. Kohstall, M. Zaccanti, M. Jag, A. Trenkwalder, P. Massignan, G. M. Bruun, F. Schreck, and R. Grimm. *Metastability and coherence of repulsive polarons in a strongly interacting Fermi mixture.* Nature **485**, 615–618 (2012).

[37] Y. Zhang, W. Ong, I. Arakelyan, and J. E. Thomas. *Polaron-to-Polaron Transitions in the Radio-Frequency Spectrum of a Quasi-Two-Dimensional Fermi Gas.* Phys. Rev. Lett. **108**, 235302 (2012).

[38] S. Nascimbène, N. Navon, K. J. Jiang, L. Tarruell, M. Teichmann, J. McKeever, F. Chevy, and C. Salomon. *Collective Oscillations of an Imbalanced Fermi Gas: Axial Compression Modes and Polaron Effective Mass.* Phys. Rev. Lett. **103**, 170402 (2009).

[39] P. Massignan, M. Zaccanti, and G. M. Bruun. *Polarons, dressed molecules and itinerant ferromagnetism in ultracold Fermi gases.* Reports Prog. Phys. **77**, 034401 (2014).

[40] J. Catani, G. Lamporesi, D. Naik, M. Gring, M. Inguscio, F. Minardi, A. Kantian, and T. Giamarchi. *Quantum dynamics of impurities in a one-dimensional Bose gas.* Phys. Rev. A **85**, 023623 (2012).

[41] T. Fukuhara, A. Kantian, M. Endres, M. Cheneau, P. Schauß, S. Hild, D. Bellem, U. Schollwöck, T. Giamarchi, C. Gross, I. Bloch, and S. Kuhr. *Quantum dynamics of a mobile spin impurity.* Nat. Phys. **9**, 235–241 (2013).

[42] D.-S. Lühmann, K. Bongs, K. Sengstock, and D. Pfannkuche. *Self-Trapping of Bosons and Fermions in Optical Lattices.* Phys. Rev. Lett. **101**, 050402 (2008).

[43] S. Will, T. Best, S. Braun, U. Schneider, and I. Bloch. *Coherent Interaction of a Single Fermion with a Small Bosonic Field.* Phys. Rev. Lett. **106**, 115305 (2011).

[44] J. Heinze, S. Götze, J. S. Krauser, B. Hundt, N. Fläschner, D.-S. Lühmann, C. Becker, and K. Sengstock. *Multiband Spectroscopy of Ultracold Fermions: Observation of Reduced Tunneling in Attractive Bose-Fermi Mixtures.* Phys. Rev. Lett. **107**, 135303 (2011).

[45] D. J. Heinzen and M. S. Feld. *Vacuum Radiative Level Shift and Spontaneous-Emission Linewidth of an Atom in an Optical Resonator.* Phys. Rev. Lett. **59**, 2623–2626 (1987).

[46] M. Brune, P. Nussenzveig, F. Schmidt-Kaler, F. Bernardot, A. Maali, J. M. Raimond, and S. Haroche. *From Lamb shift to light shifts: Vacuum and subphoton cavity fields measured by atomic phase sensitive detection.* Phys. Rev. Lett. **72**, 3339–3342 (1994).

[47] A. Fragner, M. Goppl, J. M. Fink, M. Baur, R. Bianchetti, P. J. Leek, A. Blais, and A. Wallraff. *Resolving Vacuum Fluctuations in an Electrical Circuit by Measuring the Lamb Shift.* Science (80-.). **322**, 1357–1360 (2008).

[48] R. Scelle, T. Rentrop, A. Trautmann, T. Schuster, and M. K. Oberthaler. *Motional Coherence of Fermions Immersed in a Bose Gas.* Phys. Rev. Lett. **111**, 070401 (2013).

[49] N. F. Ramsey. *A Molecular Beam Resonance Method with Separated Oscillating Fields.* Phys. Rev. **78**, 695–699 (1950).

[50] J. Appmeier. *Immersed Quantum Systems: A Sodium Bose-Einstein Condensate for Polaron Studies*. Dissertation. Universität Heidelberg (2010).

[51] T. Schuster. *Feshbach Resonances and Periodic Potentials in Ultracold Bose-Fermi Mixtures*. Dissertation. Universität Heidelberg (2012).

[52] R. Scelle. *Dynamics and Motional Coherence of Fermions Immersed in a Bose Gas*. Dissertation. Universität Heidelberg (2013).

[53] C. A. Stan and W. Ketterle. *Multiple species atom source for laser-cooling experiments.* Rev. Sci. Instrum. **76**, 063113 (2005).

[54] R. Meppelink. *Hydrodynamic excitations in a Bose-Einstein condensate*. Dissertation. Universiteit Utrecht (2009).

[55] R. Scelle. *Cooling, Plugging, Trapping: Exploiting Optical Dipole Potentials For Polaron Experiments*. Diplomarbeit. Universität Heidelberg (2009).

[56] G. Breit and I. I. Rabi. *Measurement of Nuclear Spin.* Phys. Rev. **38**, 2082–2083 (1931).

[57] Z. Hadzibabic, S. Gupta, C. A. Stan, C. H. Schunck, M. W. Zwierlein, K. Dieckmann, and W. Ketterle. *Fiftyfold Improvement in the Number of Quantum Degenerate Fermionic Atoms.* Phys. Rev. Lett. **91**, 160401 (2003).

[58] W. Ketterle, K. B. Davis, M. A. Joffe, A. Martin, and D. E. Pritchard. *High densities of cold atoms in a dark spontaneous-force optical trap.* Phys. Rev. Lett. **70**, 2253–2256 (1993).

[59] K. M. R. van der Stam, A. Kuijk, R. Meppelink, J. M. Vogels, and P. van der Straten. *Spin-polarizing cold sodium atoms in a strong magnetic field.* Phys. Rev. A **73**, 063412 (2006).

[60] M.-O. Mewes, M. R. Andrews, N. J. van Druten, D. M. Kurn, D. S. Durfee, and W. Ketterle. *Bose-Einstein Condensation in a Tightly Confining dc Magnetic Trap.* Phys. Rev. Lett. **77**, 416–419 (1996).

[61] A. Görlitz, T. L. Gustavson, A. E. Leanhardt, R. Löw, A. P. Chikkatur, S. Gupta, S. Inouye, D. E. Pritchard, and W. Ketterle. *Sodium Bose-Einstein Condensates in the F=2 State in a Large-Volume Optical Trap.* Phys. Rev. Lett. **90**, 090401 (2003).

[62] F. Schreck. *Mixtures of ultracold gases: Fermi sea and Bose-Einstein condensate of lithium isotopes.* Dissertation. Université Pierre et Marie Curie - Paris VI (2002).

[63] S. Inouye, M. R. Andrews, J. Stenger, H.-J. Miesner, D. M. Stamper-Kurn, and W. Ketterle. *Observation of Feshbach resonances in a Bose–Einstein condensate.* Nature **392**, 151–154 (1998).

[64] R. Grimm, M. Weidemüller, and Y. B. Ovchinnikov. *Optical Dipole Traps for Neutral Atoms.* (Academic Press, 2000) pp. 95–170.

[65] C. Pethick and H. Smith. *Bose-Einstein Condensation in Dilute Gases* (Cambridge University Press, 2002).

[66] L. P. Pitaevskii and S. Stringari. *Bose-Einstein Condensation*. International Series of Monographs on Physics (Clarendon Press, 2003).

[67] W. Ketterle and M. W. Zwierlein. *Making, probing and understanding ultracold Fermi gases.* Riv. del Nuovo Cim. **31**, 247–422 (2008).

[68] N. Tammuz, R. P. Smith, R. L. D. Campbell, S. Beattie, S. Moulder, J. Dalibard, and Z. Hadzibabic. *Can a Bose Gas Be Saturated?* Phys. Rev. Lett. **106**, 230401 (2011).

[69] L. Khaykovich. *Formation of a Matter-Wave Bright Soliton.* Science (80-.). **296**, 1290–1293 (2002).

[70] D. A. Butts and D. S. Rokhsar. *Trapped Fermi gases.* Phys. Rev. A **55**, 4346–4350 (1997).

[71] Z. Hadzibabic and J. Dalibard. *Two-dimensional Bose fluids: An atomic physics perspective.* Riv. del Nuovo Cim. **34**, 389–434 (2011).

[72] E. P. Gross. *Structure of a quantized vortex in boson systems.* Nuovo Cim. **20**, 454–477 (1961).

[73] L. P. Pitaevskii. *Vortex Lines in an imperfect Bose gas.* Sov. Phys. JETP **13**, 451–454 (1961).

[74] F. Dalfovo, S. Giorgini, L. P. Pitaevskii, and S. Stringari. *Theory of Bose-Einstein condensation in trapped gases.* Rev. Mod. Phys. **71**, 463–512 (1999).

[75] D. A. Steck. *Sodium D Line Data.* (2010).

[76] M. E. Gehm. *Properties of 6Li.* (2003).

[77] W. Scherf, O. Khait, H. Jäger, and L. Windholz. *Re-measurement of the transition frequencies, fine structure splitting and isotope shift of the resonance lines of lithium, sodium and potassium.* Zeitschrift für Phys. D Atoms, Mol. Clust. **36**, 31–33 (1996).

[78] S. Knoop, T. Schuster, R. Scelle, A. Trautmann, J. Appmeier, M. K. Oberthaler, E. Tiesinga, and E. Tiemann. *Feshbach spectroscopy and analysis of the interaction potentials of ultracold sodium.* Phys. Rev. A **83**, 042704 (2011).

[79] T. Schuster, R. Scelle, A. Trautmann, S. Knoop, M. K. Oberthaler, M. M. Haverhals, M. R. Goosen, S. J. J. M. F. Kokkelmans, and E. Tiemann. *Feshbach spectroscopy and scattering properties of ultracold Li + Na mixtures.* Phys. Rev. A **85**, 042721 (2012).

[80] L. J. LeBlanc and J. H. Thywissen. *Species-specific optical lattices.* Phys. Rev. A **75**, 053612 (2007).

[81] F. Bloch. *Über die Quantenmechanik der Elektronen in Kristallgittern.* Zeitschrift für Phys. **52**, 555–600 (1929).

[82] A. Kastberg, W. D. Phillips, S. L. Rolston, R. J. C. Spreeuw, and P. S. Jessen. *Adiabatic Cooling of Cesium to 700 nK in an Optical Lattice.* Phys. Rev. Lett. **74**, 1542–1545 (1995).

[83] M. Greiner, I. Bloch, O. Mandel, T. W. Hänsch, and T. Esslinger. *Exploring Phase Coherence in a 2D Lattice of Bose-Einstein Condensates.* Phys. Rev. Lett. **87**, 160405 (2001).

[84] E. L. Hahn. *Spin Echoes.* Phys. Rev. **80**, 580–594 (1950).

[85] D. Chen, C. Meldgin, and B. DeMarco. *Bath-induced band decay of a Hubbard lattice gas.* Phys. Rev. A **90**, 013602 (2014).

[86] E. Nicklas. *A new tool for miscibility control: Linear coupling.* Dissertation. Universität Heidelberg (2013).

[87] A. Görlitz, J. M. Vogels, A. E. Leanhardt, C. Raman, T. L. Gustavson, J. R. Abo-Shaeer, A. P. Chikkatur, S. Gupta, S. Inouye, T. Rosenband, and W. Ketterle. *Realization of Bose-Einstein Condensates in Lower Dimensions.* Phys. Rev. Lett. **87**, 130402 (2001).

[88] A. Shashi, F. Grusdt, D. a. Abanin, and E. Demler. *Radio-frequency spectroscopy of polarons in ultracold Bose gases.* Phys. Rev. A **89**, 053617 (2014).

[89] F. Grusdt. *Topological phases and polaron physics in ultra cold quantum gases.* Dissertation. Universität Kaiserslautern (2015).

[90] R. P. Feynman. *Mathematical Formulation of the Quantum Theory of Electromagnetic Interaction.* Phys. Rev. **80**, 440–457 (1950).

[91] A. O. Barut and J. F. Van Huele. *Quantum electrodynamics based on self-energy: Lamb shift and spontaneous emission without field quantization.* Phys. Rev. A **32**, 3187–3195 (1985).

[92] A. O. Barut. *Quantum electrodynamics based on self-energy versus quantization of fields: Illustration by a simple model.* Phys. Rev. A **34**, 3502–3503 (1986).

[93] I. Bialynicki-Birula. *Comment on "Quantum electrodynamics based on self-energy: Lamb shift and spontaneous emission without field quantization".* Phys. Rev. A **34**, 3500–3501 (1986).

[94] W. Casteels, J. Tempere, and J. T. Devreese. *Many-polaron description of impurities in a Bose-Einstein condensate in the weak-coupling regime.* Phys. Rev. A **84**, 063612 (2011).

[95] A. Klein and M. Fleischhauer. *Interaction of impurity atoms in Bose-Einstein condensates.* Phys. Rev. A **71**, 033605 (2005).

[96] A. L. Gaunt, T. F. Schmidutz, I. Gotlibovych, R. P. Smith, and Z. Hadzibabic. *Bose-Einstein Condensation of Atoms in a Uniform Potential.* Phys. Rev. Lett. **110**, 200406 (2013).

[97] L. Chomaz, L. Corman, T. Bienaimé, R. Desbuquois, C. Weitenberg, S. Nascimbène, J. Beugnon, and J. Dalibard. *Emergence of coherence via transverse condensation in a uniform quasi-two-dimensional Bose gas.* Nat. Commun. **6**, 6162 (2015).

[98] D. Dasenbrook and A. Komnik. *Semiclassical polaron dynamics of impurities in ultracold gases.* Phys. Rev. B **87**, 094301 (2013).

[99] T. Ramos, H. Pichler, A. J. Daley, and P. Zoller. *Quantum Spin Dimers from Chiral Dissipation in Cold-Atom Chains.* Phys. Rev. Lett. **113**, 237203 (2014).

[100] H. B. G. Casimir. *On the attraction between two perfectly conducting plates.* in *Proc. KNAW*. Vol. 51 (1948) pp. 793–795.

[101] M. Schecter and A. Kamenev. *Phonon-Mediated Casimir Interaction between Mobile Impurities in One-Dimensional Quantum Liquids.* Phys. Rev. Lett. **112**, 155301 (2014).

Danksagung

Während der Promotion habe ich vielseitige Unterstützung erfahren, für die ich mich bedanken möchte.
Zunächst möchte ich Markus Oberthaler danken für die Aufnahme in seine Gruppe, die vielen interessanten, intensiven und lehrreichen Diskussionen und seine Begeisterung, die immer wieder Schwung in das Projekt gebracht hat.
Selim Jochim danke ich für die Übernahme der Zweitkorrektur und ihm und seinem Team dafür, dass sie uns immer mit Rat und Ausrüstung unterstützt haben.
Am NaLi möchte ich Tobi und Raphi für den Aufbau des Experiments und meine gute Einarbeitung danken. Glücklicherweise haben sie noch ausreichend Betätigung für nachfolgende Generationen gelassen. Diese Aufgaben bin ich über die Dauer der Promotion zusammen mit Arno angegangen, der technische, physikalische und moralische Unterstützung geboten hat. Auch den Diplom-, Bachelor- und Masterstudenten, die am Experiment mitgearbeitet haben, möchte ich danken. Unserem Nachfolger, der Frohnatur Fabián, danke ich für seine aufopferungsvolle und humorvolle Art, die das Laborleben bereichert.
Andreas Komnik danke ich für seine ausdauernde Unterstützung des Projekts von theoretischer Seite, die sich auch in über 160 E-Mails im Laufe des letzten Jahres widerspiegelt. Es ist immer spannend, seine abstrakte Beschreibungsweise des Experiments nachzuvollziehen.
Fred danke ich für die Hilfe, das Thema in den größeren Kontext einzuordnen, was sich als erstaunlich vielschichtig erwiesen hat. Für die Zukunft wünsche ich ihm viel Erfolg und ein gutes Händchen für das NaLi.
Den Mikado-Spezialisten Daniel, Helmut und Wolfgang danke ich für theoretische und experimentelle Unterstützung, die sich bis zum Korrektur Lesen dieser Arbeit erstreckt.
Allen Matterwavern danke ich für eine positive und konstruktive Atmosphäre, die sich auch tief in den privaten Bereich erstreckt.
Sehr gut gefallen haben mir natürlich die Mountainbike Touren, bei denen sich Matterwaver und Gäste von ihrer sportlichen Seite gezeigt haben, einige auch ihre Grenzen kennen gelernt haben. Ich hoffe, dass es Zhongyi gelingt, diese Bewegung fortzuführen.
Allen Mitarbeitern des KIP danke ich für ihr Dazutun. Das reicht von der EDV, der Verwaltung, über die Elektronik bis zur feinmechanischen Werkstatt. Insbesondere

Christiane und Dagmar waren immer sehr hilfsbereit.
Fabian Grusdt, Pietro Massignan und Tao Yin danke ich für die Diskussion der mit unserem Experiment verbundenen Physik.